Electronic Theses and Dissertations

Theses, Dissertations, and Major Papers

1991

Damage accumulation below the worn surfaces during the sliding wear of copper.

Hongfa. Hu
University of Windsor

Follow this and additional works at: https://scholar.uwindsor.ca/etd

Recommended Citation

NOTICE

AVIS

The quality of this microform is heavily dependent upon the quality of the original thesis submitted for microfilming. Every effort has been made to ensure the highest quality of reproduction possible.

If pages are missing, contact the university which granted the degree.

Some pages may have indistinct print especially if the original pages were typed with a poor typewriter ribbon or if the university sent us an inferior photocopy.

Reproduction in full or in part of this microform is governed by the Canadian Copyright Act, R.S.C. 1970, c. C-30, and subsequent amendments.

La qualité de cette microforme dépend grandement de la qualité de la thèse soumise au microfilmage. Nous avons tout fait pour assurer une qualité supérieure de reproduction.

S'il manque des pages, veuillez communiquer avec l'université qui a conféré le grade.

La qualité d'impression de certaines pages peut laisser à désirer, surtout si les pages originales ont été dactylographiées à l'aide d'un ruban usé ou si l'université nous a fait parvenir une photocopie de qualité inférieure.

La reproduction, même partielle, de cette microforme est soumise à la Loi canadienne sur le droit d'auteur, SRC 1970, c. C-30, et ses amendements subséquents.

Canada

DAMAGE ACCUMULATION BELOW THE WORN SURFACES

DURING THE SLIDING WEAR OF COPPER

by

HONGFA HU

A Thesis
Submitted to the Faculty of Graduate Studies and Research
through the Engineering Materials Group
of the Department of Mechanical Engineering
in Partial Fulfillment of the Requirements
for the Degree of Master of Applied Science
in Engineering Materials
at the University of Windsor

Windsor, Ontario, Canada, 1991

© Hongfa Hu, 1991

ISBN 0-315-69893-4

Canada

ABSTRACT

Damage accumulation below the contact surfaces constitutes an important form of delamination wear in ductile materials. In this study, metallographic techniques were used to determine the extent of plastic deformation and strain localization events during the sliding wear of commercially pure copper samples. Tests were performed using a block-on-ring type wear machine on specimens in annealed condition and after 50% deformation by rolling. Strain and microhardness gradients were measured as a function of sliding distance and the strain hardening behavior of deformed subsurface layer was determined. It was observed that both the magnitude of strain gradients and the depths of plastically deformed layer increased with the sliding distance. Wear proceeded with the removal of flakelike debris formed as a result of subsurface fracture through a shear band decohesion mechanism. It was found that the location of maximum damage was not at the contact surface but at a certain distance below it. This critical depth was determined by the relative intensities of shear and hydrostatic stress gradients. A model based on Rice and Tracy analysis of void growth was proposed to account for the experimental observations. The stress and strain distributions adjacent to the wear surface were sensitive to the degree of prior cold working. In addition, the wear rate of the 50% rolled specimens was higher than that of annealed specimens when tested at loads higher than 1000 g. This was related to the different strain hardening behavior and the smaller thickness of plastically deformed layer for rolled Cu below the worn surface.

To My Parents

ACKNOWLEDGEMENTS

TABLE OF CONTENTS

viii

LIST OF TABLES

LIST OF FIGURES

Chapter 1. INTRODUCTION

In different sections of manufacturing processes, various forms of wear happen and in some cases this constitutes the cause of failure. In industrialized societies, a high proportion of the gross national product is used to replace the failures due to wear and to improve the life of machinery also have the economic advantages. Progress in wear control and prevention can be achieved when the mechanisms by which wear occurs are better understood.

Wear defined as progressive loss of substance from the operating surface of a body occurs as a result of relative motion at the surface. The different modes of wear exhibit different mechanisms which are dependent on material properties. These mechanisms have not been fully understood and the general practice for each sector in industry has been to devise its own approach and solution to the specific type of wear problem.

Sliding wear is due to a relative motion between two smooth solid surfaces in contact under load. Sliding wear is an important part in wear and comprises many mechanisms such as adhesion, surface fatigue, tribochemical reactions, abrasion. A plastic deformation accumulation process below the worn surfaces is usually involved in most of these mechanisms. Thus, sliding wear is a complicated problem due to the presence

1

of large strains and a complex stress state in the vicinity of the surface contact resulting in the subsurface crack growth and fracture.

The present project is focused on the plastic deformation and damage accumulation below the worn surfaces as well as the effect of prior deformation on sliding wear in a commercial purity copper. This material was selected for study because of the large amount of information in literature on its mechanical properties. The purpose of this study is as follows:

(1) to investigate stress and strain gradients generated during sliding wear, strain hardening behavior in highly deformed layers, and relate these to the wear rates,

(2) to characterize the microstructural changes that occur during sliding wear as a function of sliding distance,

(3) to study the effect of prior deformation before the wear test on sliding wear by comparison of results from annealed and rolled coppers.

Chapter 2. LITERATURE SURVEY

Tribology is the science and technology of interacting surfaces in relative motion [1]. Wear is one of the principal constituents of tribology and has been given special attention because wear of the machine elements is a critical issue for material and energy conservation[2].

A better understanding of the factors that influence wear resistance is of great importance for the prediction and selection of materials by designers and engineers. A large number of articles on wear have been presented in science and engineering journals, e.g., the journal Wear, Tribology International, Journal of Tribology, Proceedings of the International Conferences on Wear of Materials, etc. In the past decades, a number of comprehensive handbooks and texts have been published on the subject of wear[3-13].

The sliding wear behavior of materials is influenced greatly by the chemical, mechanical properties and microstructure. Microscopic examination of the highly deformed near-surface regions has shown that plastic deformation is mainly responsible for the occurrence of sliding wear processes such as void formation, crack nucleation and propagation[14-16]. These processes often lead to the detachment of subsurface layers and to the material removal by delamination[3,4,14,17].

The following literature survey on deformation and damage accumulation is organized into five sections:

(1) Elastic deformation beneath contact surfaces,

(2) Plastic deformation below the worn surfaces,

(3) Crack nucleation and propagation below the worn surfaces,

(4) Wear debris morphology and formation,

(5) Effect of prior deformation on wear.

2.1 Elastic Deformation Beneath Contact Surfaces

When two solid surfaces come into contact in sliding wear, there is some force applied to one of the surfaces pressing it against the other in contact. At first, the force applied to the contact surface produces elastic deformation, and if the applied load is sufficiently high, plastic deformation on and below the surface is formed.

Due to the roughness and waviness of the surfaces, contact between the solids takes place only at discrete points (Fig.2.1). Considering discontinuous points as individual contact spots, the elastic strains and stresses at and below contact spots can be approximately assessed from Hertz and Boussinesq solutions[18-21].

2.1.1. Hertzian Contact

When two elastic solids are brought into contact they touch initially at a single point or along a line. Under the action of the slightest load they deform in the vicinity of their point of first contact so that they touch over an area which is finite though small compared with the dimensions of the two bodies. Hertzian theory predicts the shape of this area of contact and how it grows in size with increasing load. The magnitude and distribution of stresses in the vicinity of the elastic contact region are also given[18].

Assumptions made in Hertzian theory are :

(i) the surfaces are continuous and non-conforming;

(ii) the strains are small; and

(iii) the surfaces are frictionless.

Consider the contact of a sphere and a plane under a normal load (P) with the radius (a) of contact area seen in Fig.2.2[19]. For simplicity, both a sphere and a plane in contact have the same Young's modulus E and Poisson's ratio v. The contact radius (a) and the maximum contact pressure P_{max} are given by

$$a = 1.11 (P \cdot R)^{1/3} \qquad\qquad (2.1)$$

and

$$P_{max} = -0.388 (P \cdot E^2 / R^2)^{1/3} \qquad (2.2)$$

where P is the normal load, R is the radius of the sphere, and E is the Young's modulus with $E_1 = E_2$ and $v_1 = v_2 = 0.3$.

The maximum shear stress τ_{max} at a certain depth Z_m beneath the worn surface can also be estimated by the expressions as below

$$\tau_{max} = 0.31 P_{max} \qquad (2.3)$$

$$Z_m = 0.47 a \qquad (2.4)$$

Because the theory assumes that only a normal load is applied without a tangential load what happens in sliding wear is far from that in Hertz theory.

2.1.2. Stress Distribution Under Normal Point Loading

Boussinesq (1885) and Cerruti (1882) presented their solution for stress field in an elastic half-space under normal point loading, that is, contact at a infinitely small area[20]. Simplifying the contact points as surface subjected to a normal point load, the Boussinesq and Cerruti solution can be improved and applied to the sophisticated problem

of the stress field on and below the contact surface in wear.

For an isotropic material under a normal point load, Boussinesq's and Cerruti's solution for stress components in a polar coordinate system (Fig.2.3) is summarized as below[21]:

$$\sigma_{rr} = \frac{P}{\pi R^2} \left[\left(\frac{1-2\nu}{4} \right) \sec^2 \frac{\phi}{2} - \frac{3}{2} \cos\phi \sin^2\phi \right] \qquad (2.5)$$

$$\sigma_{\theta\theta} = \frac{P}{\pi R^2} \left[\left(\frac{1-2\nu}{2} \right) \left(\cos\phi - \frac{1}{2} \sec^2 \frac{\phi}{2} \right) \right] \qquad (2.6)$$

$$\sigma_{zz} = \frac{P}{\pi R^2} \left[-\frac{3}{2} \cos^3\phi \right] \qquad (2.7)$$

$$\sigma_{rz} = \frac{P}{\pi R^2} \left[-\frac{3}{2} \cos^2\phi \sin\phi \right] \qquad (2.8)$$

$$\sigma_{r\theta} = \sigma_{\theta z} = 0 \qquad (2.9)$$

The principal normal stresses can also be obtained as follows :

7

$$\sigma_{11} = \sigma_{rr} \sin^2\alpha + \sigma_{zz} \cos^2\alpha - 2\sigma_{rz} \sin\alpha\cos\alpha \tag{2.10}$$

$$\sigma_{22} = \sigma_{\theta\theta} \tag{2.11}$$

$$\sigma_{33} = \sigma_{rr} \cos^2\alpha + \sigma_{zz} \sin^2\alpha + 2\sigma_{rz} \sin\alpha\cos\alpha \tag{2.12}$$

where

$$\alpha = \frac{1}{2} \arctan \frac{2\sigma_{rz}}{\sigma_{zz} - \sigma_{rr}} \tag{2.13}$$

The hydrostatic stress is given by

$$\sigma = \frac{1}{3} (\sigma_{11} + \sigma_{22} + \sigma_{33}) \tag{2.14}$$

In order to simplify the discussion, the emphasis is put on the area directly below the point load, i.e., along the Z-axis[21]. In this case, i.e., $\phi = 0$, $R = Z$, the stress components are

$$\sigma_{rr} = \sigma_{\theta\theta} = \frac{P}{\pi Z^2} \left[\frac{1-2\nu}{4} \right] \tag{2.15}$$

$$\sigma_{zz} = -\frac{3P}{2\pi Z^2} \qquad\qquad (2.16)$$

$$\sigma_{r\theta} = \sigma_{\theta z} = \sigma_{rz} = 0 \qquad\qquad (2.17)$$

Based on the analysis as above, the principal normal stresses should be

$$\sigma_{11} = -\frac{3P}{2\pi Z^2} \qquad\qquad (2.18)$$

$$\sigma_{22} = \sigma_{33} = \frac{1-2\nu}{4} \frac{P}{\pi Z^2} \qquad\qquad (2.19)$$

in which σ_{11} is in the z-direction and σ_{22}, σ_{33} on orthogonal plane normal to z-axis. The hydrostatic stress, σ_H, can be obtained by the above expression

$$\sigma_H = -(1+\nu)\frac{P}{3\pi Z^2} \qquad\qquad (2.20)$$

Thus, according to the above equation:

(i) There is a linear relationship between the hydrostatic stress and an normal load; the hydrostatic stress is compressive at all times;

(ii) Since the hydrostatic stress is a function of $1/Z^2$, a hydrostatic stress gradient occurs in the subsurface material with its maximum value at the surface.

In addition, the effective stress related to shear stress can be defined as[22]

$$\sigma_{eff}=\frac{\sqrt{2}}{2}[(\sigma_{11}-\sigma_{22})^2+(\sigma_{11}-\sigma_{33})^2+(\sigma_{33}-\sigma_{22})^2]^{1/2} \qquad (2.21)$$

For the same case, i.e., along the Z-axis, used to analyze the hydrostatic stress, the effective stress can be calculated as a function of Z and P

$$\sigma_{eff}=\frac{7-2v}{4}\frac{P}{\pi Z^2} \qquad (2.22)$$

Almost the same dependence of effective stress on depths can be summarized based on the above relationship between normal load P and depth Z as that of hydrostatic stress. The effective stress increases linearly with normal load and decreases quickly with $(1/Z^2)$.

Boussinesq's and Cerruti's solution provides a basic conclusion, that is, the steep gradients for both hydrostatic and effective stresses exist below the contact surface. However, because of the unrealistic assumptions :

(i) only normal loads applied, (ii) an infinitely small point contact,

the calculated values for both hydrostatic and effective stresses are too high. By assuming a circular contact region of diameter (2a) subject to a normal and a tangential force distributed hemispherically over the surface, Hamilton and Goodman[21] have carried out an elastic analysis for stress components. According to this analysis there is also a sharp compressive hydrostatic stress gradient with its maximum at the surface and its value

decreases rapidly with increase of depth. But, the effective stress increases with depth until it reaches a maximum at a certain depth which depends on the friction coefficient beneath the surface; after that depth, the value of effective stress falls monotonically with increasing depth. Comparing the isochromatic pattern of shear stress due to the normal load with that due to both normal and tangential loads, it is seen in Fig.2.4 that the location of the greatest value of the maximum shear stress, where the failure most likely takes place, is much nearer to the surface in the case where both normal and tangential loads are applied.

2.2. Plastic Deformation Below the Worn Surfaces

In sliding wear, large strains can occur at and near the worn surface of a ductile material. A deformation gradient can exist in a region of ductile material beneath the worn surfaces. Tangential forces introduce the shear stresses that tend to cause plastic deformation and void nucleation. The hydrostatic stresses developed delay microvoid coalescence and ductile fracture[3].

The microstructure of the deformed material can broadly be classified into a three layered structure as illustrated schematically in Fig.2.5.

(1) Transfer layer -- typically of a few micrometers thick[23,24,25].

This layer can be thought as a microcomposite consisting of an intimate mechanical mixture of crystallites derived from both sliding materials.

11

(2) The highly deformed layer -- In the most cases, the highly deformed layer may extend to tens or hundreds of micrometers. A plastic flow pattern is usually revealed by grain boundaries curved in the sliding direction (Fig.2.5).

(3) The undeformed bulk material.

In this section, the strain hardening and the structural properties of highly deformed layers generated during sliding contacts will be reviewed. However, first, it is worth while to review the stress-strain behavior of ductile materials subjected to large strains during more conventional mechanical deformation processes such as cold rolling and wire drawing.

2.2.1. Stress-Strain Behavior and Microstructure at Large Deformation

Since the primary aim of cold working is to change the shape of products, deformations applied in such processes tend to be large[26]. The total strain applied by most cold working processes is higher than $\varepsilon = 1$. Such deformations can be regarded to involve "large" strain compared with the maximum strain attainable in tensile test (0 - 0.5). However, the term "large" strains is used in a qualitative way and usually there is no clearly definable bound distinguishing small and large strains.

The typical stress-strain curve of FCC metals shows a gradually decreasing work-hardening rate at large strains. A saturation flow stress where is no more work hardening

is reached at certain large strains. For Al, Cu, Ag, the saturation stresses appear at equivalent strain $\varepsilon \approx 3$. The work hardening rate increases until the saturation stress. A flow curve for BCC metal (iron) shows an almost constant work-hardening rate of 153 MNm^{-2} from $\varepsilon \approx 1$ up to the largest total strain $\varepsilon \approx 7$[27]. This hardening behavior in large strains is also observed in other BCC metals, for instance, tungsten.

According to conventional engineering description, the flow curve for small strain can be given by the power expression of the form[28]:

$$\sigma = K_1 \varepsilon^n \qquad (2.23)$$

where σ is the flow stress, ε is the strain, K_1 is a material constant and n is the strain-hardening coefficient. However, the above equation is inadequate for large strains. Voce equation[29] gives one of the most commonly accepted descriptions of flow stress-strain curve at large strains:

$$\sigma = \sigma_s - (\sigma_s - \sigma_o) \, e^{-\varepsilon/\varepsilon_c} \qquad (2.24)$$

where σ is the flow stress at strain ε, σ_o is the yield stress, σ_s is a saturation stress where work hardening rate, $d\sigma/d\varepsilon =0$, ε_c is a constant.

The above equations are phenomenological, i.e., produced by curve fitting. There have been some attempts to relate the stress-strain behavior at large deformation to the

microstructural properties. In particular, Embury and Fisher[30] studied microstructural changes during wire drawing of pearlite and proposed the following expression:

$$\sigma = \sigma_i + \frac{k}{\sqrt{2}\sqrt{r_0}} \exp\left(\frac{\varepsilon}{4}\right) \qquad (2.25)$$

where σ is the flow stress after drawing to strain ε, σ_i is the friction stress, k is a material constant and r_0 is the mean spacing between barriers to dislocation motion, i.e., cell size before drawing.

The cold-worked substructure of polycrystals (e.g., copper) has been studied by many research workers using TEM[31-33]. The onset of plastic deformation is accompanied by profuse multiplication of dislocations. Dislocation density rapidly rises by several orders of magnitude. Tangles of dislocations become progressively interconnected, thus giving rise to a rough cellular structure at strain as low as 3%. Following the application of a strain of about 10% a cellular structure can be observed. The cellular structure consists of continuous walls of dense tridimensional tangles surrounding areas of smaller dislocation density. The density in the walls is estimated to be three to five times that inside the cells. The shape and size of the cells created by low strains change as deformation increases. The average shape of the cells follows the trend imposed by the external shape change; all become fibers when drawn, ribbons when

14

rolled and disks when compressed.

Another important feature of microstructure at high strains is the formation of shear bands. The bands are usually thin (mostly less than 1 μm) and many contain elongated subgrains[26]. In rolling, the shear bands develop at about $\pm35^\circ$ to the rolling plane and divide the specimen into prisms that have their long axes parallel to the transverse direction[30,34].

2.2.2. Plastic Deformation during Sliding Wear

2.2.2.1. Metallographic observations

Detailed information below the worn surfaces can be obtained by metallographic observations made on the longitudinal sections (on a plane normal to the wear surface and parallel to the sliding direction) and transverse sections (on a plane normal to both the sliding direction and the wear surface) shown in Fig.2.7.

A longitudinal cross section of worn copper specimen was analyzed by Heilman[35] with the help of TEM and STEM. At the low strains, (i.e., at the regions away from the worn surfaces), the substructure is composed of equiaxed cells bounded by dislocation walls. Closer to the worn surface, the substructure progressively transfers to smaller and more elongated subgrains with sharper walls. These substructural features

show similarities with those reported for large plastic strains produced by conventional deformation processes[26,31,34,36-39]. The investigations on the cross sections by Ohmae et al using TEM[40] also showed that the dislocation cell size became larger as the depth from the worn surface increased, but cells only slightly elongated in an orientation parallel to the surface and normal to the sliding direction. According to the TEM studies on the longitudinal sections, cell shape either resembles a slab or an ellipsoid with the large planar face parallel to the wear surface and elongated in the sliding direction[40,41].

The plastic deformation and the presence of strain gradients can also be observed on the transverse sections[42-44]. Alpas and Embury[42] indicated that orthogonal shear bands at 35° to the wear surface were found on this section in copper. With increasing strain, i.e., on approaching the surface, the number of shear band increases and spacing between them becomes smaller.

The influence of stacking fault energy (SFE) on the wear has been studied by Wert et al[43]. They found that the wear rate of a series of Cu-Al alloys increased with decreasing SFE. This was attributed to the fact that in low SFE metals, planar slip and twinning would be involved in the deformation process.

2.2.2.2. Hardness gradients

16

Microhardness has been used by many research workers to assess the extent and the characteristics of plastic deformation due to the wear process[45-51]. A common method involves cross-sectioning of the worn surfaces and measuring the microhardness as a function of depth below the worn surface. However, because the zone of the most severe deformation is usually shallow, the cross-sectioning shows poor spatial resolution of the microhardness. However, taper sectioning described in section 3.4.1. can be regarded as an effective method for improving the resolution of microhardness measurements near the worn surface.

Richardson[4] related the abrasive wear resistance to the hardness of the worn surface; the higher the hardness of the worn surface reached, the better the wear resistance of materials. Moore et al[45] argued that the surface hardness depended on the bulk hardness and the strain hardening properties of material.

2.2.2.3. Strain gradients

The accumulated strain below the contact surfaces can be estimated from the comparison of grain boundary shape before and after the sliding wear[51]. Usually the plastic shear strain decreases with increasing depth. Heilman and Rigney suggested that the plastic shear strain gradients below the worn surface may be approximated by the expression[52]:

$$\gamma = \gamma_{surface} \exp(-AZ) \qquad (2.26)$$

17

where Z is the depth from the worn surface and A is a constant.

Studies of strains around the wear track in iron and copper were carried out by Ruff[53] using the selected area electron channeling pattern technique. Although strains only up to 20% can be measured by this technique, their conclusions showed that the strains associated with the wear track, have their maxima at the surface of the track center and decrease with depth.

2.3. Crack Nucleation and Propagation below the Worn Surfaces

In sliding wear, the surface and subsurface shear deformation can occur as a result of repeated normal and tangential loading. As the subsurface deformation continues, cracks may nucleate at a certain depth below the contact surface because a hydrostatic stress state with a maximum value at the contact surfaces exists beneath the contact region.

The crack nucleation in sliding wear was observed to be favored by inclusion particles, grain boundaries and twin boundaries[19]. Goods and Brown[54] proposed that dislocation cell boundaries would act as crack nucleation sites. It was argued that localized slip in the form of shear band formation could lead to crack nucleation and propagation below the worn surfaces[40].

18

For materials containing hard particles, cracks may form when these particles fracture. Crack nucleation sites may also be produced during plastic deformation by the decohesion of the matrix-particle interface[55-57]. Suh et.al.[58] have referred to Hertz stress calculations to rationalize cracks nucleating at the particle/matrix interfaces at some distance from the surface.

One important mechanistic concept that arises from the crack nucleation and propagation is the delamination theory of wear developed by Suh and co-workers[15]. According to this model shown in Fig.2.8, the stresses applied at the surface produce subsurface dislocations which are organized into cellular structure, ultimately leading to the formation of cracks in the highly strained portions of the lattice. The spread of the cracks along cell boundaries, both parallel and perpendicular to the surface, leads to the removal of flake-shape wear debris. This mechanism has been the subject of much discussion, and has not found uniform acceptance since certain aspects of the crack nucleation and propagation processes remain unclear.

The role played by particles in void formation and crack nucleation has been studied extensively in simple stress states[59-63]. A necessary condition for the nucleation of void, by decohesion of the particle/matrix interface, is that the elastic strain released by the particle is at least equal to the newly created surface energy[59-61]. However, an additional condition for void nucleation by decohesion is the attainment of a critical normal stress σ_c at the particle/matrix interface[60,61]. For the case of small particles

(radius r<1 μm), dislocation models[59,60] are required to estimate the local flow stress σ_l. Brown and Stobbs[63] showed that the dislocation density ρ_l around a particle is given approximately by $\rho_l = 1.7 \, \varepsilon^l / rb$ and thus the local flow stress (σ) was given by the expression:

$$\sigma = \alpha \mu b (\rho_l)^{1/2} \cong 1.3 \alpha \mu (\frac{\varepsilon^l b}{r})^{1/2} \qquad (2.27)$$

where μ is the shear modulus, b is the Burger's vector, ε^l is the maximum plastic strain and α is a constant lying between ~1/3 and 1/7. The presence of particles imposes a local plastic constraint on the matrix thus elevating the local stress on the particle interface by a factor which has been estimated to be ~4.2[45,64]. Consequently, the elevated local stress on the particle interface is given by[54]:

$$\sigma_E \cong 5.4 \alpha \mu (\frac{\varepsilon^l b}{r})^{1/2} \qquad (2.28)$$

The maximum stress σ_T on the particle interface is therefore the sum of the elevated local stress σ_E and the macroscopic mean-normal σ_m and maximum devatoric S_1 stresses :

$$\sigma_T = S_1 + \sigma_m + \sigma_E \qquad (2.29)$$

Hence the critical condition for void nucleation by decohesion of the matrix/particle interface is given by :

20

$$S_1 + \sigma_m + \sigma_s = \sigma_c \qquad (2.30)$$

Where σ_c is the critical cohesive strength of the interface. By developing approximate expressions for the macroscopic flow stress $(S_1 + \sigma_m)$[54,64] it can be shown that the critical strain ε^{in} required to nucleate voids by particle decohesion is given by :

$$\varepsilon^{in} = Kr\,(\sigma_c - \sigma_m)^2 \qquad (2.31)$$

where K is a material constant related to the volume fraction of particles. Support for the validity of the critical strain equation is obtained from experimental results for a number of spheroidized steel specimens[39].

A model of void growth in plastic flow fields was developed by Rice and Tracey[55]. The results for the rates of change R in the radius R of the void were shown to have the form :

$$\dot{R} = [\gamma\dot{\varepsilon} + 0.56\dot{\varepsilon}\sinh(\frac{2\sigma_H}{3\sigma})]\,R \qquad (2.32)$$

where $\dot{\varepsilon}$ = the strain rate,

   σ_H = the hydrostatic stress,

   σ = the flow stress, and

   γ = the amplification factor, 1-2, relating the growth rate of void to the strain.

21

The confirmation of the validity of the Rice-Tracey equation for void growth has been obtained by Le Roy et al.[39] who carried out a numerical integration of the Rice-Tracey equations to give estimates of the changing area-fraction of voids A_f on a microsection, with increasing plastic strain. The theoretical results[39] were obtained for tension tests on materials which were assumed to display a continuous linear increase in void nucleation. There was found to be good agreement for the low-, medium-carbon steels up to a strain of $\varepsilon \sim 0.6$ between the experimental and theoretical results.

2.4. Wear Debris Morphology and Formation

Wear debris as one of the important sources of information to understand the wear process was under investigation[65-79]. Wear debris may consist of spheres, flakes, plates, ribbons, irregular clusters, and oxide particles. The size of wear debris may range from tens of nanometers to centimeters.

Thin, flake-shape debris with thickness about one-tenth of the lateral dimensions are usually produced during delamination wear. Suh and his colleagues[15,66] have developed the delamination theory of wear to explain the formation of this type of debris. The main points of this theory can be summarized as below:

(i) Normal and tangential forces are first transmitted through contacting points, which deform to smooth the surface,

(ii) Plastic strain accumulates in the surface layers with repeated loading,

22

(iii) Cracks are nucleated below the surface layer since triaxial compressive stresses exist in a zone close to the surface.

(iv) Cracks extend and propagate with further loading.

(v) Subsurface layers delaminate to produce the long and thin plates when cracks shear to the surface (Fig.2.8).

However, by careful characterization of the debris and of the near-surface material (copper), Rigney et al[24] found that the delaminated material was not the same (either structurally or chemically), as the base material. Loose flake debris is commonly derived from a very fine-grained transfer layer. They[68] also developed a model to predict the thickness of flake debris.

Other workers have presented some different mechanisms. Kayaba and Kato[75] found that flake-like debris was ejected at the leading edge of a hard tool that is made to slide across the surfaces of a softer material. They proposed the mechanism illustrated schematically in Fig.2.9. A plastic zone, ABC, develops early during the interaction between two asperities and that shear displacement occurs along AC, creating a shear tongue 'CC. The plastic zone is then transferred to a lower layer, and the process is repeated to produce several layers of shear tongues. When a crack eventually develops at the sharp cusp at the root of the tongues, a fragment combining with a series of plates detaches from the surfaces and individual plates subsequently separate.

Many other types of debris have been found including sphere, ribbon, irregular cluster, oxide debris etc[72-76]. Oxide debris are composed of particles and plates, which are small and thin, a few micrometers to a fraction of a micrometer. Quinn[78] has proposed an oxidational theory of wear. At a first stage, oxide films are formed at the real areas of contact at certain contact temperatures. When this film reaches a critical thickness, (usually 1-3 μm), and becomes mechanically unstable, it flakes off. The sequence is shown in Fig.2.11.

In summary, the removal of debris can be attributed to the crack nucleation and propagation in highly deformed layer on subsurface. However, in addition to the subsurface delamination mechanism attention should also be given to debris formation by surface oxidation and mechanical alloying.

2.5. Effect of Prior Deformation on Wear

In abrasive wear, Kruschov[80] found that abrasive wear of metals was very little influenced if they were hardened by plastic deformation such as cold work before abrasion. Thus, the abrasion resistance of cold-worked metals was independent of the degree of cold working. In his studies, a number of pure metals in annealed state were tested including lead, tin, aluminum, zinc, copper, nickel, iron, cobalt, chromium, titanium, molybdenum. Also, the carbon steel under both heat treated and annealed states, some bronzes and carbon steels in cold worked condition were examined. The

experiments led to the conclusion that a material surface during abrasion reached a maximum work-hardened state, i.e., a limiting hardness and flow stress (a saturation value), regardless of what kind of deformation had been applied previously.

In Larsen-Badse's studies[81], the resistance to dry sliding abrasion has been measured in some hardened and tempered carbon steels. He found the abrasion resistance varied linearly with both the bulk hardness of material and the microhardness of the worn surface, and it also, could be related to the exponent of work hardening, n. For tempered steels containing a dispersion of cementite in ferrite, wear resistance (R) was related to the volume of cementite (f) and the radius of the cementite particles (r)

$$R = \frac{K}{r} f^{3/2} + R_{Fe} \qquad (2.33)$$

where K is a constant and R_{Fe} is the wear resistance of ferrite. The analysis of hardened and tempered carbon steels indicated that the abrasion resistance increases less rapidly with material hardness than that for the pure metals. It was concluded that heat treatment which raised the bulk hardness of steels resulted in the increase of microhardness of abrasion surface.

Richardson[82] found that increasing the hardness of annealed metals by moderate cold rolling (50% reduction in thickness) produced little effect on their abrasive wear resistance. In addition, Avery[83] showed that prehardening austenitic Mn steel by

25

deformation had a negligible effect on its abrasive wear rate.

However, the detailed microscopic studies on this topic are lacking. In order to obtain further information on the mechanisms of wear of materials with and without prior plastic deformation for sliding wear, the microstructural changes during wear as well as strain-stress behavior of deformed layers should be investigated in more detail.

Chapter 3. EXPERIMENTAL METHODS

3.1. Material And Heat Treatment

Wear tests were performed on commercial purity copper samples (99.9%) in annealed and cold rolled conditions. A bar of commercial purity copper (99.9%) was annealed at 600 °C while being immersed in Al_2O_3 powder to prevent oxidization. The material was subsequently cooled inside the furnace. Half of the annealed copper bar was cold rolled to 50% reduction in thickness. The microhardness of specimens are listed in Table 3.1. Specimens machined for wear tests were 10 mm long, 10 mm wide and 5 mm thick. In order to keep the applied stress constant during the initial stages of wear tests, a curved surface (with a radius of 19 mm which is equal to the radius of the test ring) was machined on the testing surface.

3.2. Wear Set-up

The sliding wear test machine was a block-on-ring type as shown in Fig.3.1. The main components of the wear machine consisted mainly of a rotating ring and an arm used to hold the specimen above the ring. The speed of the ring can be adjusted by a speed controller connected to the motor. The test time can also be automatically set by a timer. The ring was made by 52100 bearing steel.

The specimen was firmly fixed on the top of the ring by clamping through the notch in the arm to prevent relative movement and to ensure good alignment between specimen and ring.

For all the wear tests, the normal load was provided by the weights placed on the top of specimen and the speed of ring was measured by a digital tachometer.

3.3. Experimental Procedure

3.3.1. Specimen Preparation for Wear Test

Before each test, the test surfaces of the block and the ring were ground, and then polished to 0.5 μm using alumina slurry. The surfaces were then ultrasonically cleaned in trichoroethane, methanol and acetone to remove any organic residue. While placing the specimen in position, it was ensured that the edge of the specimen was parallel to the edge of the ring and that the mating curved surfaces of the specimen and the ring were perfectly aligned.

3.3.2. Wear Test

Two types of tests were performed:
(1) weight loss from the surface of specimens was determined as a function of sliding

distance at constant load (1535 g) and sliding speed (0.20 m/s),

(2) weight loss at two constant sliding distances (1782 m at a sliding speed of 0.12 m/s, 2800 m at a sliding speed of 0.20 m/s) was determined at the following applied load levels: 310, 500, 954, 1500, 2060 g.

All tests were repeated and two test results were averaged to obtain the mean value.

Prior to each test, the specimen was weighted to the nearest 1×10^{-4} g by a balance. The weight loss during the wear tests was evaluated to calculate wear rates by the following expression

$$WearRate(W_R) = \frac{WeightLoss}{SlidingDistance} \qquad (3.3)$$

The weight of the worn specimens was measured after removing the loose debris from the worn surface using methanol, acetone in an ultrasonic cleaner.

All tests were carried out in normal laboratory air at a temperature of 18 to 21 °C and a relative humidity of 40 to 50%.

3.4. Measurements of Strain and Microhardness below the Worn Surfaces

3.4.1. Microhardness Gradient Measurements

The two most common microhardness measurements are the Knoop and Vickers tests. The Knoop indenter is more suitable for testing the microhardness of narrow features or thin layers of materials due to its shallower penetration. On the other hand, taper sectioning is an effective method for enhancing the resolution of fine details in deformed layers below the worn surfaces. Therefore, in this work, the Knoop indenter was used on tapered sections of worn specimens for the microhardness gradient measurement. The principles of taper sectioning are illustrated in Fig.3.2.

The tapered sections were prepared with extreme care to minimize artifacts in the region of interest. After wear test, the worn surface of the cleaned specimen was covered with an acetone soluble lacquer. Next the specimen, held by a special clip was cut by low speed saw at a angle (α) of about 10 degrees to the worn surface. Then, the surface of the cut section was polished to 0.5 μm. After polishing, the exact value of α was accurately measured under the optical microscopy with a graduated lens (accuracy of 0.1 μm) in microhardness test machine. The contact surface was moved first normal and then parallel to the hairline marker in the microscopy. Both distances which form orthogonal sides of a triangle with a segment of the taper section were measured. The value α was calculated by taking the tangent of these two distances.

The Knoop microhardness measurements were carried out on Micromet II Microhardness Tester made by Buehler Ltd. Tests were performed with a 25 gram load, and test time of 15 seconds. Three readings were taken at a certain distance from the

30

worn surfaces on the tapered section for each hardness determination. These were averaged to find the mean hardness value.

3.4.2. Measurements of Strain Gradients and Thicknesses of Plastically Deformed Layer

To measure the strains below the worn surface, a foil-slit method was developed. A piece of copper foil (400 μm-thick, 3 mm-wide and 5 mm-long) with the same condition as specimen itself was inserted into 400 μm-thick slit in the specimen perpendicular to wear surface. Thus, an artificial interface perpendicular to contact surface has been obtained (Fig.3.3).

At the end of the experiment, the specimens were sectioned through the center of the foil in a plane parallel to sliding direction. The sectioned specimens revealed the distortion of the interface in sliding direction (Fig.3.3).   .

The thickness of plastically deformed layer below the worn surface was determined by noting the largest depth at which any measurable forward displacement was displayed by the bent interface. The plastic strain distribution below the worn surface was estimated from the shear angle θ of the curved interface (Fig.3.3). Using the method proposed by Dautzenberg and Zaat[51], the plastic strain was estimated using:

$$e = \frac{\sqrt{3}}{3} \tan\theta \qquad (3.2)$$

31

3.5. Metallography of Worn Surfaces

Following the wear tests, the morphology of the worn surfaces cleaned using methanol and acetone ultrasonically was analyzed by a Semco Nanolab7 scanning electron microscope (SEM).

The cross sections were prepared with care to avoid artifacts following the technique proposed by Ahn et al[84]. The wear surface was covered with acetone soluble lacquer. The lacquer coating was used both for

(1) protection of the worn surface from etching attack,

(2) retention of edge during mechanical polishing.

The specimen was then cut by a low speed saw. Then, the cut sections were mounted in a special clip and polished to 0.5 μm. After that, lacquer coating was removed by dissolution in acetone in an ultrasonic cleaner. The cut sections were etched with an etchant whose composition was summarized in Table 3.2. The specimen was placed in an inclined position in the scanning electron microscope to examine both the worn surface and the cross section at the same time.

The wear debris was collected after each test. The debris particles were coated with aluminum for observation in SEM. Elemental composition of the debris v/as analyzed with a energy dispersive X-ray analysis (EDX analysis) and X-ray diffraction.

Chapter 4. EXPERIMENTAL RESULTS

The focus of the work is on the investigation of plastic deformation below the worn surfaces and the effect of prior deformation on sliding wear. The results are presented into two sections:

(1) experimental results and observations on annealed Cu,

(2) experimental results and observations on 50% rolled Cu.

4.1. Experimental Results and Observations on Annealed Cu

4.1.1. Metallographic Observations on the Worn Surfaces and Microstructure Adjacent to the Worn Surfaces

Observations on the worn surfaces are carried out to study the wear mechanisms that operate during the wear process. For this reason the worn surfaces are periodically examined by the SEM after wearing to several sliding distances.

The worn surface topography is characterized by surface deformation and damage. Fig.4.2 shows a crack propagating on the worn surface. These surface cracks propagate in a direction perpendicular to the sliding direction.

Figure 4.3 shows delamination of material adjacent to the worn surface. It is noted that the detachment occurs at the rear end of the delaminating material. This process leads to the generation of flake like loose debris plates. Some areas on the worn surface are covered by the oxide layers (Fig.4.4). The extent of oxide covered areas increases with sliding distance.

SEM metallographic investigations on the cross sections parallel to the sliding direction (Longitudinal Section, i.e., L.S.) indicate that at the beginning of wear process, the microstructure just below the wear surface is comprised of a thin deformed layer, about 8 μm as shown in Fig.4.5. The deformation is revealed by the distortion of grain boundaries towards the sliding direction. With increasing sliding distance, the deformed layer penetrates deeper in the material. The thickness of this layer increases to about 15 μm (Fig.4.6). There are also some cracks as shown in Fig.4.6, about 10-100 microns long. Two debris particles almost detached from surface are clearly seen. Fig.4.6.b. shows another example of subsurface deformation and crack propagation in the sliding direction.

After a certain sliding distance (420 meters), the thickness of deformed layer reaches a constant value of 50 microns (Fig.4.7). After that, no further increase in the depth of the deformed layer has been observed.

On the transverse section, the microstructure below the wear surface is characterized by elongated elliptical grains and subsurface cracks. The thickness of the

34

highly deformed layer is also estimated from the depth at which the distorted grains are observed (Fig.4.8).

At a higher magnification, the grain structure indicates the localization of deformation in the form of shear bands (Fig.4.9).

4.1.2. Quantitative Determination of Microhardness and Strain Gradients Below the Worn Surfaces

In the present work, microhardness and strains below the wear surface were measured to determine quantitatively the extent of plastic deformation as a function of sliding distance.

A micrograph of Knoop microindentations taken on a tapered section as shown in Fig.4.10 indicates the microhardness increases when approaching to the worn surface. The microhardness profiles below the wear surface were obtained at two different sliding distances as shown in Fig.4.11 (based on data in Appendix A1). The maximum microhardness is attained at the worn surface and decreases rapidly with depth to the bulk hardness (70 kg/mm^2). The microhardness values near the worn surfaces increase with sliding distance. The microhardness value at depth of 7 microns below the worn surface is 140 kg/mm^2 at the sliding distance of 36 meters and this becomes 170 kg/mm^2 at 720 meters. According to the microhardness profiles, the thickness of plastically deformed

layer can be estimated, 15 μm and 60 μm for the sliding distances of 36 m and 720 m, respectively.

As explained in section 3.4 the strains below the worn surfaces are followed by measuring the displacements of an interface created using a foil-slit method. Although the gradients were also revealed by the distortion of grain boundaries, this method of measurement was developed because it provides an accurate way of determining the subsurface displacements. The original interface perpendicular to the worn surface becomes curved in sliding direction during the wear process. The displacements of interface at the sliding distances of 0, 36, 720 meters are shown in Fig.4.12. Fig.4.13 shows the increase in the displacement gradients below the worn surface as a function of sliding distance. The equivalent strains calculated using equation 3.2 are shown in Fig.4.14 (see data in Appendix A2). Figure 4.14 indicates the following results:

(1) at any given sliding distance strain increases rapidly when approaching the worn surface;

(2) the magnitude of strain gradients increases with sliding distance. For instance, at a depth of 7 microns below the worn surface, strain increases from 0.20 at sliding distance of 36 meters to 1.22 at 720 meters;

(3) assuming that the deformed layer beneath the wear surface is defined as a zone with minimum equivalent plastic strain larger than 0.01, it is found that the thickness of deformed layer increases with sliding distance until it reaches to a constant value of 50 microns in Fig.4.15.

In summary, strain and microhardness measurements indicate that an accumulated process of plastic deformation occurs below the worn surfaces. The magnitudes of both strains and microhardnesses increase with sliding distance; the thickness of deformed layer also increases with sliding distance until it reaches to a constant value.

4.1.3. SEM Observations and X-ray Studies on Wear Debris

In the section 4.1.1, it is shown that the formation of wear debris includes delamination, fracture and oxidization processes in material layer near the worn surfaces. Thus, it is worth investigating the morphology and composition of the wear debris.

There are two main morphologies in the collected debris. One is the flake-shape metallic debris and the other is oxide particles. The top and side views of a typical flake-shape debris are shown in Fig.4.16. The side view indicates that the flake-shape debris has a uniform thickness of 5 microns. With further increase of sliding distance, debris is a mixture of metallic flakes and oxide particles in Fig.4.17. The morphology of the oxide particles are shown in Fig.4.18.

X-ray diffraction of the debris yields the peaks shown Fig.4.19. (The analysis data are listed in Appendix A3). The dominant peak is for CuO. The remaining peaks are those for α-Fe_2O_3, Cu, Fe_2CuO_4. In addition, using EDX analysis, small amount of Fe flake debris is found (Fig.4.20).

4.1.4. Results on Wear Rates

The wear rates are calculated from the weight loss data in Appendix A4 using equation 3.1. The dependence of wear rates on sliding distance is shown in Fig.4.21 (also see Appendix A5). Initially, the wear rates decrease rapidly with sliding distance. At sliding distance of about 500 meters, the wear rates reach a constant value. That correlates well with the sliding distance at which the depth of plastically deformed subsurface material reaches a constant value.

4.2. Experimental Results and Observations on 50% Rolled Cu

4.2.1. Metallographic Observations on the Worn Surface, Subsurface adjacent to the Worn Surface and Wear Debris

The surface topography of the 50% rolled Cu indicates the features similar to those observed in the annealed Cu. These are deformation of the surface and delamination of surface layers (Figs.4.22-4.24).

On the transverse section, elliptical grain shape and some propagated cracks below the worn surface can be clearly observed (Fig.4.25 and Fig.26).

Two different morphologies of debris are observed in rolled Cu. These are the flake-shape debris and oxide particles in Figs.4.27, 4.28. The side view of debris indicates that the thickness of flake-shape debris is of the order of 5-10 microns.

The oxide debris consist of fine particles of 3-5 microns (Fig.4.28). The X-ray diffraction and EDX analysis indicate that CuO, α-Fe$_2$O$_3$, Fe$_2$CuO$_4$ are the main constituents of the oxide debris (Appendix A6).

4.2.2. Strain and Microhardness Results from Rolled Cu below the Worn Surface

The microhardness profiles are shown in Fig.4.29 (data in Appendix A7). The microhardness decreases with depth to the bulk hardness value (100 kg/mm^2) from the maximum value at the worn surface. The microhardness at a certain depth below the worn surfaces increases with sliding distance. However, the thickness of the deformed layer is about 30 microns after sliding distance of 720 meters.

The magnitude of displacements below the worn surfaces are shown in Fig.4.30. The data on the equivalent strain are listed in Appendix A8. Figures 4.31, 4.32 show that the magnitude of strain and the thickness of deformed layer increases with the sliding distance.

The strain and microhardness measurements show that the magnitudes of strain

and microhardness as well as the thickness of deformed layer increase with sliding distance for rolled Cu. The difference between annealed and rolled Cu is in the constant value of the thickness of deformed layer. The smaller constant value of rolled Cu, 28 microns, is compared with that, 50 microns of annealed Cu.

4.2.3. Wear Rates

To consider the effect of prior deformation on sliding wear, wear tests are conducted with the change of the applied normal load for both rolled and annealed Cu. From Fig.4.33, it should be noted that the wear rates of rolled Cu are about 3-4 times higher than that of annealed Cu beyond the normal load of 1500 grams. In addition to tests at 1500 grams, wear tests are conducted at other loads ranging from 300 to 2000 grams on annealed and 50% rolled coppers. The measurements are made after the wear rates reach to a constant value (i.e., at a sliding distance of 1500 meters). Figure 4.33 shows that the wear rates of the 50% rolled copper specimens exceed those of the annealed specimens. For instance, at a normal load of 1500 g, the wear in the rolled specimens occurs at a rate three times faster than those in annealed samples.

The wear rates decrease with sliding distance(Fig.4.34).

Chapter 5. DISCUSSION

According to SEM and X-ray diffraction analyses, the principal features of sliding wear in copper can be summarized as follows:

(1) There are large strains on the worn surfaces and severe strain gradients in the plastically deformed layers below the worn surfaces. The largest strain near the surface is around 8 at sliding distance of 720 meters. This value is much larger than the fracture strains attained in tensile testing of copper ($\varepsilon = 0.5$). However, the large strains below the worn surfaces are comparable to those obtained in cold working processes that generate strains in the range of 1 to 4[26].

(2) According to the strain and microhardness distributions below the worn surfaces, it is found that the magnitudes of both the subsurface strain gradients and the microhardness gradients increase with sliding distance. This indicates that the subsurface layers are progressively strain hardened. The thickness of the deformed layers increases from 12 μm to 50 μm when sliding distance increases from 36 to 720 meters, thereafter remains constant. This shows that plastic deformation is localized in a thin layer below the worn surfaces.

(3) The maximum degree of damage appears to occur at some critical depth below the worn surfaces. It can be suggested that shear localization initiates the events leading

41

to subsurface crack formation. A shear band is considered to propagate by the growth and coalescence of the voids along a strain gradient. The void growth near the worn surfaces is considered to be suppressed by the hydrostatic stresses whose maxima are at the worn surfaces.

In this section, stress-strain behavior in the plastically deformed layer below the worn surfaces will be analyzed quantitatively. A model of subsurface delamination phenomenon will be given thereafter.

5.1. Work Hardening Behavior Below the Wear Surface

Based on the microhardness data, the flow stresses are estimated using a simple expression derived by March[85]:

$$\sigma - \frac{1}{3}H \tag{5.1}$$

Where σ is the flow stress, H is the hardness value. This relation was tested using various work-hardened metals and has been shown to a rapid and reliable estimation of flow stresses[85]. Using equation 5.1 the average flow stress of the deformed layers as a function of depth below the worn surfaces are calculated for a set of sliding distances. The average flow stress values are then plotted as a function of equivalent strains (from

42

Fig.4.14). In this way, the stress-strain curves as shown in Fig.5.1 are obtained. It is seen that as wear proceeds strains become larger and the flow stress of the deformed layers is pushed up to higher values.

The Voce equation[29] in section 2.2.1 is a commonly accepted expression of the stress-strain behavior of materials subjected to large strains:

$$\sigma - \sigma_s - (\sigma_s - \sigma_o)e^{-e/e_c} \qquad (2.24)$$

Where σ is the flow stress at strain ε; σ_o is the yield stress; σ_s is a saturation stress where work hardening rate, $d\sigma/d\varepsilon = 0$; ε_c is a constant. The best fit parameters for the annealed and rolled Cu are given in table 5.1. It is found that the experimental results are not in good agreement with the Voce equation particularly at large strains, above 2.0 (Fig.5.2).

An alternative approach is to use the Embury-Fisher exponential equation[30] discussed previously. The Embury-Fisher equation in section 2.2.1 is simplified by:

$$\sigma - f[\exp(\frac{e}{4})] \qquad (2.25)$$

where ε is the strain at the flow stress σ. As seen in Fig.5.3, there is a large difference

between the experimental results and the predictions based on the Embury-Fisher equation.

The stress-strain curve for metals is often described by the power expression (section 2.2.1) generally attributed to Hollomon[28]:

$$\sigma = K\varepsilon^n \qquad (2.23)$$

where K and n are empirical constants. It is found that the power expression is in a reasonable agreement with the results. The numerical values of these constants in equation 2.23 are listed in table 5.2 (see the curves represented by the solid and dash lines in Fig.5.1).

The equation 2.23 can be differentiated to obtain the work hardening rates:

$$\frac{d\sigma}{d\varepsilon} = nK(e)^{n-1} \qquad (5.2)$$

Fig.5.4 shows the variation in work hardening rate with strain. The material near the worn surface ($\varepsilon > 2$) has a very low work hardening rate (100 MPa) with respect to the layers further below in the plastically deformed layer. This can also be seen in Fig.5.5 in which the work hardening rates ($d\sigma/d\varepsilon$) are plotted against the depth below the worn surfaces.

According to the above discussion, it is seen that the local flow stress of the material within the plastically deformed layer increases to a value three times higher than that of the strength of undeformed bulk materials (for instance, 600 MPa at sliding distance of 720 meters). At large strains ($\varepsilon \geq 1$) the work hardening rates decrease to low values and become almost constant. This indicates that the material loses its ability to maintain further work hardening and consequently plastic deformation becomes heterogeneous. This leads to the development of instabilities resulting in the crack nucleation of the shear bands.

For rolled Cu, the flow stress vs strain curves below the worn surfaces are plotted in Fig.5.6 as described for annealed Cu (Fig.5.1). Neither the Voce nor the Embury-Fisher equation is in accord with the experimental results shown in Figs.5.7, 5.8. But, Fig.5.6 indicates that the power equation is a reasonable approximation of the data. The curves of work hardening rates vs strain and depth below the worn surface are presented in Figs.5.9, 5.10. As expected the work hardening rates also decrease rapidly near the worn surfaces as in the present of specimens. However, at smaller strains ($\varepsilon \geq 1$), the work hardening rates diminish to lower values than those of the annealed Cu. This may be due to the effect of prior deformation in this material to reduce the subsequent ability of material deformation during wear (see section 5.4 for a detailed discussion of this point).

5.2. Damage Accumulation

45

In the earlier discussion on the stress states (section 2.1.2), it was shown that a severe hydrostatic stress gradient may exist below the contact surfaces. As indicated by Bridgeman[86], a large hydrostatic compressive stress should improve the ductility by retarding the voids that tend to nucleate and propagate under the influence of plastic strain gradients. In the areas adjacent to the worn surfaces, damage initiation is made difficult by the large hydrostatic stresses. On the other hand, at a larger depth, the plastic strain is small, so the driving force for nucleation is negligible. Thus, the competition between the hydrostatic stress and large plastic strain would determine a damage gradient with a maximum at a certain distance below the worn surface. The void growth will reach to a maximum rate at this critical depth.

The growth of damage takes place by coalescence with neighboring voids to form the crack and propagate further parallel to the worn surfaces. When the subsurface cracks have reached the worn surface, flake-shape debris may become detached from the surface to result in the removal of materials on the surface.

In the beginning of wear process, the accumulation of plastic deformation occurs in a very narrow vicinity below the worn surfaces, for instance, 12 μm at sliding distance of 36 m for annealed Cu according to the strain distribution (Fig.4.14). Assuming that the critical strain for maximum rate of damage can be determined directly from the strain distribution. For both annealed and rolled coppers, the critical depth is 4 μm very close to worn surfaces at sliding distances at 36 meters. With further increase of sliding

46

distance, the plastic strain accumulation goes to the larger area below the worn surfaces; the critical depth also moves deeply. Both of them reach constant values, where the critical depth becomes 12 μm for both copper, meanwhile, the thickness of deformed layer becomes 50 μm for annealed copper and 28 μm for rolled copper. Therefore, the critical strain changes with depth, sliding distance, which leads to the larger critical depth for maximum damage rate (Fig.5.11).

For copper with very good ductility, where crack nucleation or damage initiation can readily occur, crack propagation may be the controlling mechanism[11]. Due to the crack nucleation very close to the worn surface at the beginning of the test, the way is short for subsequent crack propagation to reach the worn surfaces. This process results in the faster crack propagation and delamination for the formation of loose debris compared with that when increasing sliding distance (Fig.5.12). Hence, the higher wear rates at the beginning may be mainly attributed to the fast damage accumulation.

For rolled copper, the critical depth almost is the same as that of annealed copper at certain sliding distance. The inferior ductility of rolled copper increases the rate of crack propagation. This may be one reason to increase the damage rate and wear rate.

It is considered that the propagation and coalescence of the voids constitute the first stage of the delamination. The process of damage accumulation results in the formation of subsurface cracks. When these cracks reach to the worn surface, a flake-

shape debris is detached from the surface (see Figs.4.3 and 4.24).

5.3. A Model For Delamination Wear In Ductile Materials

According to the above discussion, a model is proposed to estimate the critical depth for maximum rate of damage accumulation. Consider that a void of size, R, has nucleated. The growth rate (R) of the void can be obtained from the Rice & Tracey's equation[55].

$$\frac{\dot{R}}{R} - [\gamma + 0.56\sinh(\frac{3\sigma_H}{2\sigma})]\dot{\epsilon} \qquad (2.32)$$

where $\dot{\epsilon}$ is the strain rate; σ_H is the hydrostatic stress; σ is the flow stress; γ is the amplification factor, (1-2), relating the growth rate of void to the strain.

Some assumptions are made to simplify the model:

(1) the strain rate $\dot{\epsilon}$ is linearly proportional to the strain. Since the relation between the strain (ϵ) and depth (Z) can be expressed as (from Fig.4.14)

$$\epsilon - Dexp(BZ) \qquad (5.3)$$

then,

$$\dot{e} - Ge - GD\exp(BZ) \tag{5.4}$$

where G, D and B are constants; Z is the depth below the worn surfaces. The strain

rate is lineared to further simplify exp(BZ) using Taylor's expansion.

$$e^x - 1 + x + \frac{x^2}{2!} + \cdots + \frac{x^n}{n!} \tag{5.5}$$

then,

$$e^x \cong 1 + x \tag{5.6}$$

Thus

$$\dot{e} - GD(1 + BZ) \tag{5.7}$$

(2) The variation of hydrostatic stress in the highly work hardened material can be

estimated from the elastic solution on point load[21]. Thus,

$$\sigma_H - \frac{C}{Z^2} \tag{5.8}$$

where C is a constant.

(3) The flow stress as a function of depth can be obtained from the data of microhardness

gradients below the worn surfaces. Thus,

$$\sigma - E(Z)^A \qquad (5.9)$$

where E and A are empirical constants.

(4) Taylor's expansion is applied to simply $\sinh(3\sigma_H/2\sigma)$ term in equation (2.32), that is:

$$\sinh x - x + \frac{x^3}{3!} + \cdots + \frac{x(2n+1)}{(2n+1)!} \qquad (5.10)$$

Thus,

$$\sinh\frac{3\sigma_H}{2\sigma} \approx \frac{3\sigma_H}{2\sigma} \qquad (5.11)$$

Based on the above assumptions, the damage rate is given by:

$$\frac{\dot{R}}{R} - GD[\gamma + \gamma BZ + 0.56B\frac{3C}{2E}(Z)^{-1-A} + 0.56\frac{3C}{2E}(Z)^{-2-A}] \qquad (5.12)$$

The maximum rate of damage occurs when:

$$\frac{d}{dZ}[\frac{\dot{R}}{R}] - 0 \qquad (5.13)$$

50

Taking the derivation of equation 5.12, we obtain:

$$\frac{d}{dZ}[\frac{\dot{R}}{R}]-GD[\gamma B-0.56(1+A)B\frac{3C}{2E}(Z)^{-2-A}-0.56(2+A)\frac{3C}{2E}(Z)^{-3-A}]=0 \quad (5.14)$$

Rearranging the equation (5.15), we can find an expression for C:

$$C=\frac{\gamma B(Z)^{3+A}}{0.56(1+A)B\frac{3}{2E}(Z)+0.56(2+A)\frac{3}{2E}} \quad (5.16)$$

The constants in the equation (5.15) are listed in table 5.3 by taking $\gamma = 1.5$. Hence, the following equations are obtained:

For annealed Cu at a sliding distance of 36 meters,

$$C=\frac{0.884Z^{2.664}}{4.487\times10^{-4}Z-1.909\times10^{-3}}. \quad (5.16)$$

For annealed Cu at a sliding distance of 720 meters,

$$C=\frac{0.375Z^{2.661}}{1.349\times10^{-4}Z-1.356\times10^{-3}} \quad (5.17)$$

51

For rolled Cu at a sliding distance of 36 meters,

$$C - \frac{0.766Z^{2.850}}{4.746 \times 10^{-4}Z - 2.022 \times 10^{-3}} \qquad (5.18)$$

For rolled Cu at a sliding distance of 720 meters.

$$C - \frac{0.417Z^{2.883}}{2.674 \times 10^{-4}Z - 2.051 \times 10^{-3}} \qquad (5.19)$$

There is no exact value of C, however, the different values of C have been substituted into the equation to obtain the critical depth Z^* at which the damage rate is maximum. The critical depth Z^* values as a function of C are listed in table 5.4. As shown in Fig.5.13 there are an upper and a lower limit for the critical depth. Therefore, a range of possible Z^* values can be obtained. The Z^* values range between 5.7 - 7.3 micrometers at a sliding distance of 36 meters and 14.4 - 16.8 micrometers at a sliding distance of 720 meters. Thus, the critical depth Z^* becomes larger when increasing the sliding distance.

5.4. Effect of Prior Deformation on Sliding Wear

Most of the previous work suggested that the wear resistance of metal was very little affected if they were work hardened before the wear test[80-8?]. Richardson[82] proposed that this was because the materials reached a limiting hardness and flow stress during wear, no matter what kind of work-hardening was applied previously.

In this work it is observed that the wear resistance of rolled Cu is poorer than that of annealed Cu especially under the conditions where loads exceeding 1000 grams are applied (see Fig.4.34).

In order to understand why the resistance of rolled Cu is poorer than that of annealed Cu, an energy-based model is put forward.

The main assumption is that the friction work (W_f) performed during the sliding wear is equal to the sum of

(1) the work of plastic deformation (W_p);

(2) the work of crack nucleation and propagation (W_c); and

(3) the energy dissipated as friction heat (Q).

That is shown in equation 5.20:

$$W_f = W_P + W_C + Q$$ (5.21)

It is assumed that the friction work for annealed Cu and rolled Cu is the same. The wear debris has the same composition and oxide content regardless of the amount of cold work applied. Hence, the temperature increase during sliding wear should be approximately equal in these materials. The same friction heat produced during wear is assumed for annealed Cu and rolled Cu.

The work of plastic deformation can be expressed by

$$W_P = \int \int \sigma d\varepsilon dV \tag{5.21}$$

where σ is the flow stress; ε is the equivalent strain; and V is the deformed volume below the worn surface. To simplify the discussion, assume that the longitudinal section of deformed area is a segment of a circle as shown in Fig.5.15. Since the thickness (l) of specimens is fixed, 5 mm, the volumes of the deformed regions below the worn surface for annealed and rolled coppers are constant. Thus,

$$W_P = V \int \sigma d\varepsilon \tag{5.22}$$

The σ-ε equations based on eq.(2.23) and parameters in table 5.2 can be expressed by

$$\sigma_A = 455.0(\varepsilon)^{0.188} \tag{5.23}$$

$$\sigma_R = 502.2(e)^{0.129} \qquad (5.24)$$

where σ_A is the flow stress for annealed Cu; σ_R is the flow stress for rolled Cu; and ε is the equivalent strain.

The plastic deformation work per unit volume is

$$W_{P_{V_A}} = \int \sigma de \qquad (5.25)$$

Substituting eq.(5.23) and eq.(5.24) into eq.(5.25), then, integrating eq.(5.25), it is obtained that,

for annealed Cu,

$$W_{P_{V_A}} = \int_{0.02}^{8.27} [455.0(e)^{0.188} - 235.3] de = 2766.9 (MPa) \qquad (5.26)$$

for rolled Cu,

$$W_{P_{V_R}} = \int_{0.02}^{7.8} [528.8(0.67e)^{0.129} - 329.0] de = 1728 (MPa) \qquad (5.27)$$

The deformed volume is calculated as below,

$$V - A \cdot l \tag{5.28}$$

where A is the deformed area on the longitudinal section shown in Fig.5.14, 1 is the thickness of specimen, 5 mm. Due to the assumption, the area is given by:

$$A - \frac{1}{2}(R_1^2 - R_2^2) \theta \tag{5.29}$$

where R_1, R_2, θ are described in Fig.5.15 and their values are listed in table 5.5. Thus, the deformed volume is,

for annealed Cu,

$$V^A - A^A \cdot l - 0.1468 \times 5 - 0.734 (mm^3) \tag{5.30}$$

for rolled Cu,

$$\tag{5.31}$$
$$V^R - A^R \cdot l - 0.1253 \times 5 - 0.6265 (mm^3)$$

Substituting eqs.(5.26) and (5.30) as well as eqs.(5.27) and (5.31) into eq.(5.22), respectively, the total plastic deformation work,

56

for annealed Cu

$$W_{P_A} - W_{P_{AV}} \cdot V^A - 2.03(N \cdot m) \tag{5.32}$$

for rolled Cu

$$W_{P_R} - W_{P_{RV}} \cdot V^R - 1.08(N \cdot m) \tag{5.33}$$

Therefore, it can be obtained that the plastic deformation work of annealed Cu is two times higher than that of rolled Cu, that is,

$$W_{P_A} - 2W_{P_R} \tag{5.34}$$

Due to some energy already stored in rolled Cu, it is clear that plastic deformation work expended during wear process of rolled Cu is lower than that of annealed Cu. A large proportion of the friction work in wear process of rolled Cu is converted into the work of crack nucleation and propagation.

Chapter 6. CONCLUSIONS AND RECOMMENDATIONS

6.1. Conclusions

(1) Sliding contact causes the accumulation of strain and microhardness gradients below the worn surfaces of copper.

(2) The magnitudes of strain and microhardness increase with sliding distance. The plastically deformed zones penetrate deeper in the material with increase of sliding distance.

(3) Exhaustion of strain hardening near the worn surfaces results in strain localization and formation of shear bands. The subsurface cracks propagate parallel to the worn surface and reach to the worn surface. This process leads to the formation of flake-shape wear debris.

(4) The increase of hardness and decrease of ductility of material due to prior deformation result in the thinner plastically deformed layer below the worn surface and easy occurrence of strain localization, crack nucleation and propagation, delamination adjacent to the wear surface, which lead to the lower wear resistance of material with prior deformation beyond the critical load.

(5) A Holloman equation is a reasonable approximation to the mechanical behavior in the plastically deformed layer.

(6) The critical depth Z^* for maximum rate of damage increases with sliding distance.

A model based on the Rice-Tracey equation has been developed to show that the location of maximum damage gradient dependent on a competition between the shear stresses and hydrostatic stresses.

6.2. Recommendations For Future Work

(1) Many inhomogeneities in the highly-deformed layer below the wear surface, e.g., dislocation cell boundaries, voids and microcracks, should be studied using TEM.

(2) A more refined description of residual stress beneath the wear surface could be attained with the help of X-ray diffraction analysis.

(3) For better understanding of prior deformation effect on sliding wear, the variation of subsurface microstructure below the critical load should be investigated in detail.

APPENDIX

A1. Microhardnesses below the Worn Surface for Annealed Cu

at Two Different Sliding Distances, 36 m and 720 m

Depth μm	Knoop Hardness kg/mm²	
	36 m*	720 m*
2.00	160.4	200.0
7.00	148.2	
8.00		170.3
10.00	102.0	
15.00		144.0
18.00	70.8	
20.00		118.9
22.00	71.0	
24.00	69.8	.
28.00		108.3
30.00	70.4	
34.00		98.5
36.00	68.5	
40.00		91.4
42.00	70.1	
46.00		82.2
52.00		75.5
58.00		70.6
64.00		68.6
70.00		70.6
76.00		67.5
83.00		71.6

*: Sliding Distance.

A2. Equivalent Strain below the Worn Surface for

Annealed Cu with 1535 g and 0.2 m/s

Depth μm	Equivalent Strain (ε)						
	ε^1	ε^2	ε^3	ε^4	ε^5	ε^6	ε^7
1.0	4.70	6.26	7.88	8.26	8.26	8.26	8.26
2.0	1.43	3.45	3.60	3.27	3.27	3.27	3.56
3.0	0.89	2.50	2.20	2.01	2.72	2.15	2.82
4.0	0.64	1.40	1.70	1.43	2.15	1.89	2.25
5.0	0.40	0.89	1.40	1.30	1.89	1.68	1.91
6.0	0.28		1.10	1.13	1.59	1.43	1.62
7.0	0.20	0.62	0.92	1.00		1.18	1.22
8.0	0.15	0.42	0.79	0.92	1.43	1.09	1.15
9.0	0.10					0.89	0.99
10.0	0.08	0.31		0.74	1.18	0.69	0.78
11.0	0.05		0.60				
12.0	0.03	0.27		0.52	1.00	0.58	0.63
14.0		0.13	0.44	0.40	0.86	0.47	0.52
16.0		0.11	0.36	0.37	0.64	0.39	0.46
18.0		0.09	0.21	0.33	0.53	0.33	0.38
20.0		0.07	0.17	0.28	0.42	0.27	0.33
22.0		0.05	0.14	0.21	0.33	0.22	0.26
24.0		0.01	0.12	0.17	0.29	0.19	0.22
26.0			0.10	0.13	0.22	0.16	0.19
28.0			0.07	0.11	0.19		0.17
30.0			0.05	0.09	0.15	0.13	0.15
32.0			0.03		0.13		
34.0			0.01	0.06	0.11	0.11	0.12
36.0					0.09		
38.0				0.03		0.09	0.10
40.0				0.01	0.07		
42.0					0.05	0.07	0.07
44.0							
46.0					0.03	0.05	0.05
48.0					0.01	0.03	0.03
50.0						0.01	0.01

Sliding Distance : 1. 36 m, 2. 84 m, 3. 156 m, 4. 216 m, 5. 300 m,

6. 420 m, 7. 720 m.

A3. X-ray Diffraction Peaks of Wear Debris from

Annealed Cu against 52100 Steel

Experimental Data			Card Data											
			Cu			CuO			α-Fe$_2$O$_3$			Fe$_2$CuO$_4$		
2θ	d(Å)	I/I$_1$	d(Å)	I/I$_1$	hkl	d(Å)	I/I$_1$	hkl	d(Å)	I/I$_1$	hkl	d(Å)	I/I$_1$	hkl
24.2	3.68	14.3							3.68	25	012			
33.1	2.69	65.7							2.69	100	104			
35.6	2.52	100				2.52	100	1$\bar{1}$1						
40.8	2.21	24.3							2.20	30	113			
43.4	2.09	37.1	2.09	100	111									
48.8	1.87	28.6				1.87	25	2$\bar{0}$2						
54.0	1.69	51.4							1.69	60	116			
57.6	1.60	18.6										1.59	50	511
62.2	1.49	31.4										1.49	100	404
63.8	1.45	35.0							1.45	35	300			

A4. Weight Loss of Annealed and Rolled Cu During Sliding Wear

Sliding speed : 0.20 m/s, Normal load : 1535 g

Sliding Distance (m)	Weight Loss (g)	
	Annealed Cu	Rolled Cu
36	0.0005	0.0011
84	0.0009	0.0021
156	0.0012	0.0032
216	0.0014	0.0041
300	0.0018	0.0048
420	0.0024	0.0060
720	0.0028	0.0078
1440	0.0032	0.0154
2160	0.0045	0.0235
2800	0.0050	0.0285

A5. Dry Sliding Wear Rate of Annealed and Rolled Cu

Sliding speed : 0.20 m/s, Normal load : 1500 g

Sliding Distance (m)	Wear Rate x 10^{-7} (g/m)	
	Annealed Cu	Rolled Cu
36	139	306
84	107	250
156	76.9	205
216	64.8	190
300	60.0	160
420	57.1	143
720	38.9	108
1440	22.2	107
2160	20.8	109
2800	17.8	102

A6. X-ray Diffraction Peaks of Wear Debris from

Rolled Cu against 52100 Steel

Experimental Data			Card Data												
			Cu			CuO			α-Fe$_2$O$_3$			Fe$_2$CuO$_4$		
2θ	d(Å)	I/I$_1$	d(Å)	I/I$_1$	hkl	d(Å)	I/I$_1$	hkl	d(Å)	I/I$_1$	hkl	d(Å)	I/I$_1$	hkl
24.2	3.68	14.3							3.68	25	012			
33.1	2.69	65.7							2.69	100	104			
35.6	2.52	100				2.52	100	1$\bar{1}$1						
40.8	2.21	24.3							2.20	30	113			
43.4	2.09	37.1	2.09	100	111									
48.8	1.87	28.6				1.87	25	2$\bar{0}$2						
54.0	1.69	51.4							1.69	60	116			
57.6	1.60	18.6										1.59	50	511
62.2	1.49	31.4										1.49	100	404
63.8	1.45	35.0							1.45	35	300			

A7. Microhardnesses below the Worn Surface for Rolled Cu at Two Different Sliding Distances, 36 m and 720 m

Depth μm	Knoop Hardness kg/mm²	
	36 m*	720 m*
2.00	180.4	212.4
7.00	157.0	160.0
10.00	128.1	
12.00		142.3
15.00	102.7	
18.00		117.2
20.00	99.7	
22.00		105.8
24.00	100.1	
28.00		98.8
30.00	100.4	
34.00		100.0
36.00	98.6	
38.00		99.1
42.00	99.3	
44.00		101.2
50.00		103.2
54.00		100.1
58.00		102.2
62.00		101.4
68.00		100.6

*: Sliding Distance.

A8. Equivalent Strain below the Worn Surface for

Rolled Cu with 1535 g and 0.2 m/s

Depth μm	Equivalent Strain (ε)						
	ε^1	ε^2	ε^3	ε^4	ε^5	ε^6	ε^7
1.0	5.29	6.80	8.26	8.26	8.26	8.26	8.26
2.0	1.77	3.07	2.50	2.50	2.72	2.72	2.78
3.0	1.00	1.98	1.77	1.89	2.01	1.89	2.01
4.0	0.79	1.49	1.59	1.43	1.59	1.68	1.68
5.0	0.58	1.35	1.30	1.30	1.33	1.43	1.49
6.0	0.48	1.05	1.13	1.08	1.18	1.36	1.38
7.0	0.40	0.84	1.00	0.96	1.08	1.24	1.24
8.0	0.35	0.68	0.92	0.82	0.96	1.13	1.18
9.0	0.31	0.59	0.79	0.66	0.86	1.04	1.10
10.0	0.23	0.50	0.69	0.58	0.79	0.96	0.98
11.0	0.19	0.45	0.58	0.53	0.69	0.89	0.88
12.0	0.16	0.39	0.52	0.48	0.62	0.77	0.78
13.0	0.09	0.34	0.48	0.45	0.55	0.71	0.72
14.0	0.07	0.28	0.42	0.40	0.48	0.62	0.64
15.0	0.03	0.20	0.33	0.36	0.45	0.52	0.53
16.0	0.01	0.15	0.28	0.33	0.42	0.45	0.48
17.0		0.10	0.26	0.31	0.39	0.33	0.35
18.0		0.07	0.23	0.26	0.35	0.28	0.30
19.0		0.03	0.20	0.21	0.27	0.21	0.25
20.0		0.01	0.15	0.18	0.21	0.15	0.18
22.0			0.11	0.13	0.15	0.10	0.13
24.0			0.07	0.10	0.10	0.07	0.09
26.0			0.03	0.05	0.07	0.03	0.04
28.0			0.01	0.03	0.03	0.01	0.01
30.0				0.01	0.01		

Sliding Distance : 1. 36 m, 2. 84 m, 3. 156 m, 4. 216 m, 5. 300 m,

6. 420 m, 7, 720 m.

A9. Dry Sliding Wear Rate of Annealed and Rolled Cu Tested

on 52100 Steel with different Loads and Speeds

Load (g)	Wear Rate x 10^7 (g/m)			
	W_{A1}	W_{A2}	W_{R1}	W_{R2}
310	12.80	13.19	4.81	7.63
500	17.10	17.71	7.48	12.15
954	21.90	20.83	15.00	34.03
1500	22.97	25.69	74.80	102.00
2060	26.18	34.72	100.40	125.00

R : Rolled Cu.   A : Annealed Cu
1 : Test with Sliding Distance, 1782 m; Sliding Speed 0.12 m/s.
2 : Test with Sliding Distance, 2800 m; Sliding Speed 0.20 m/s

68

REFERENCES

1. D.A. Rigney, Sliding Wear of Metals, Ann. Rev. Mater. Sci., 18, 1988, 141-63.

2. C.S. Yust, Tribology and Wear, Int. Met. Rev., 30, 1985, 141-154.

3. L.E. Samuels, The Nature of Mechanically Polished Metal Surfaces: The Surface Deformation Produced by the Abrasion and Polishing of 70 : 30 Brass, J. Inst. Metals, 85, 1956-57, 51-62.

4. R.C.D. Richardson, The Maximum Hardness of Strained Surfaces and The Abrasive Wear of Metals and Alloys, Wear, 10, 1967, 353-82.

5. M.J. Neale, ed., Tribology Hand Book, Butterworths, London, 1973.

6. M.B. Peterson and W.O. Winer, eds., Wear Control Handbook, N.Y., Am. Soc. Mech. Eng., 1980.

7. F.P. Bowden and D. Tabor, The Friction and Lubrication of Solids, Oxford Clarendon Press, 1958.

8. I.V. Kragelskii, Friction and Wear, Butterworths, London, 1965.

9. E. Robinowicz, Friction and Wear of Materials, John Wiley and Sons, N.Y., 1965.

10. N.P. Suh and N. Saka, eds., Fundamentals of Tribology, The MIT Press., 1980.

11. D.A. Reginey, ed., Fundamentals of Friction and Wear of Materials, Metals Park, Ohio, Am. Soc. Met., 1981.

12. D. Scott, ed., Wear, vol. 13, In Treatise Mater. Sci. Tech., ed. H. Herman, N.Y., Academic., 1979.

13. D.H. Buckley, Surface Effects in Adhesion, Friction, Wear and Lubrication, Amsterdam, Elsevier, 1981.

14. M.A. Moore and R.M. Douthwaite, Plastic Deformation below Worn Surface, Met. Trans. A, 7A, 1976, 1833-1839.

15. N.P. Suh, An Overview of the Delamination Theory of Wear, Wear, 44, 1977, 1-16.

16. D.A. Rigney and J.P. Hirth, Plastic Deformation and Sliding Friction of Metals, Wear, 53, 1979, 345-70

17. P.A. Jacquet, Micrographic Study of Plastic Deformation of α-Brass; Application to the Surface Structure caused by Abrasion, Rev. Met., 47, 1950, 355-64.

18. J. Halling, Principles of Tribology, The Macmillan Press Ltd., 1975.

19. K.Z. Gahr, Microstructure and Wear of Materials, Elsevier, 1987.

20. K.L. Johnson, Contact Mechanics, Cambridge University Press, 1987.

21. G.M. Hamilton and L.E. Goodman, The Stress Field Created by a Circular Sliding Contact, J. Appl. Mech., June 1966, 371-76.

22. G.E. Dieter, Mechanical Metallurgy, McGraw-Hill, 1986.

23. P. Heilmann, J. Don, T.C. Sun and D.A. Rigeny, Sliding Wear and Transfer, Wear, 91, 1983, 171-90.

24. D.A. Rigney, L.H. Chen and M.G.S. Naylor, Wear Processes in Sliding Systems, Wear, 100, 1984, 195-219.

25. L.H. Chen and D.A. Rigney, Transfer during Unlubricated Sliding Wear, in Wear of Materials 1985, ASME, 1985.

26. J.G. Sevillano, P.V. Houtte, E.Aernoudt, Large Strain Work Hardening and Texture,

Prog. Mater. Sci., 25, 1980, 69-412.

27. G. Langford and M. Cohen, Strain Hardening of Iron by Severe Plastic Deformation, Trans. ASM, 62, 1969a, 623-638.

28. J.H. Hollomon, Tensile Deformation, Trans. AIME, 162, 1945, 268-275.

29. E. Voce, The Relationship Between Stress and Strain For Homogeneous Deformation, J.Inst.Met., 74, 1948, 537.

30. J.D. Embury and R.M. Fisher, The Structure and Properties of Drawn Pearlite, Acta Metall., 14, 1966, 147-159.

31. A.S. Malin and M. Hatherly, Microstructure of Cold-rolled Copper, Met. Sci., 13, 1979, 463-72.

32. J.E. Bailey and P.B. Hirsch, Electron Microscope Observations on the Annealing Processes Occuring in Cold-worked Silver, Philos. Mag., 5, 1960, 833-842.

33. J.D. Embury, A.S. Keh and R.M. Fisher, Substructural Strengthening in Materials Subject to Large Plastic Strains, Trans. AIME, 236, 1966, 1252-1260.

34. A. Korbel, J.D. Embury, M. Hatherly, P.L. Martin and H.W. Erbsloh, Microstructural Aspects of Strain Localization in Al-Mg Alloys, Acta Metall., 34, 1986, 1999-2009.

35. P. Heilman, Orientation Determination of Subsurface Cells generated by Sliding, Acta Metall., 31, 1983, 1293-1305.

36. D. Kuhlmann-Wilsdorf, Dislocation Concepts in Friction and Wear, in Fundamentals of Friction and Wear of Materials, ed. D.A. Rigney, ASM, 1981.

37. P.J. Jackson, Dislocation Modelling of Shear in f.c.c. crystals, Prog. Mater. Sci., 29,

1985, 139-75.

38. D. Teirlinck, F. Zok, J.D. Embury and M.F. Ashby, Fracture Mechanism Maps in Stress Space, Acta Metall., 36, 1988, 1213-1228.

39. G. Le Roy, J.D. Embury, G. Edward and M.F. Ashby, A Model of Ductile Fracture Based on the Nucleation and Growth of Voids, Acta Metall., 29, 1981, 1509-1522

40. N. Ohmae, T.Tsukizoe and F. Akiyama, On the Microscopic Processes Involved in Metallic Friction, Phli. Mag. A., 40, 1979, 803-10.

41. D.A. Rigney, The Significanceof Near Surface Microstructure in the Wear Process, Wear, 46, 1978, 241-250.

42. A.T. Alpas and J.D. Embury, The Role of Subsurface Deformation and Strain Localization on the Sliding Wear Behavior of Laminated Composites, in Press.

43. J.J. Wert and G.A. Sloan, The Influence of Stacking Fault Energy and Adhesion on the Wear of Cu and Al-Bronze, in Wear of Materials 1987, ASME, 1987.

44. M.A. Seif, P.J. Mohr, F.A. Moslehy and S.L. Rice, Deformation Measurement in Sliding Wear by Laser Speckle Metrology, in Wear of Materials 1989, ASME, 1989.

45. M.A. Moore, R.C.D. Richardson and D.G. Attwood, The Limiting Strength of Worn Metal Surfaces, Met. Trans. 3, 1976, 2485-91.

46. J.. Kirk and T.D. Swanson, Subsurface Effects during Sliding Wear, Wear, 35, 1975, 63-67.

47. S.L. Rice, H. Nowotny and S.F. Wayne, Characteristics of Metallic Subsurface Zones in Sliding and Impact Wear, in Wear of Materials 1981, ASME, 1981.

48. O. Vingsbo and S. Hogmark, Wear of Steels, in Fundamentals of Friction and Wear

of Materials, ed. D.A. Rigney, Metals Park, Am. Soc. Met., 1981.

49. P.J. Plau, Use of a Two-diagonal Measurement Method for Reducing Scatter in Knoop Microhardness Testing, Script Metall., 14, 1980, 719-722.

50. P.J. Blau, Investigation of the Nature of Micro-indentation Hardness Gradients below Sliding Contacts in Five Copper Alloys Worn against 52100 Steel, J. Mater. Sci., 19, 1984, 1957-1968.

51. J.H. Dautzenberg and J.H. Zaat, Quantitative Determination of Deformation by Sliding Wear, Wear, 23, 1973, 9-19.

52. P. Heilman and D.A. Rigney, An Energy-based Model of Friction and its Application to Coated Systems, Wear, 72, 1981, 195-217.

53. A.W. Ruff, Deformation Studies at Sliding Wear Tracks in Iron, Wear, 40, 1976, 59-74.

54. S.H. Goods and L.M. Brown, The Nucleation of Cavities by Plastic Deformation, Acta Metall., 27, 1976, 1-15.

55. J.R. Rice and D.M. Tracey, On the Ductile Enlargement of Voids in Triaxial Stress Fields, J. Mech. Phys. Solids, 17, 1969, 201-217.

56. A. Nstoh, The Formation of Cracks in Plastic Flow II, Proc. Roy. Soc. (London), A232, 1955, 548-560.

57. F.A. McClintock, Ductility, ASM, Metals Park, Ohio, 1968.

58. S. Jahanmir and N.P. Suh, Mechanics of Subsurface Void Nucleation in Delamination Wear, Wear, 44, 1977, 17-38.

59. K.E. Puttick, Ductile Fracture in Metals, Phil. Mag., 4, 1959, 964.

60. L.M. Brown and J.D. Embury, Proc. 3rd Int. Conf. on Strength of Metals and Alloys, Inst. of Metal, London, 1973.

61. D. Teirlinck, F. Zok, J.D. Embury and M.F. Ashby, Fracture Mechanism Maps in Stress Space, Acta Metall., 36, 1988, 1213-1228.

62. D.A. Rigney, L.H. Chen and M.G.S. Naylor, Wear Process in Sliding System, Wear, 100, 1984, 195-219.

63. C. Zener, Fracturing of Metals, ASM, Novelty, Ohio, 1949.

64. L.M. Brown and W.M. Stobbs, The Work-hardening of copper-silica V. Equilibrium Plastic Relaxation by Secondary Dislocations, Phil. Mag., 34, 1976, 351-372.

65. N.P. Suh, The Delamination Theory of Wear, Wear, 25, 1973, 111-124.

66. L.E. Samuels, E.D. Doyle and D.M. Turley, Sliding Wear Mechanisms, in Fundamentals of Friction and Wear of Materials, ed. D.A. Rigney, Metals Park, Ohio, Am. Soc. Met., 1981.

67. A.W. Ruff and L.K. Ives, Characterization of Wear Surfaces and Wear Debris, in Fundamentals of Friction and Wear of Materials, ed. D.A. Rigney, Metals Park, Ohio, Am. Soc. Met., 1981.

68. J. Don and D.A. Rigney, Prediction of Debris Flake Thickness, in Wear of Materials 1985, ASME, 1985.

69. J. Shirohara, K. Hiratuska and T. Sasada, The Effect of-f-orbital Electron Vancancy on Friction and Wear of Materials, in Wear of Materials 1987, ASME, 1987.

70. S. Jahanmir, The Relationship of Tangential Stress to Wear Particle Formation Mechanisms, in Wear of Materials 1985, ASME, 1985.

74

71. L.H. Chen and D.A. Rigney, Transfer during Unlubricated Sliding Wear of Selected Metal System, in Wear of Materials 1985, ASME, 1985.

72. E. Rabinowicz, The Shape of Adhesive Wear Particles, in Wear of Materials 1985, ASME, 1985.

73. Z.Y. Yang, M.G.S. Naylor and D.A. Rigney, Sliding Wear of 304 and 310 Stainless Steels, in Wear of Materials 1985, ASME, 1985.

74. M. Sawa and D.A. Rigney, Sliding Behavior of Dual Phase Steels in Vaccum and in Air, in Wear of Materials 1987, ASME, 1987.

75. T. Kayaba and K. Kato, The Analysis of Adhesive Wear Mechanisms by Successive Observations of the Wear Process in SEM, in Wear of Materials 1979, ASME, 1979.

76. E.D. Doyle, A Mechanism of Spherical Particle Formation in Wear Debris, J. Aust. Inst. Metals, 19, 1974, 276-278.

77. N.K. Myshkin, O.V. Kholoolilov and V.A. Bely, A Study on Surface Topography and Wear Particles, in Wear of Materials 1989, ASME, 1989.

78. T.F.J. Quinn, Review of Oxidational Wear, Part I: The Origins of Oxidational Wear, Tri. Int., 16, 1983, 257-71.

79. T.F.J. Quinn, Review of Oxidational Wear, Part II: Recent Developments and Future Trends in Oxidational Wear Research, Tri. Int., 16, 1983, 305-15.

80. M.M. Khruschov, Resistance of Metals to Wear By Abrasion as Related to Hardness, in Proc. Conf. Lubrication Wear, London, 1957.

81. J. Larsen-Badse, The Abrasion Resistance of Some Hardened and Tempered Carbon

Steels, Trans. TMS-AIME, 236, 1966, 1461-66.

82. R.C.D. Richardson, The Wear of Metals by Hard Abrasive Wear, Wear, 10, 1967, 291-309.

83. H.S. Avery, Work Hardening in Relation to Abrasion Resistance in Materials for the Mining Industry Symposium, Climax Molybdenum Co., 1974.

84. T.M. Ahn, P.J. Blau, K.L. Hsu, D.A. Rigney and J.D. Schell, Metallography Techniques for Wear Specimen, Wear, 56, 409-13, (1979).

85. D.M. Marsh, Plastic Flow in Glass, Proc. Roy. Soc., Ser. A, 279, 1964, 420-435.

86. P.W. Bridgman, Studies in Large Plastic Flow and Fracture, McGraw-Hill, 1952.

Table 3.1. Material Characteristics

Materials	Condition	KHN (kg/mm^2)
Commercial pure copper (99.9%)	Annealed	71.0
	50% Cold Rolled	100.5

Table 3.2. Compositions of Etchant for Copper

Ferric Chloride (FeCl$_3$)	Hydrochloric Acid (HCl, 38%)	Distilled Water
5 gm	50 ml	100 ml

Table 5.1. Best Fit Parameters for the Voce Equation

$$\sigma = \sigma_s - (\sigma_s - \sigma_o) \exp (\varepsilon/\varepsilon_c)$$

	S.D.* (m)	σ_o (MPa)	$\sigma_{s\ (MPa)}$	ε_c
Annealed Cu	36	235.2	521.0	0.84
	720	190.7	668.0	1.43
Rolled Cu	36	309.5	591.0	0.96
	720	318.3	671.0	1.46

*: Sliding Distance.

Table 5.2. Best Fit Parameters for the Power Equation

$$\sigma = K \, (\, \varepsilon \,)^n$$

	S.D.* (m)	K (MPa)	n
Annealed Cu	36	384.5	0.178
	720	455.0	0.188
Rolled Cu	36	474.6	0.101
	720	502.2	0.129

*: Sliding Distance (m)

Table 5.3. Constants For Equation 5.16

	Annealed Cu		Rolled Cu	
	36 m*	720 m*	36 m*	720 m*
D	3.028	3.532	3.883	5.439
B	-0.589	-0.250	-0.511	-0.278
E	732.17	1028.90	768.70	771.08
A	-0.336	-0.339	-0.150	-0.117

* : Sliding Distance.

Table 5.4. The Critical Depth, Z^* (μm), as a Function of C

Annealed Cu				Rolled Cu			
36 m[*]		720 m[*]		36 m[*]		720 m[*]	
Z^*	C	Z^*	C	Z^*	C	Z^*	C
6.7	127877	16.0	746343	6.4	149786	11.5	465356
7.1	128260	16.4	746867	7.0	151019	11.9	464999
7.3	129042	16.8	749176	7.4	154392	12.3	467309
5.9	135441	15.2	752155	5.8	157237	11.1	469209
5.7	140648	14.4	771003	5.4	173287	10.9	472817

: Sliding Distance.

Table 5.5. The Parameters For Calculation of Area of Deformed Layer on Cross Section

	Annealed Cu	Rolled Cu
R_1 (mm)	19.0	19.0
R_2 (mm)	19.050	19.028
θ	8.8°	13.5°
w (mm)	3.0	4.5
t (μm)	50	28
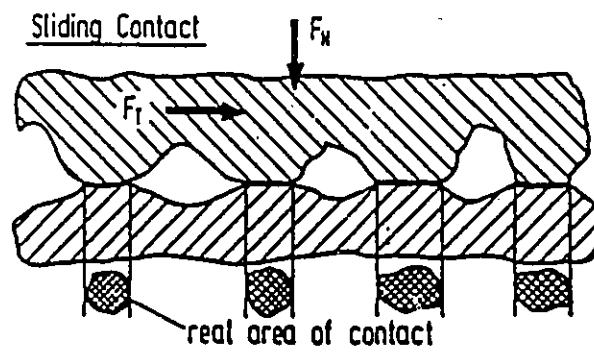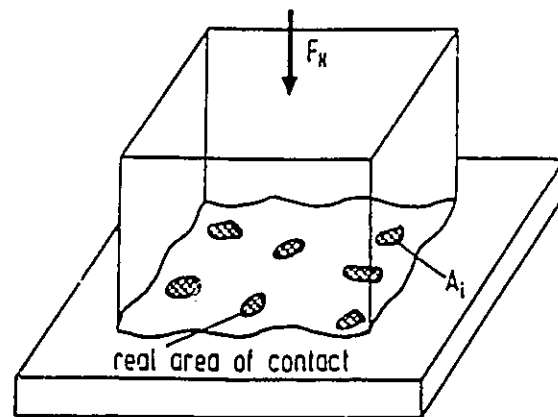
Fig. 2.1: Real area of contact under (a) normal load, (b) both normal and tangential load. (After K.Z. Gahr[19]).
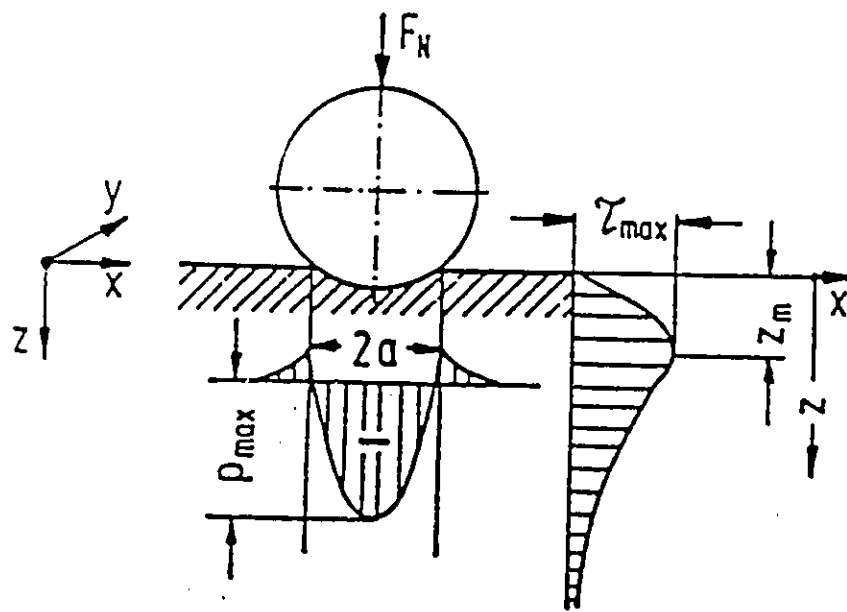
Fig. 2.2: Schematic stress distribution for the hertian contact. (After K.Z. Gahr[19]).
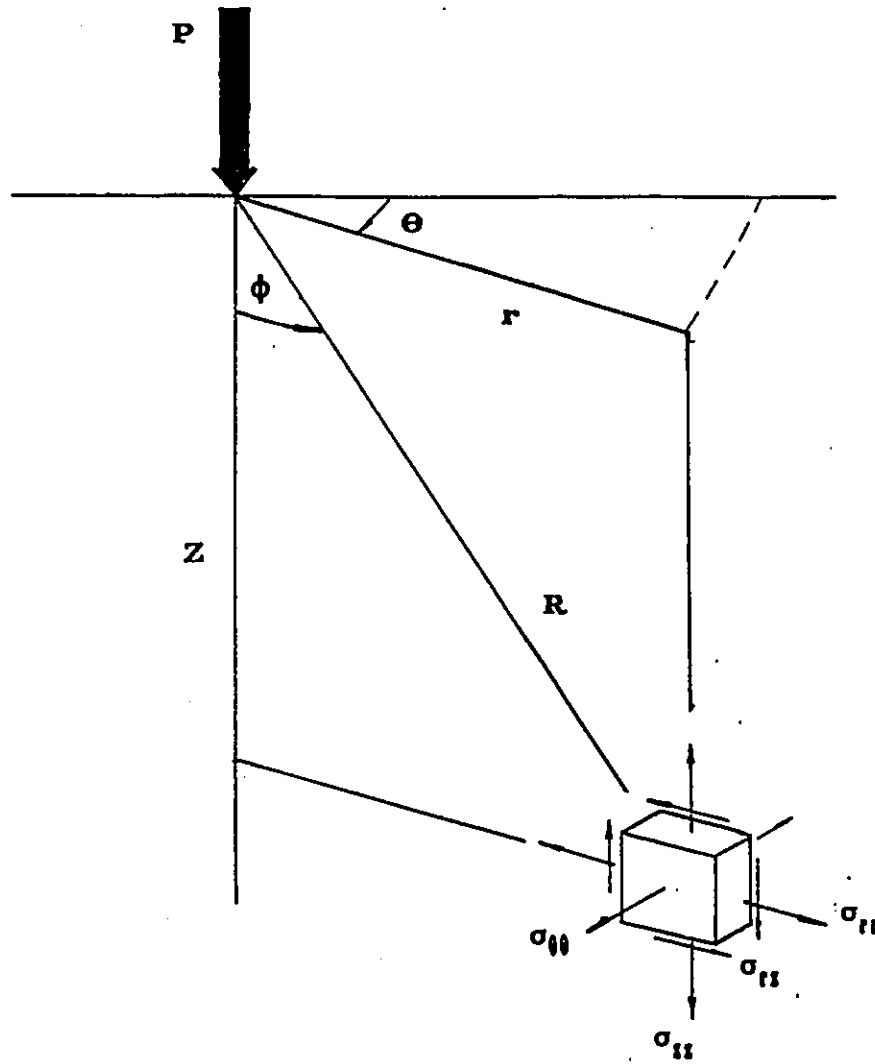
Fig. 2.3: The stress components for the elastic analysis of point loading in coordinate system. (After G.M. Hamilton and L.E. Goodman[21]).
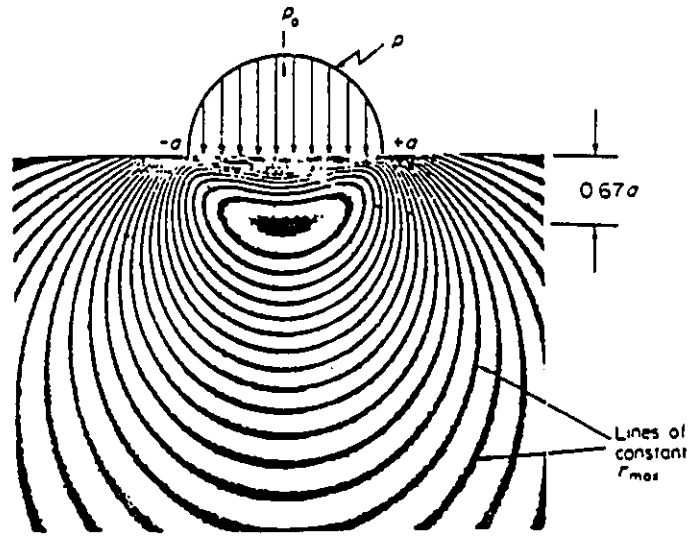
(a)
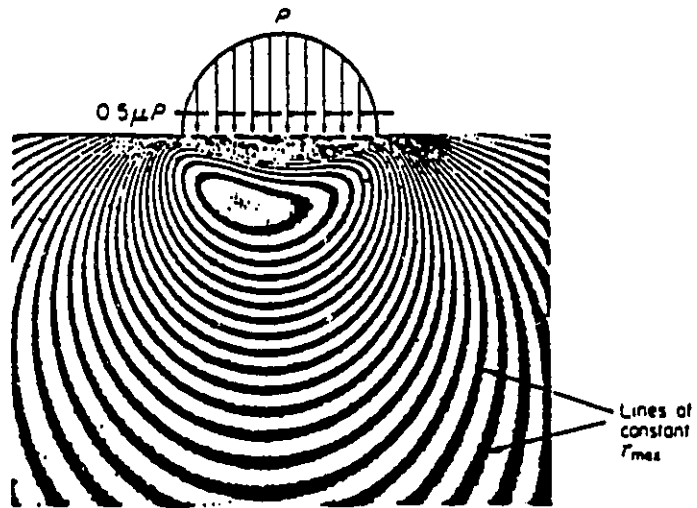
(b)

Fig. 2.4: Actual isochromatics obtained for the circular contact due to (a) normal load, (b) both normal and tangential load. (After J. Halling[18]).
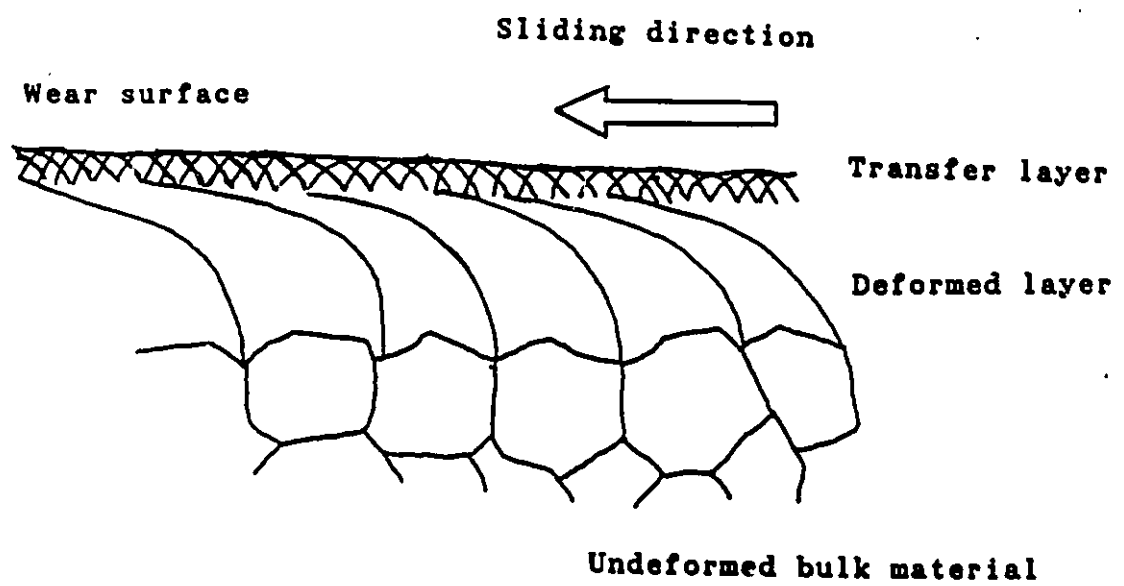
Fig. 2.5: Three-layer microstructure found at and below the worn surface.

Worn surface

Section

(a)

Worn surface
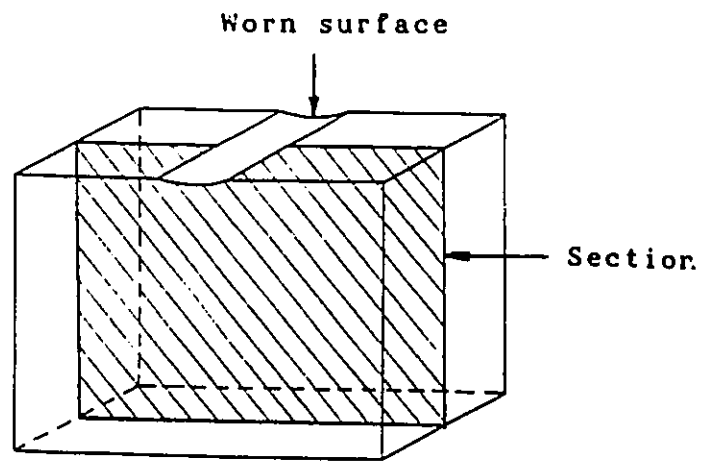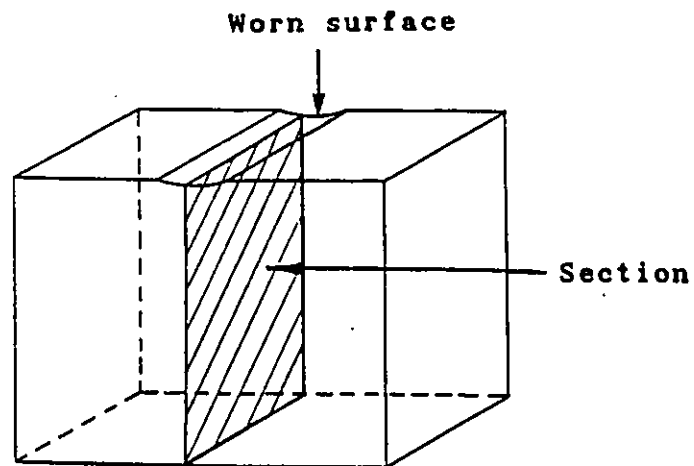
Section

(b)

Fig. 2.6: (a) Longitudinal and (b) transverse sections prepared for metallographic

examination
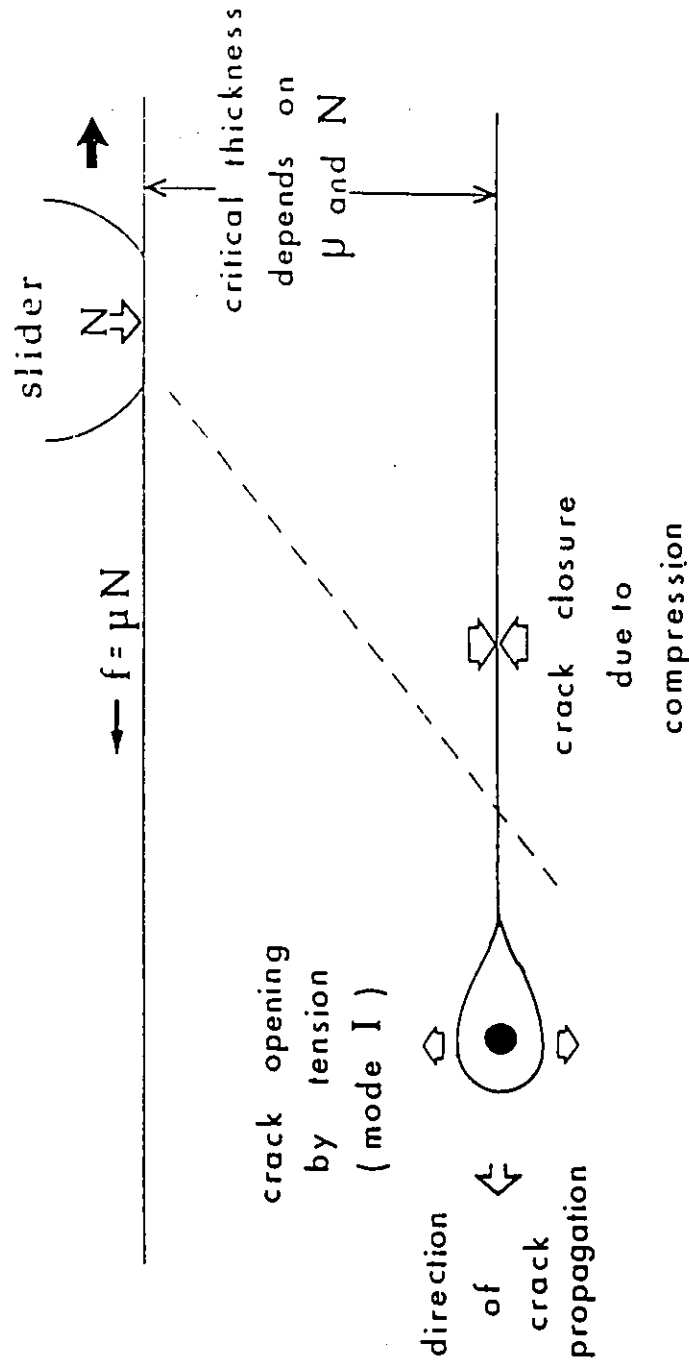
Fig.2.7: Suh's model on delamination wear occurs by void nucleation by decohesion at an inclusion/matrix interface, then subsequently propagation in the tensile zone.

(After N.P. Suh[15]).
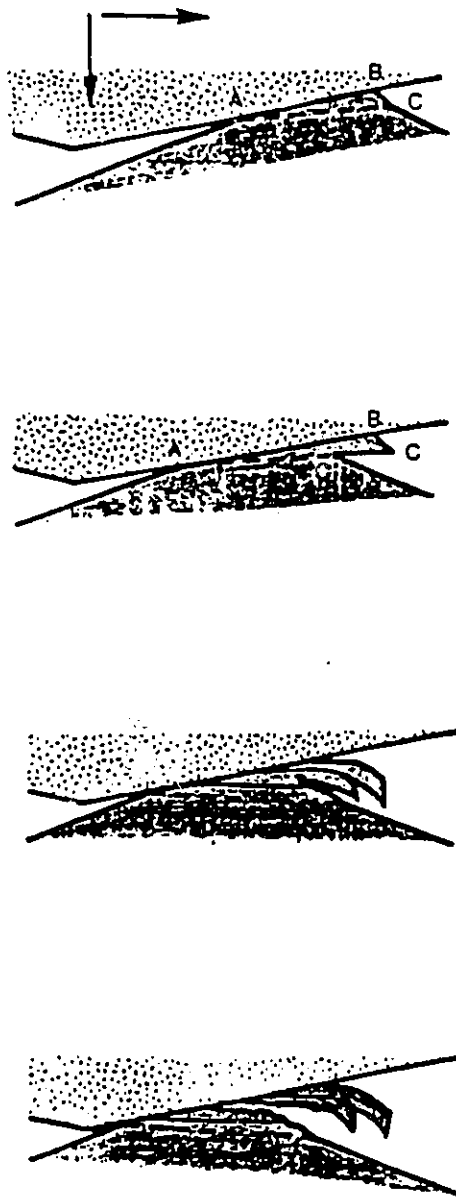
Fig. 2.8: Schematic illustration of the several stages involoved in formation of flake-shape debris by slip-tongue mechanism. (After T. Kayaba and K. Kato[75]).
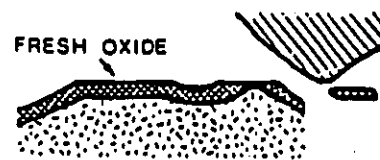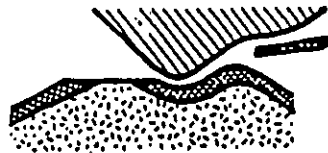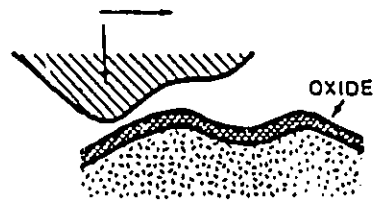
Fig. 2.9: The sequence of oxide debris formation presented by Quinn[78].
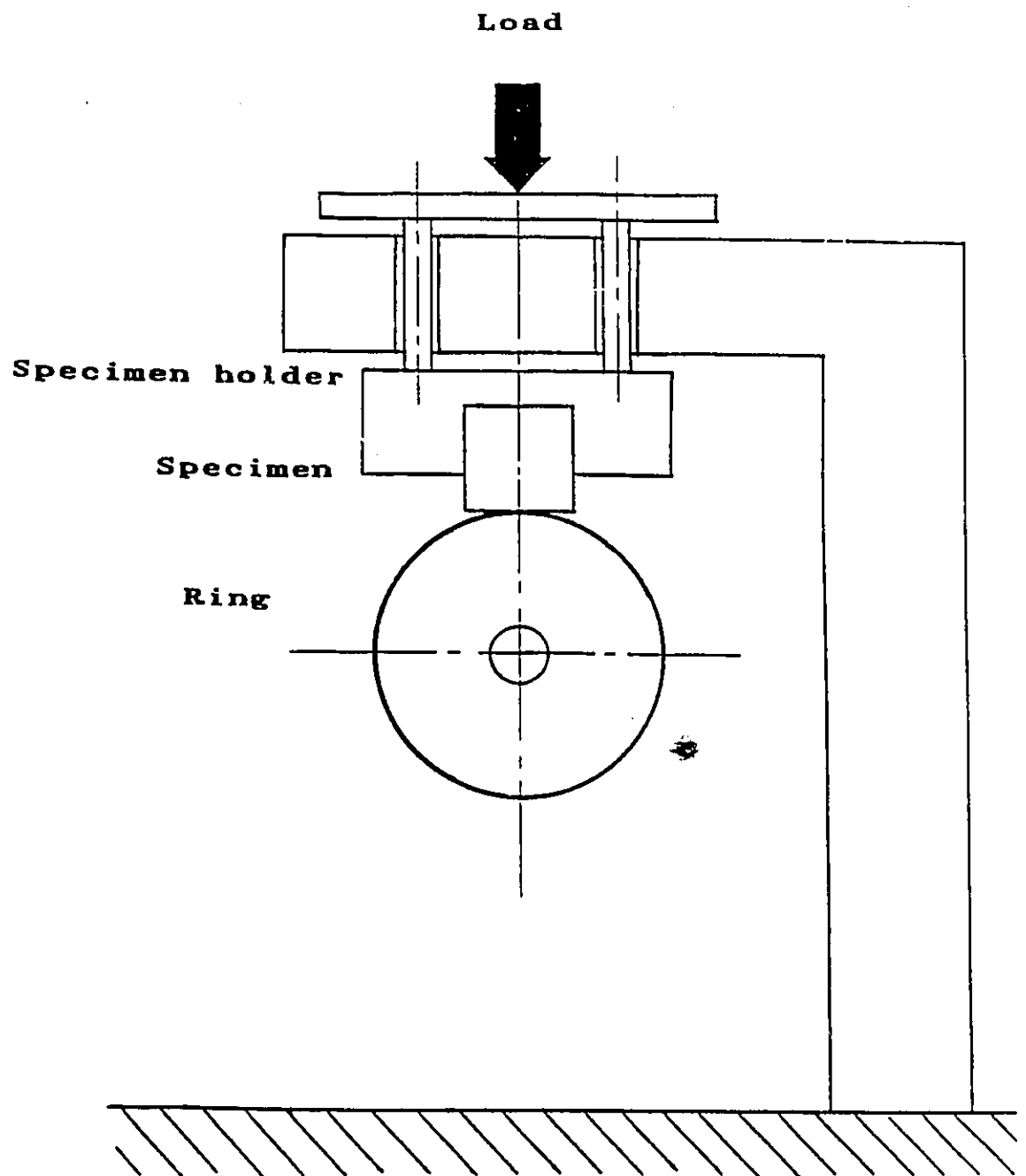
Fig. 3.1: Block on ring type wear setup.

Wear track

Taper section

(a)

$$Z = D \sin\alpha$$
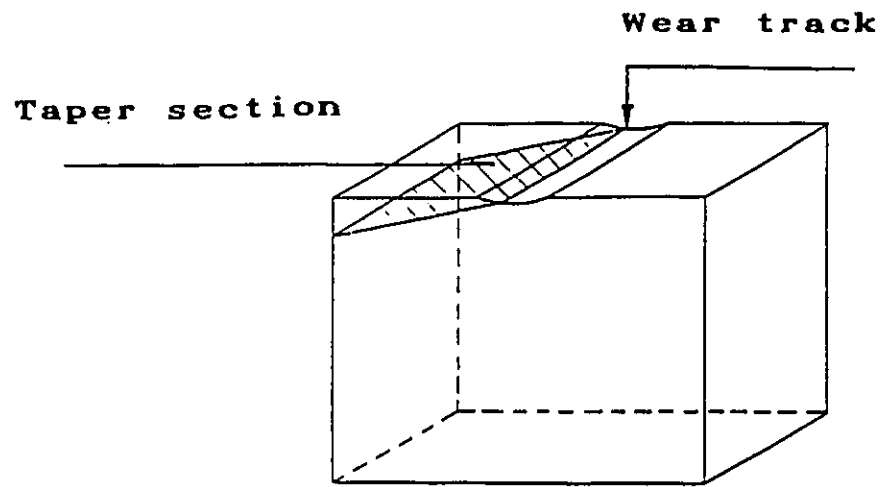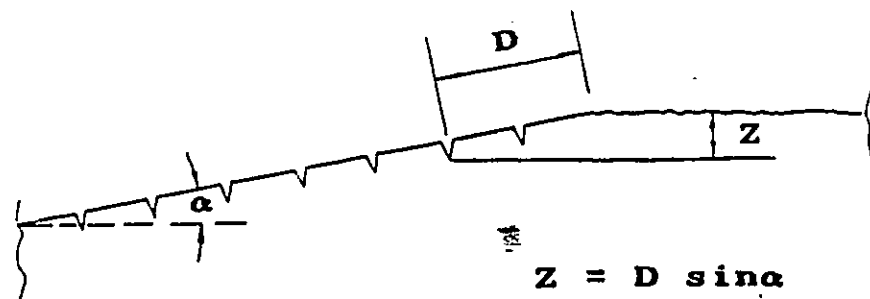
(b)

Fig. 3.2: (a) Schematic of taper section of worn specimen.

(b) An enlarged taper section to illustrate the calculation of depth corresponding
to microindenter.

94

(a)

(b)
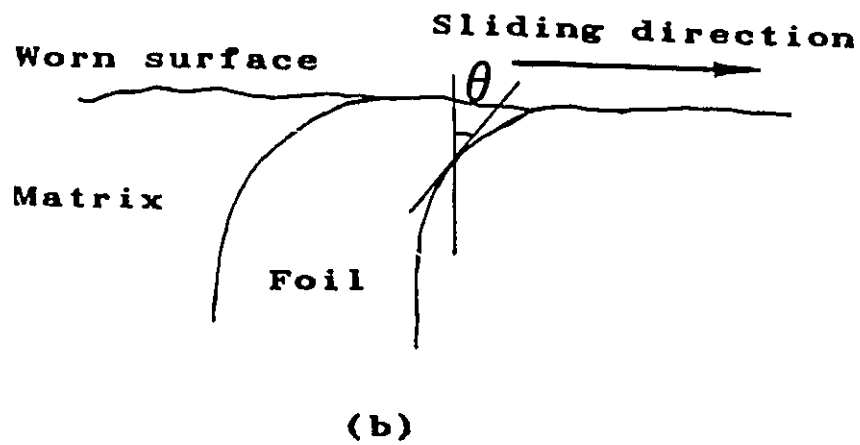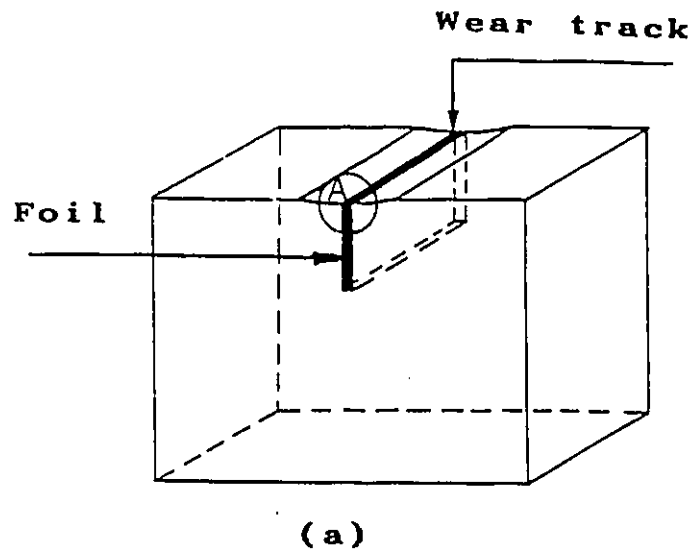
Fig. 3.3: Schematic diagram showing the foil-slit method for measuring the strain

gradients below the worn surface.

(a) worn specimen with inserted foil.

(b) an enlarged schematic of area A in (a) to show curved interface.
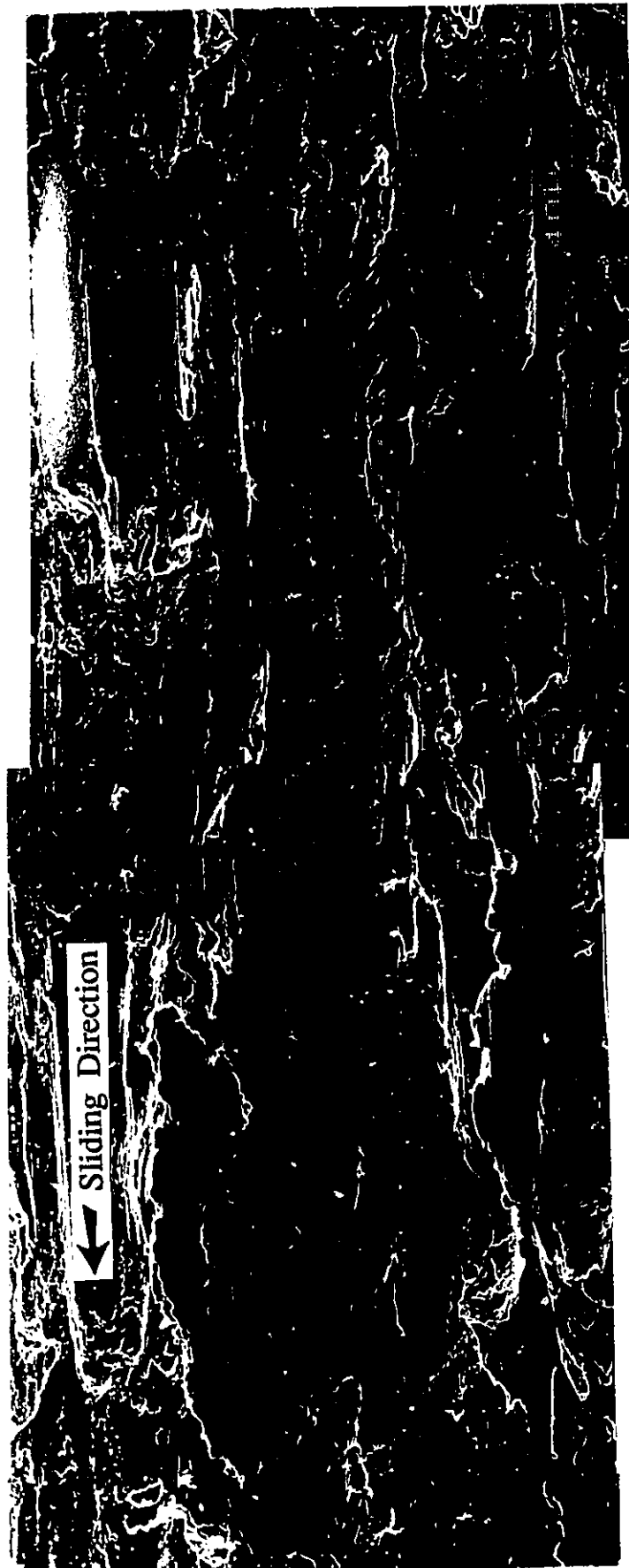
Fig. 4.1: The wear surface topography.
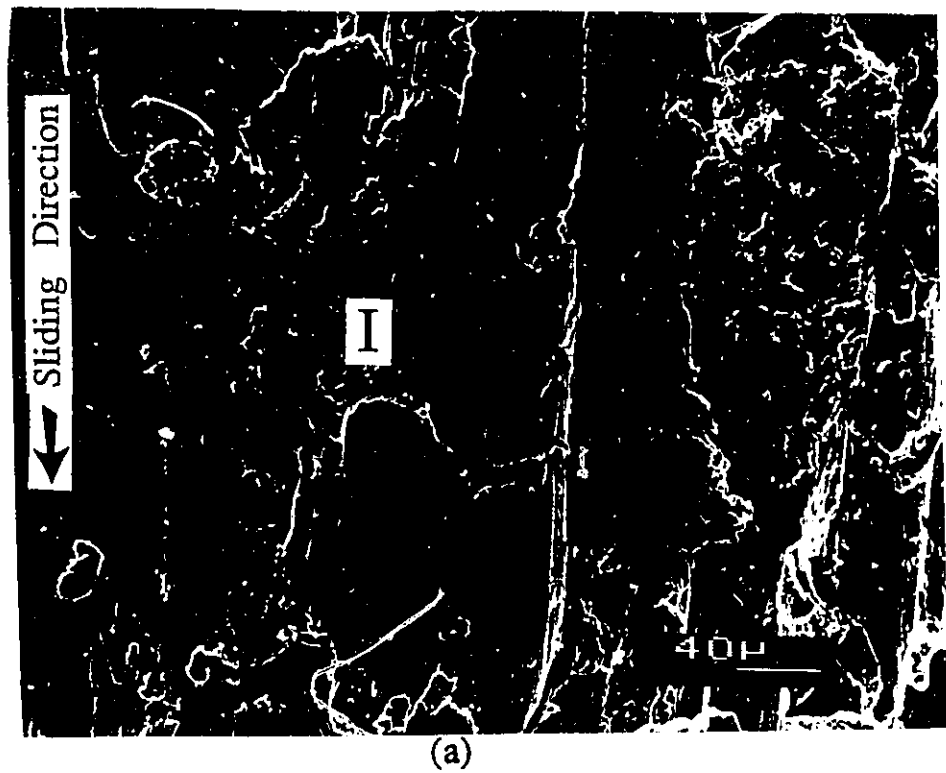
Fig. 4.2: (a) Crack perpendicular to the sliding direction on the wear surface in the

beginning region.

(b) The enlarged area I in (a).
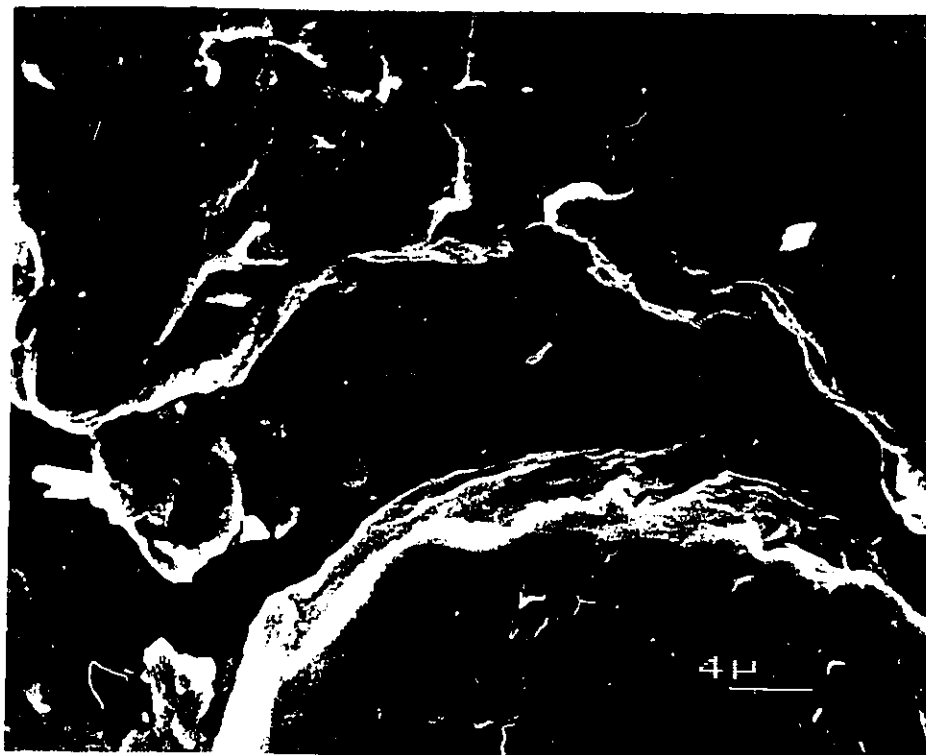
(b)

Fig. 4.2 (continued) (b)
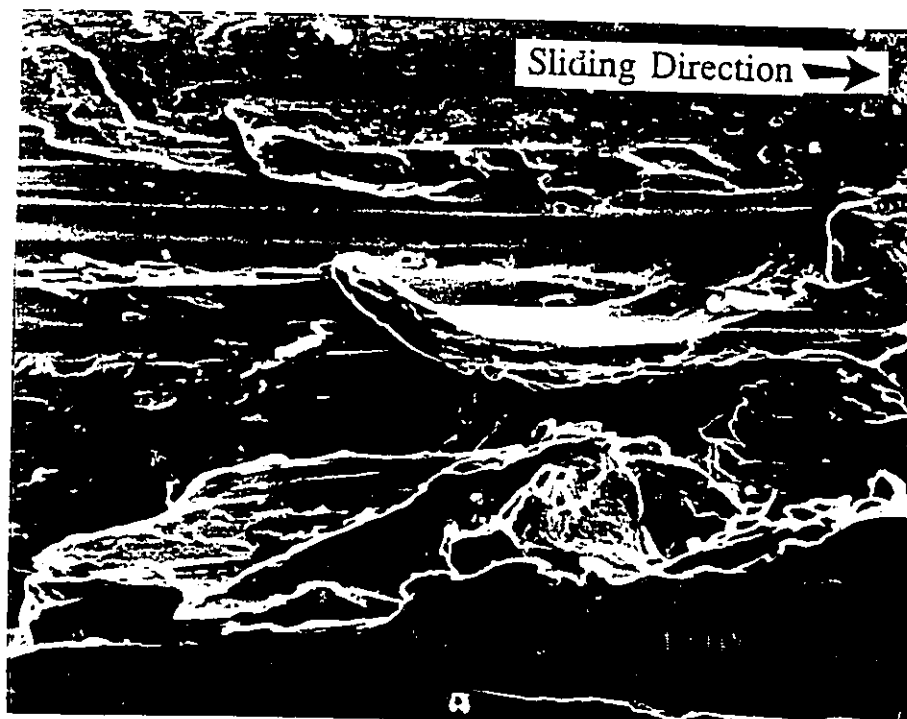
Fig. 4.3: The delaminated flake lifted off the worn surface.
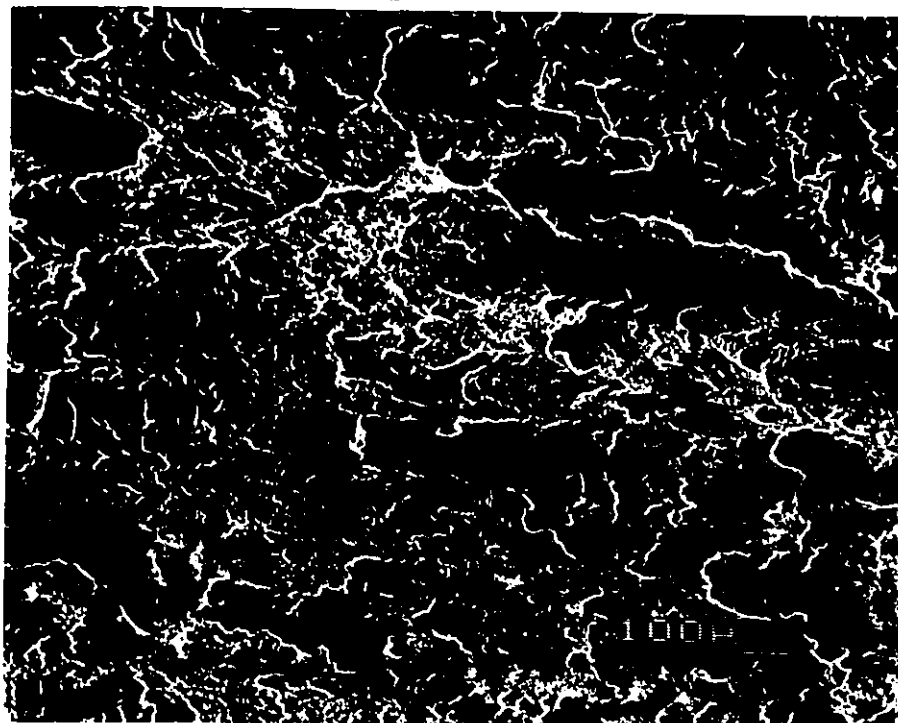
Fig. 4.4: Oxide formation on the worn surface.

Fig. 4.5: Longitudinal section shows that a shallow deformed layer below the wear surface at the beginning of wear process (sliding distance = 36 m).

Sliding Direction →

1

4

5

2

3

10μ

102

Fig. 4.6: (a) With the increase of sliding distance, the thickness of deformed layer

increases. Cracks were propagated parallel to sliding direction at several locations,

1, 2, 3. The flake-shape debris lifted off from the wear surface at locations, 4,5

(sliding distance = 216 m). (b) The subsurface crack propagates in the sliding

direction at a high magnification.
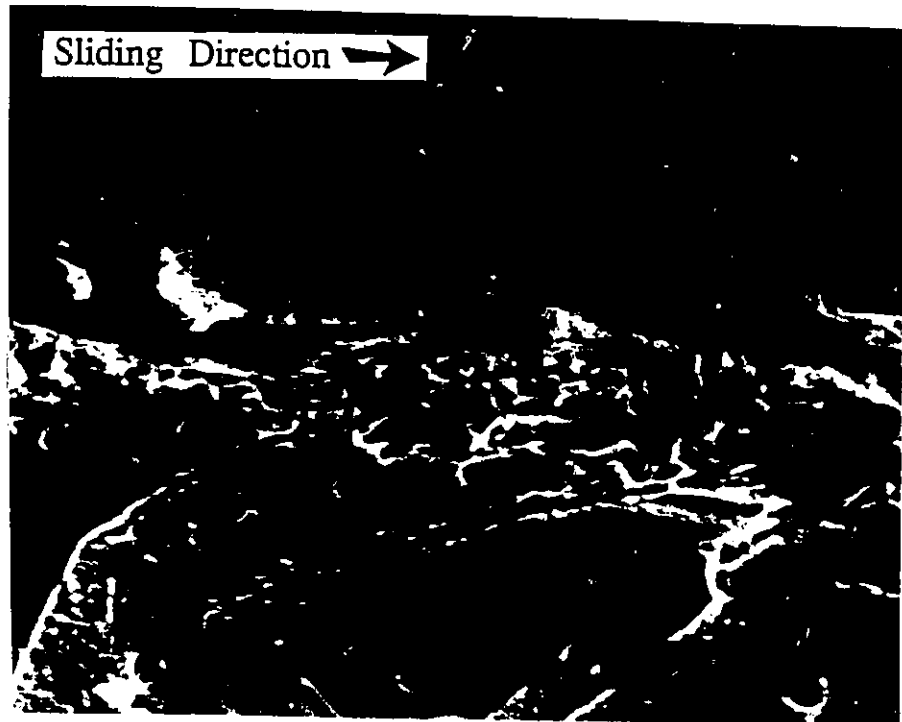
Sliding Direction ➥

(b)

Fig. 4.6 (continued) (b)

103
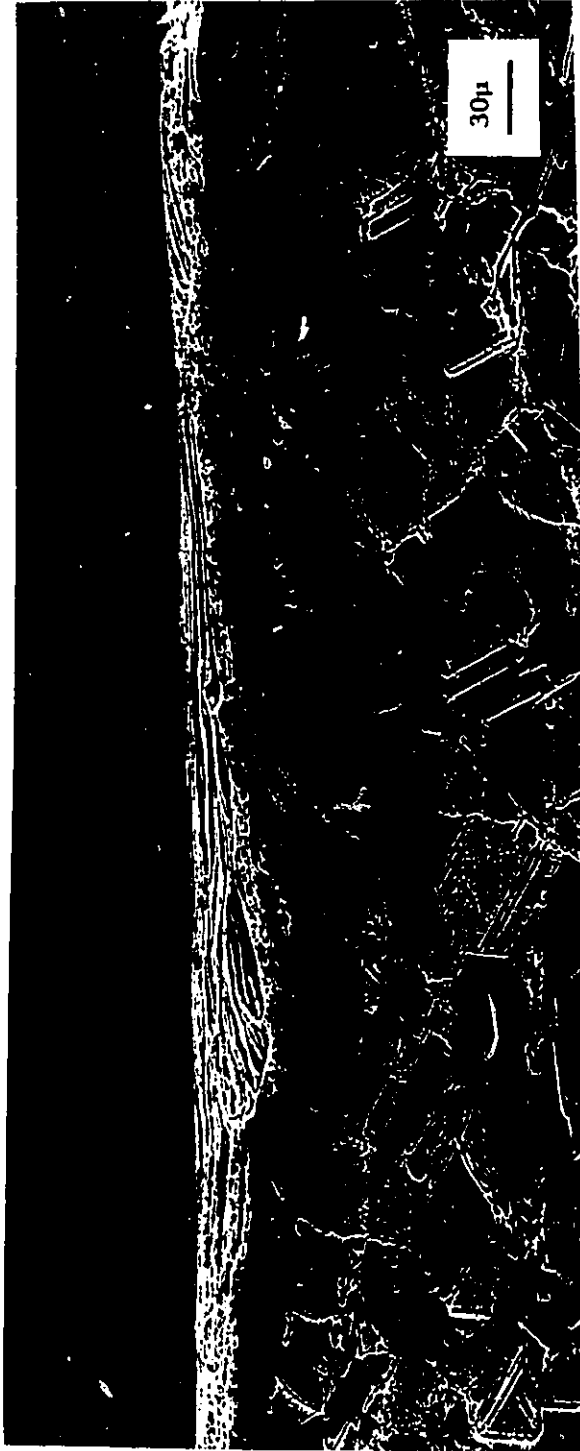
Fig. 4.7: The thickness of deformed layer reaches a constant value of 50 μm

(sliding distance = 720 m).

104

Fig. 4.8: The elliptical grains below the wear surface on transverse section.

Worn Surface

2μ

(a)
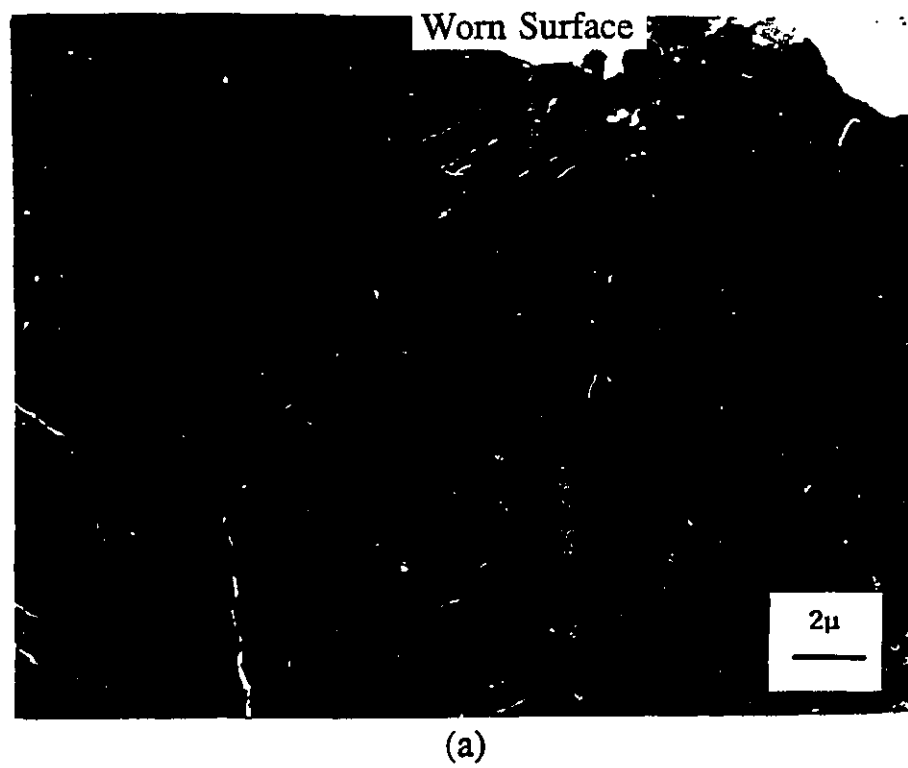
Fig. 4.9: The shear bands.

Fig. 4.10: SEM micrograph of microindentations on a taper section in annealed Cu.
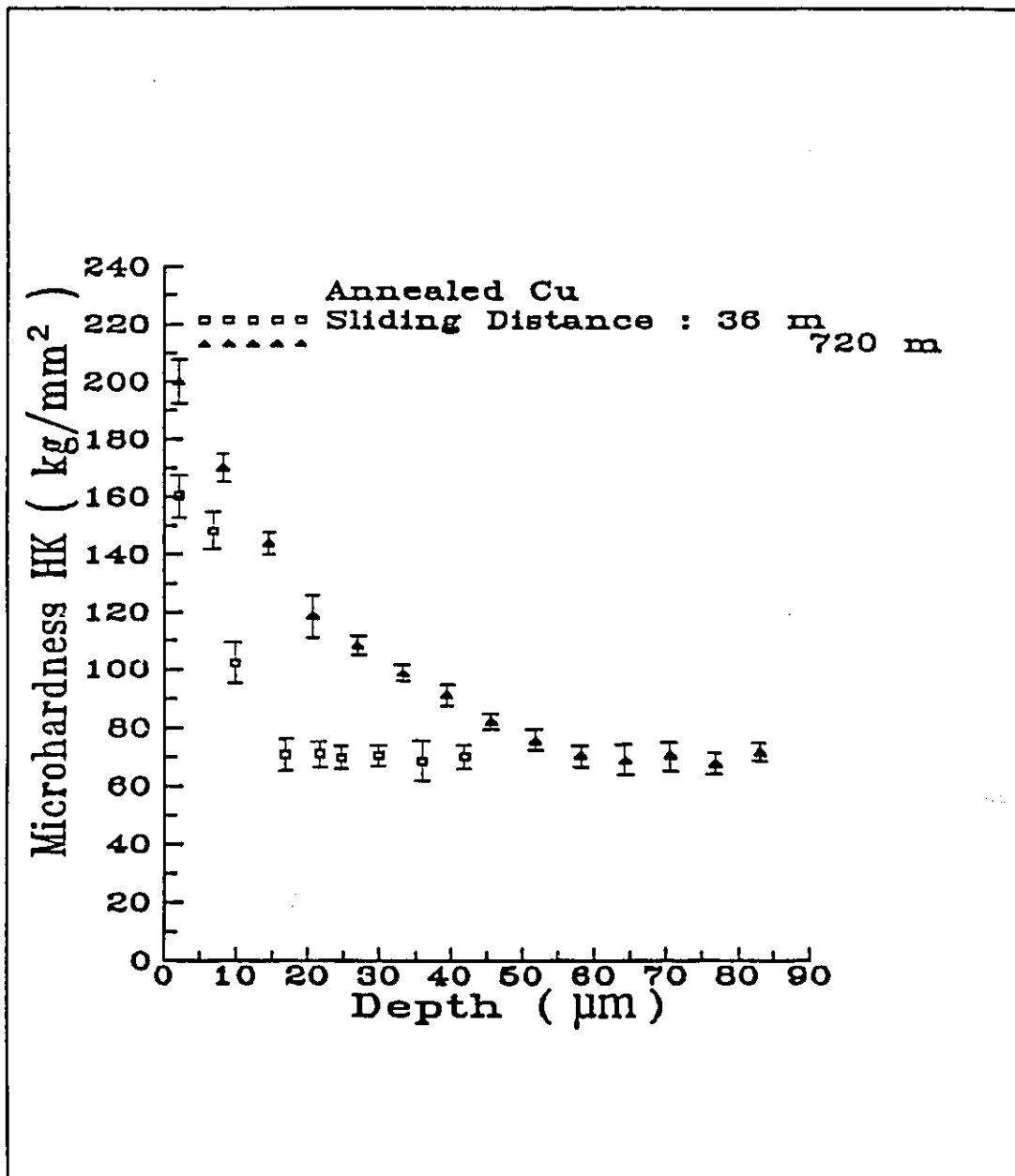
Fig. 4.11: Microhardness (HK) gradient distributions below the worn surface at two

different sliding distances for annealed Cu.
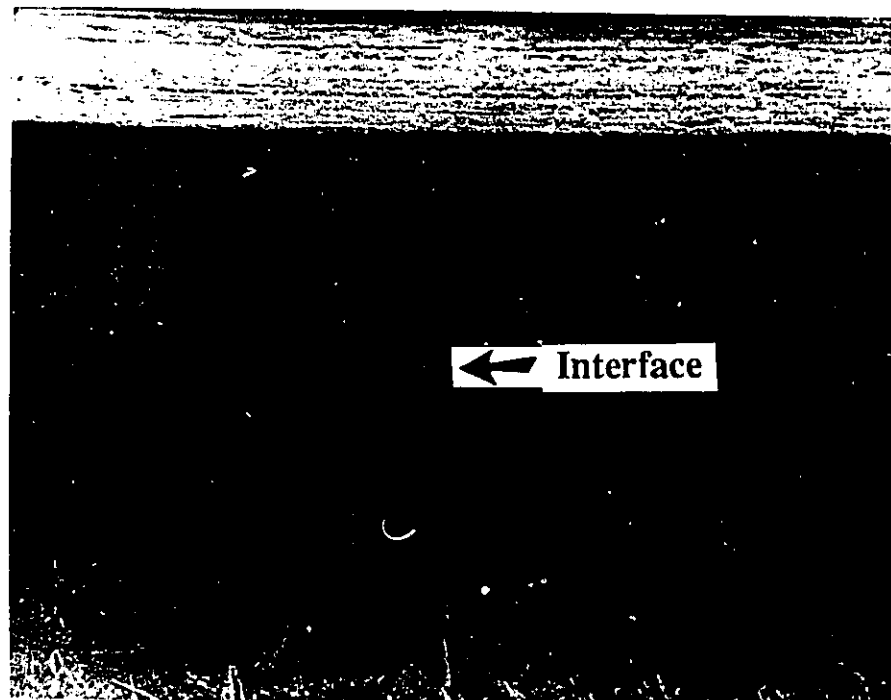
(a)

Fig. 4.12: The artifical interface made by inserting a foil.

(a) straight interface before wear test,

(b) curved interface after sliding distance of 420 m.
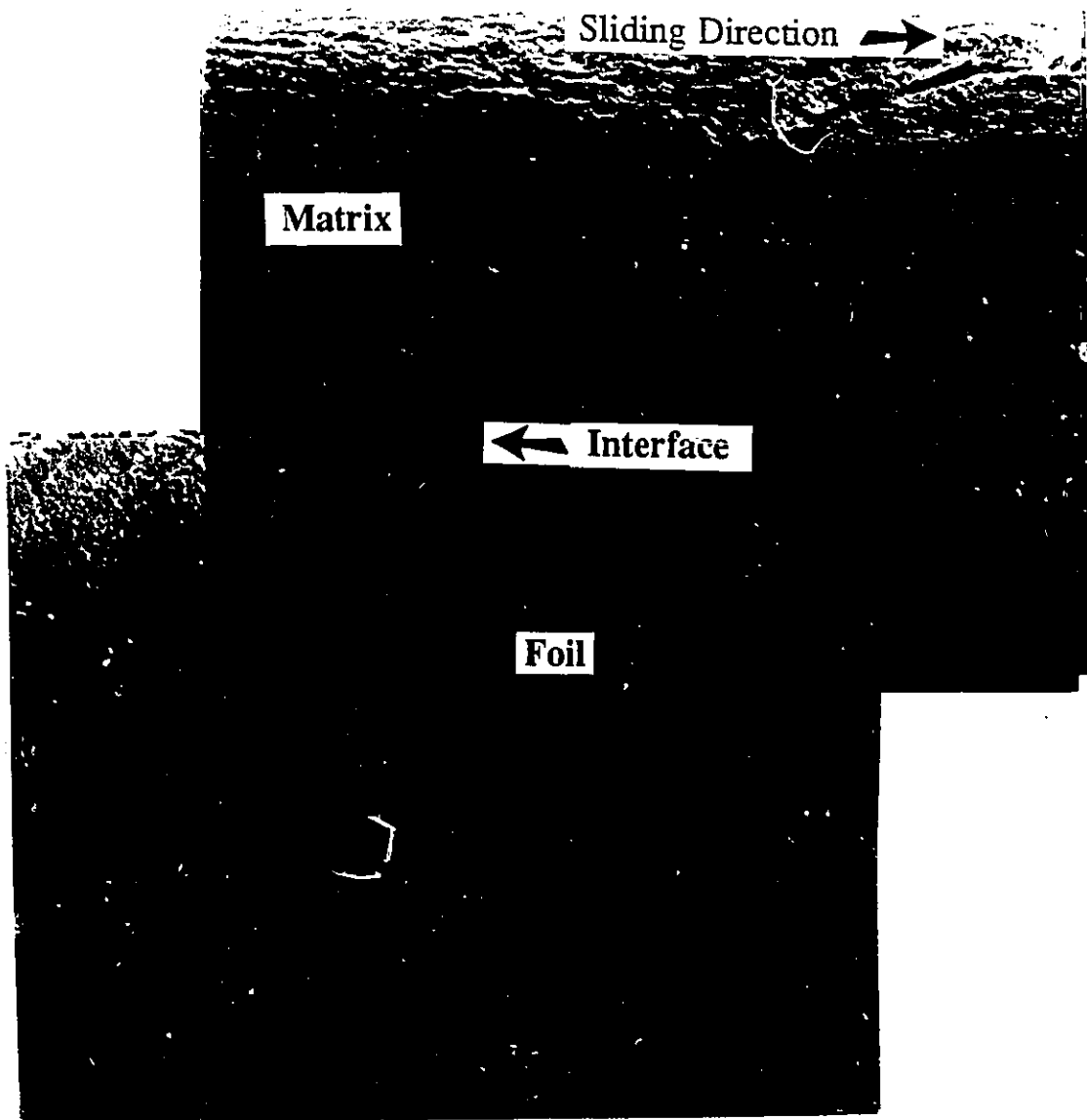
Fig.4.12 (continued) (b)
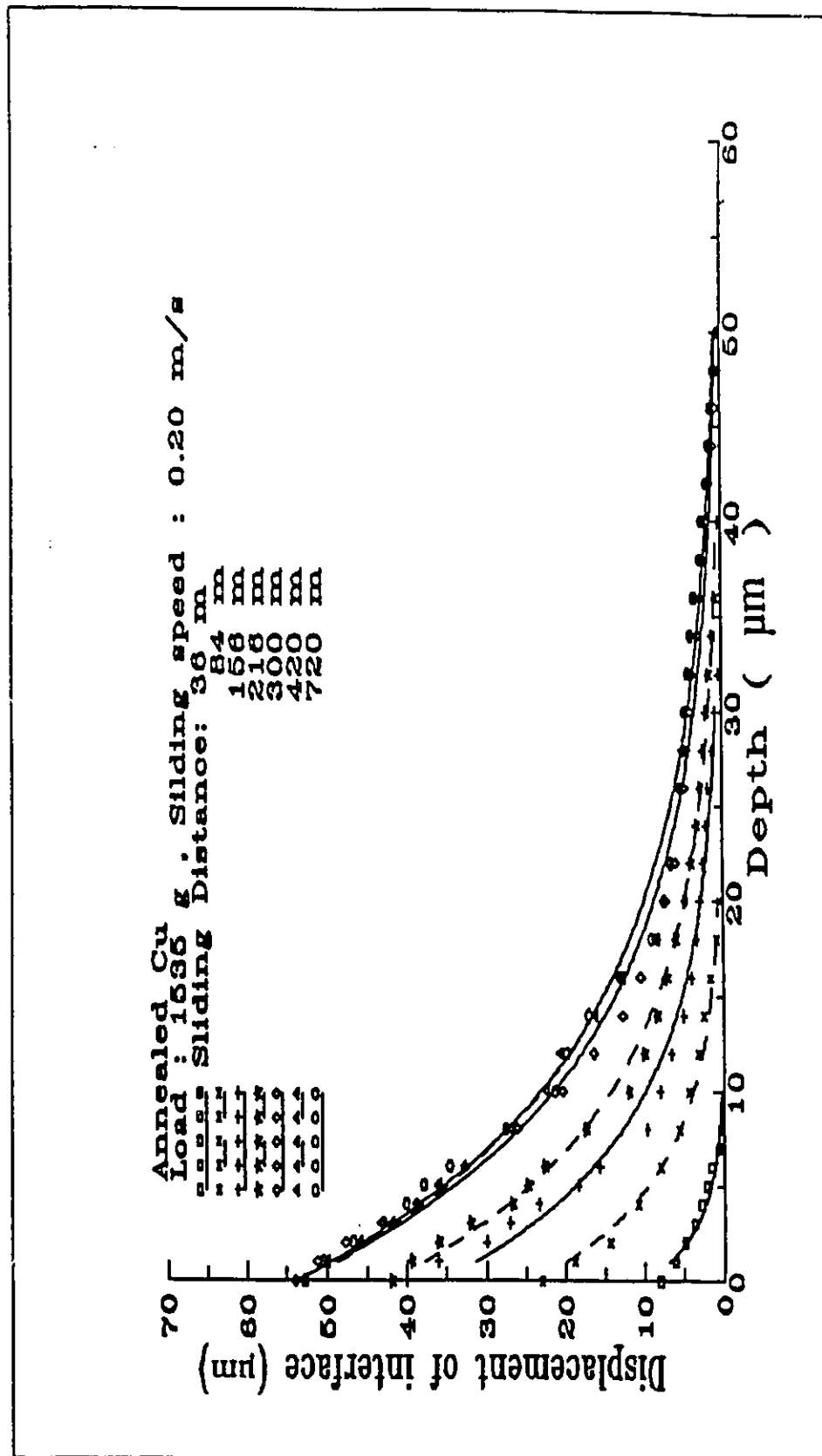
Fig. 4.13. The forward displacements of interface vs sliding distance for annealed Cu.
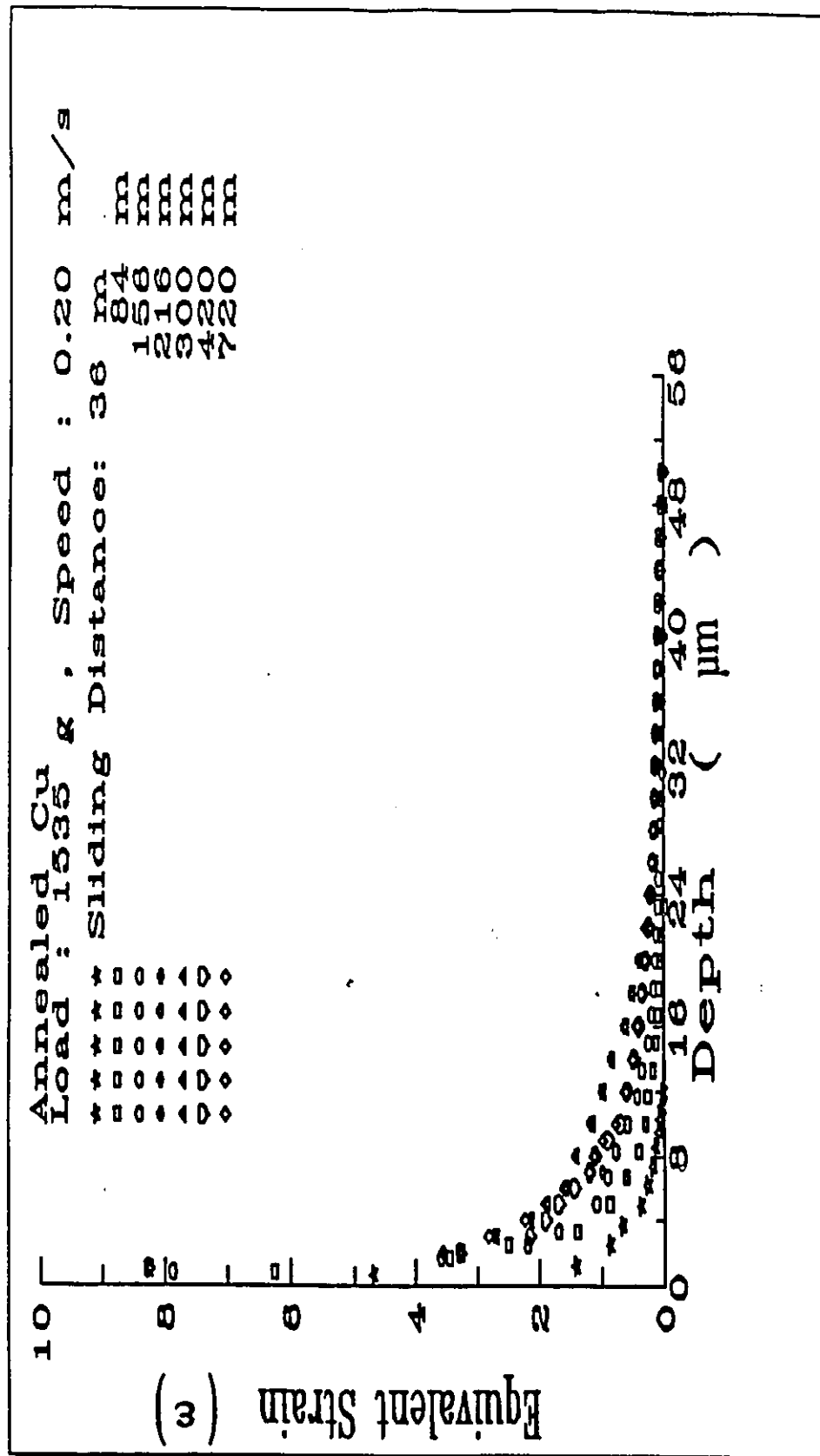
Fig. 4.14: The strain gradients for annealed Cu below the worn surfaces as a function of

sliding distance.

112
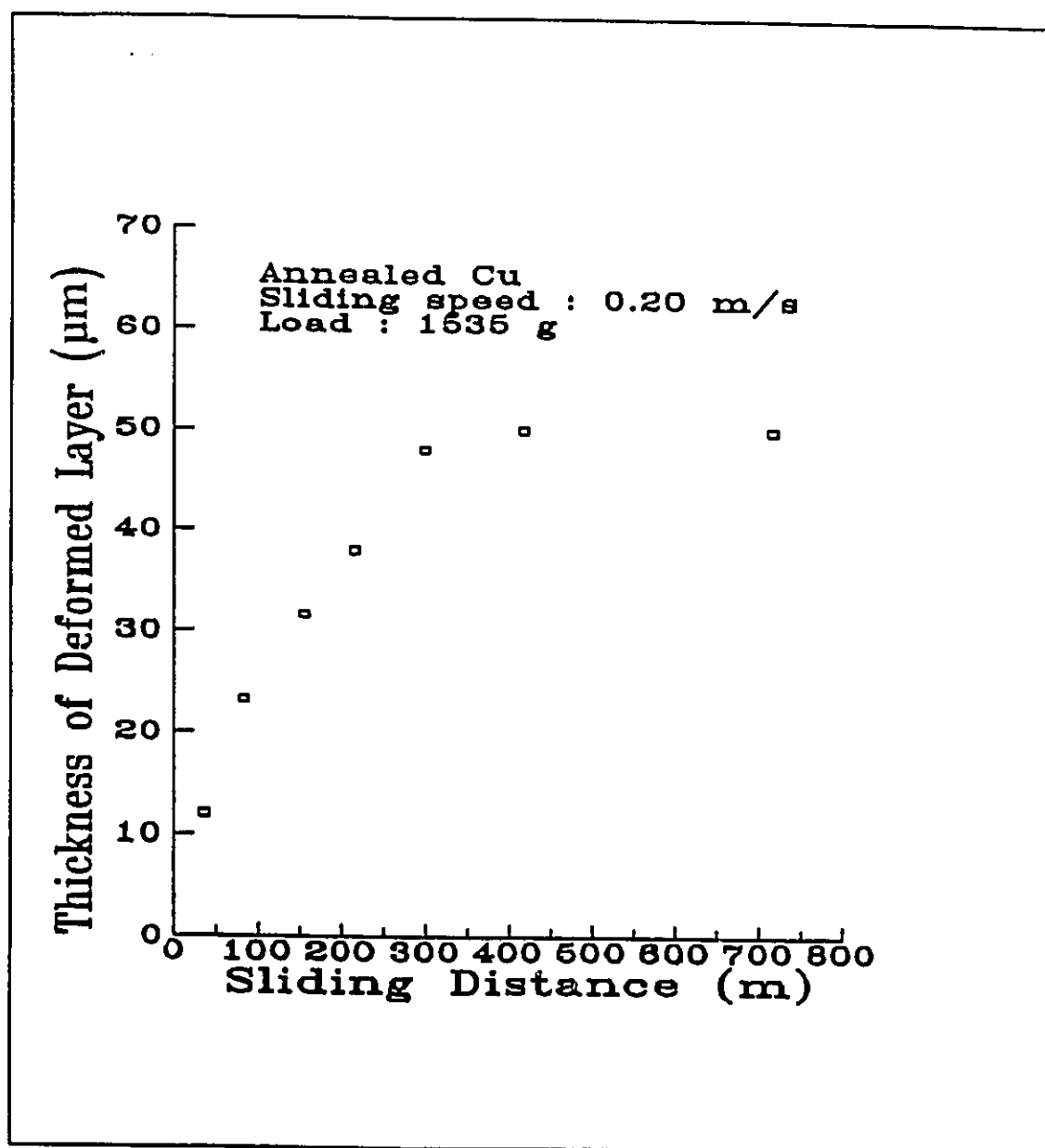
Fig. 4.15: The thickness of deformed layer increases with sliding distance.

(a)

Fig. 4.16: (a) The top view, (b) the side view of a flake-shape debris.
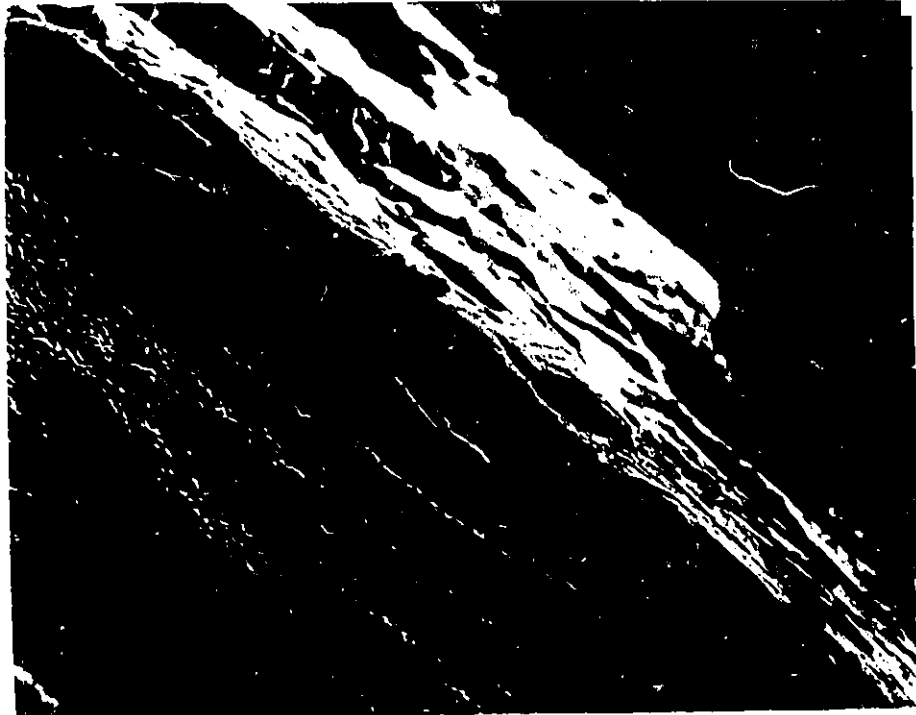
(b)

Fig. 4.16 (continued) (b)
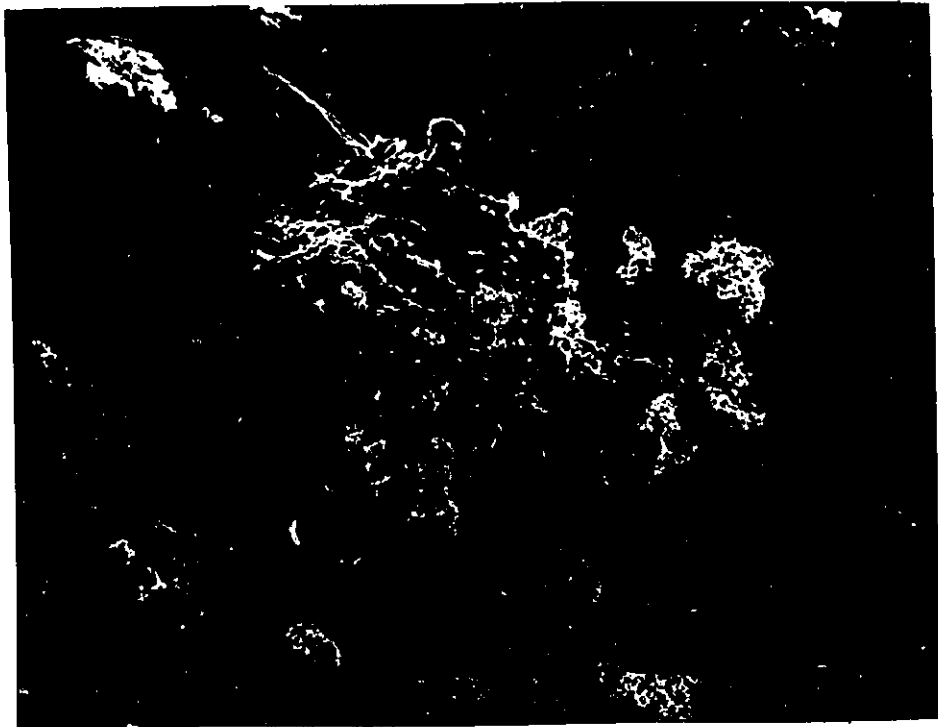
Fig. 4.17: A mixture of flake-shape debris and oxide particles.

Fig. 4.18: SEM micrograph shows oxide particle wear debris
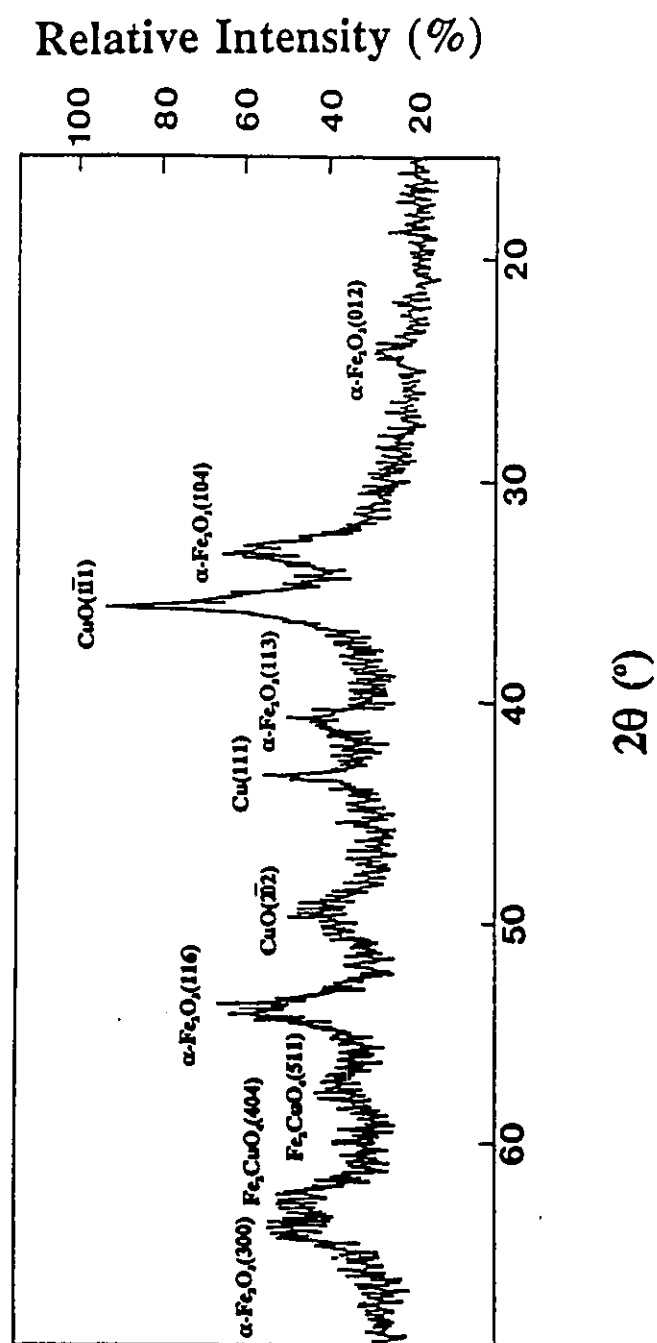
Fig. 4.19: Major X-ray diffraction peaks for wear debris of annealed Cu.
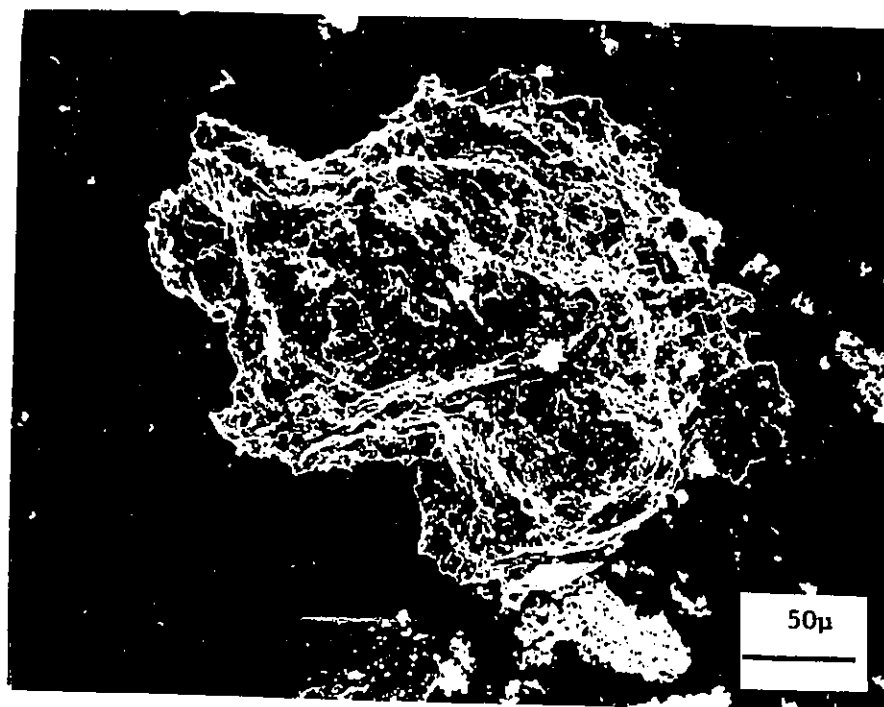
Fig. 4.20: Fe flake debris found by EDX analysis.
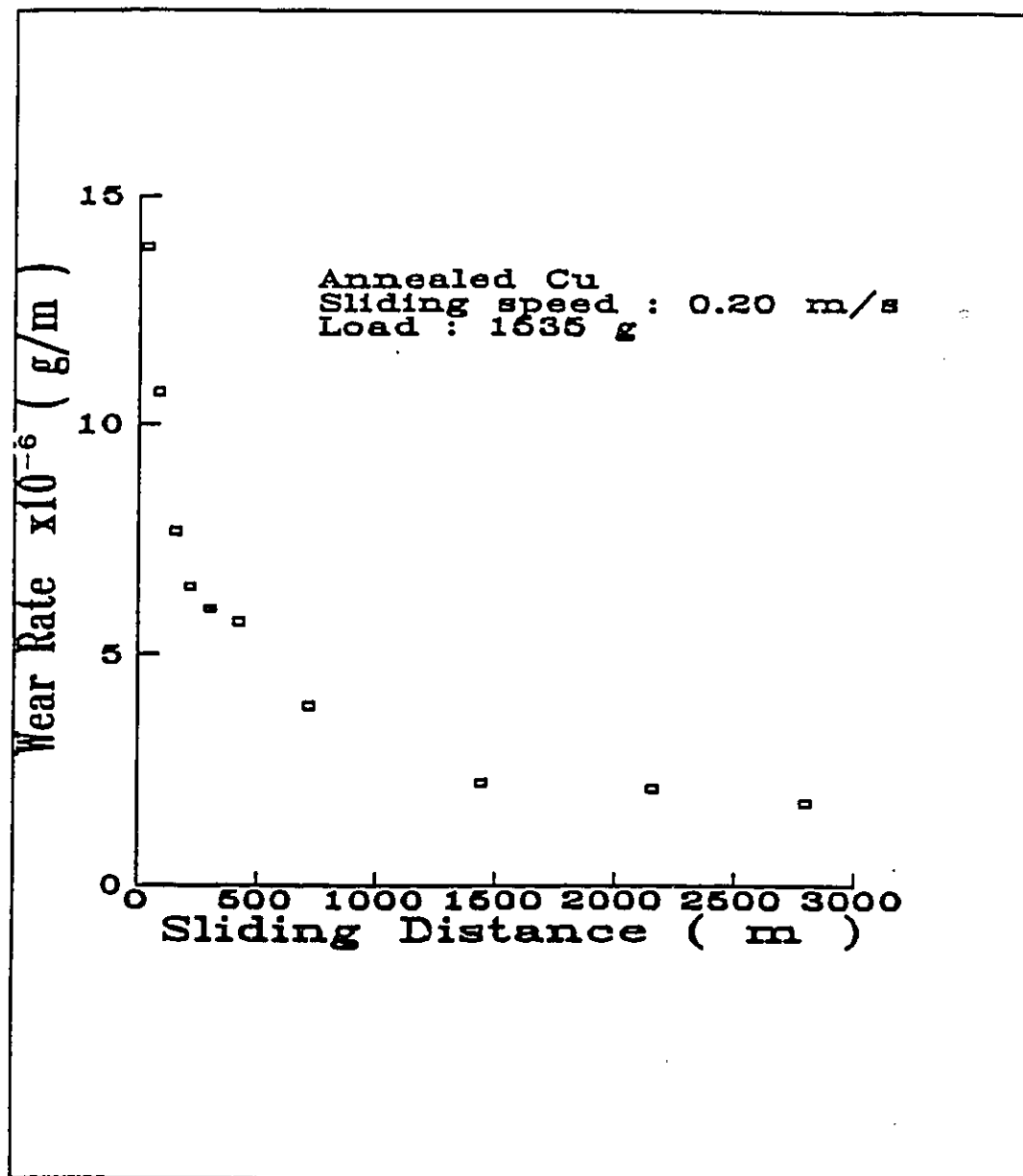
Fig. 4.22: The wear rate decreases with sliding distance for annealed Cu.
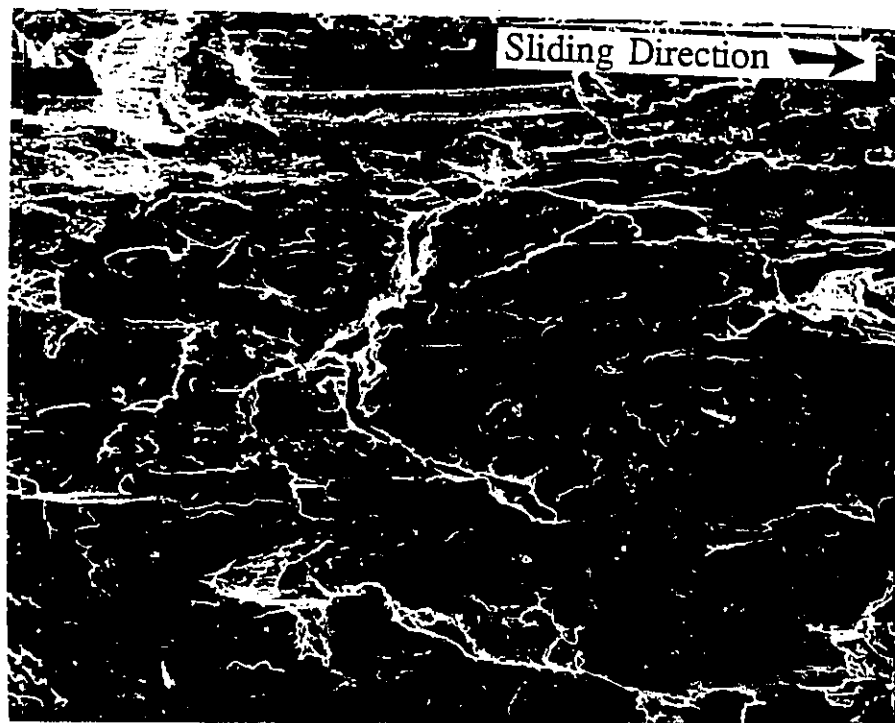
Fig. 4.23: The wear surface topography is characterized by deformation and surface cracks.

Fig. 4.23: Flake-shape debris lifted off the plane of the worn surface.
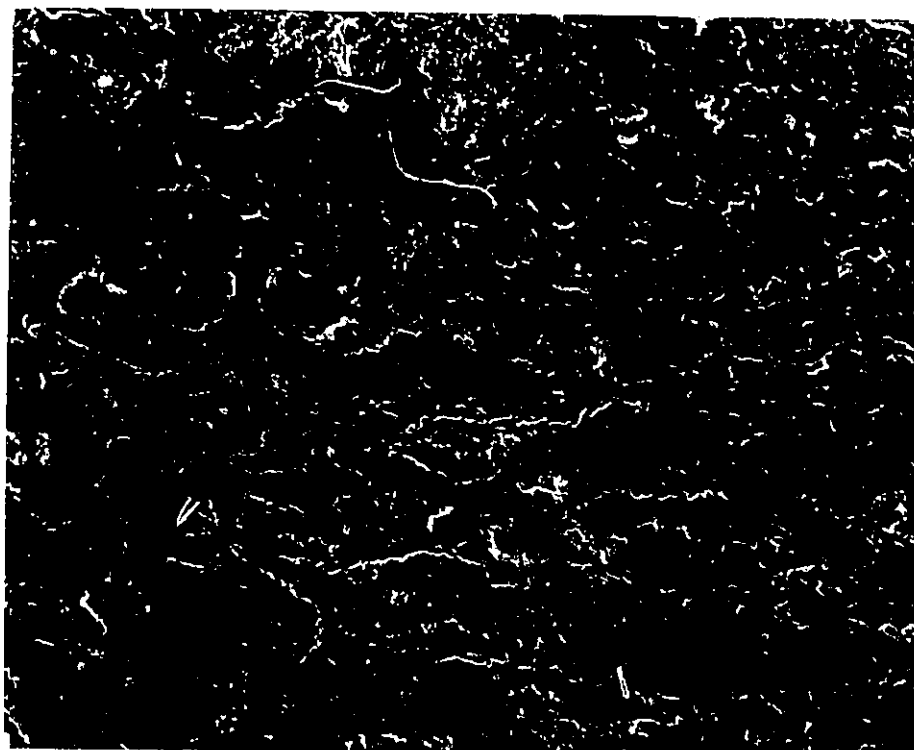
Fig. 4.24: Oxide formation on the worn surface.
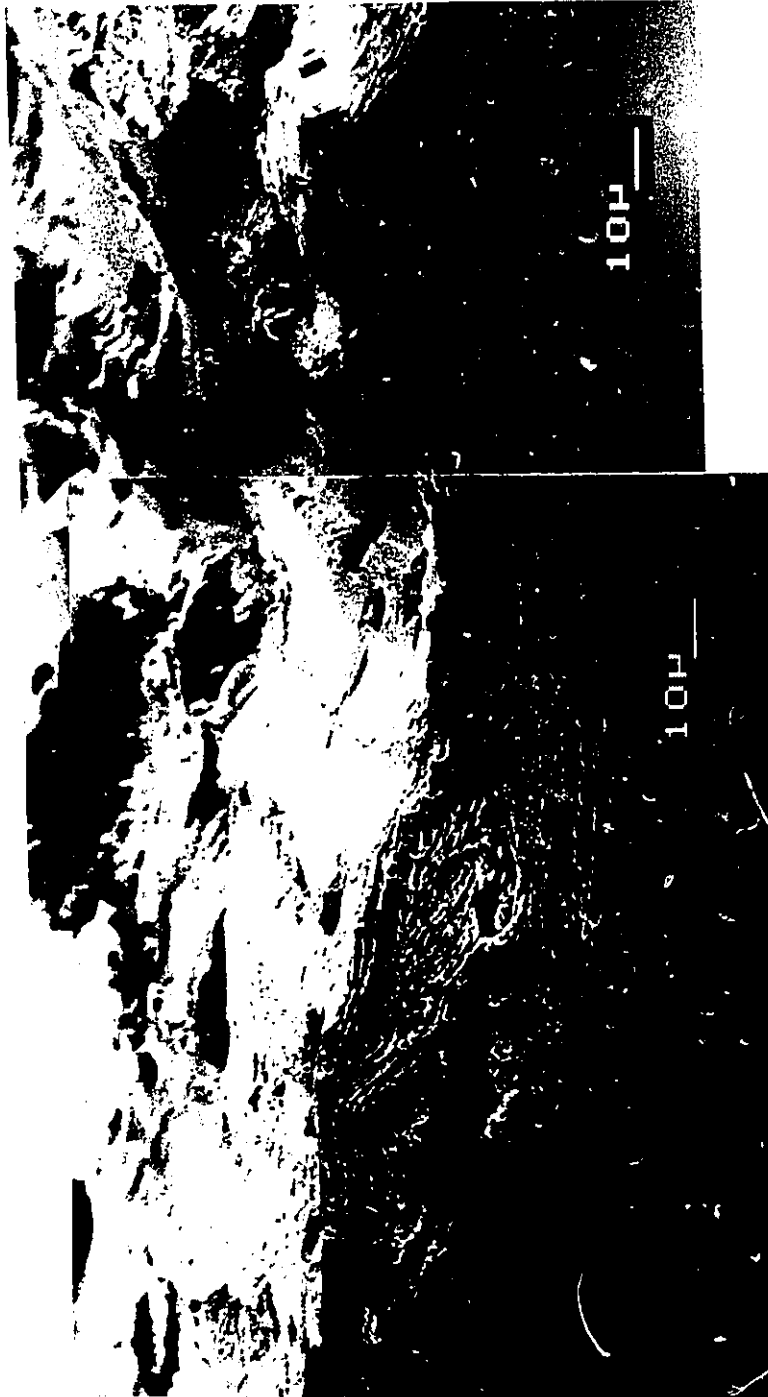
Fig. 4.25: Cracks below the wear surface propagate to lead to debris formation on transverse section.

Fig. 4.26: The voids coalesce to form the cracks on transverse section.

125
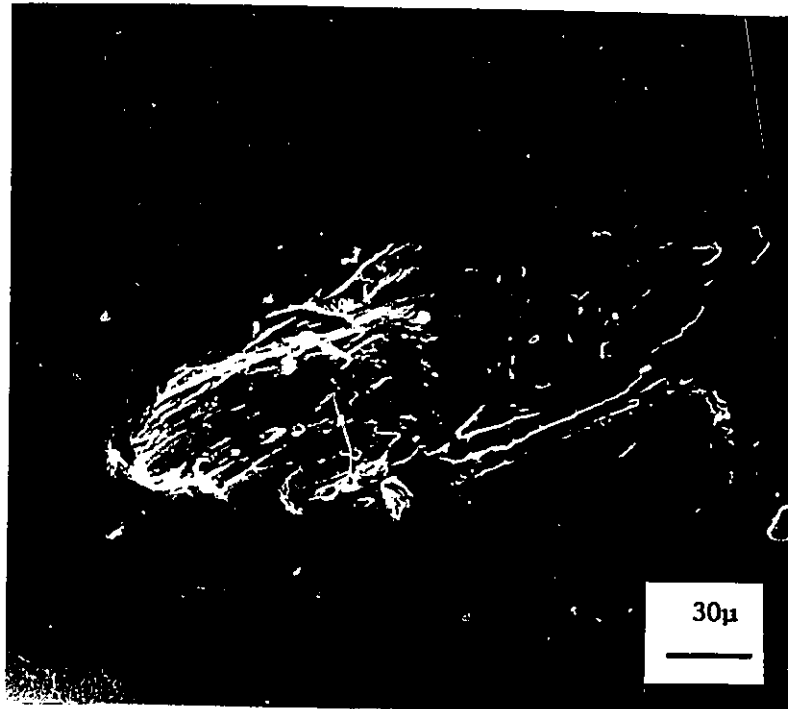
(a)

Fig. 4.27: (a) The top view, (b) the side view of a flake-shape debris from rolled Cu.

(b)

Fig. 4.27 (continued) (b)
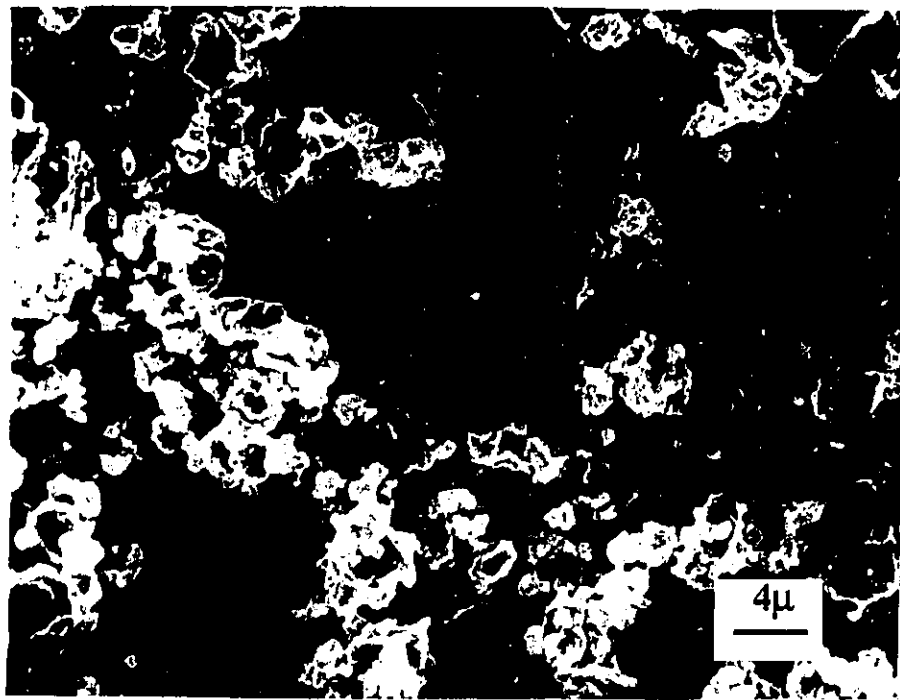
Fig. 4.28: Oxide particle wear debris from rolled Cu.
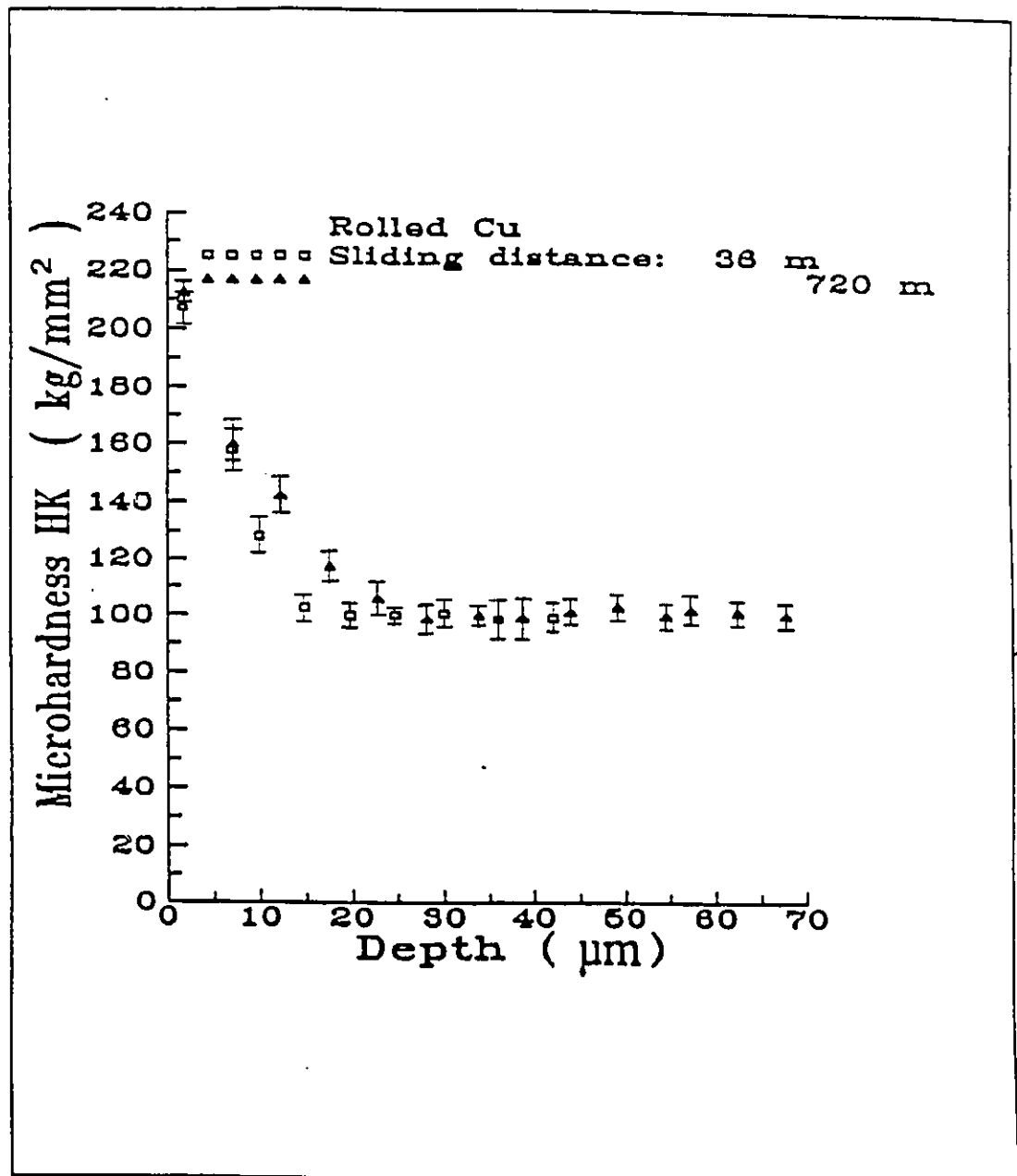
Fig. 4.29: Microhardness profiles for rolled Cu below the wear surface at two different

sliding distances (normal load =1535 g).
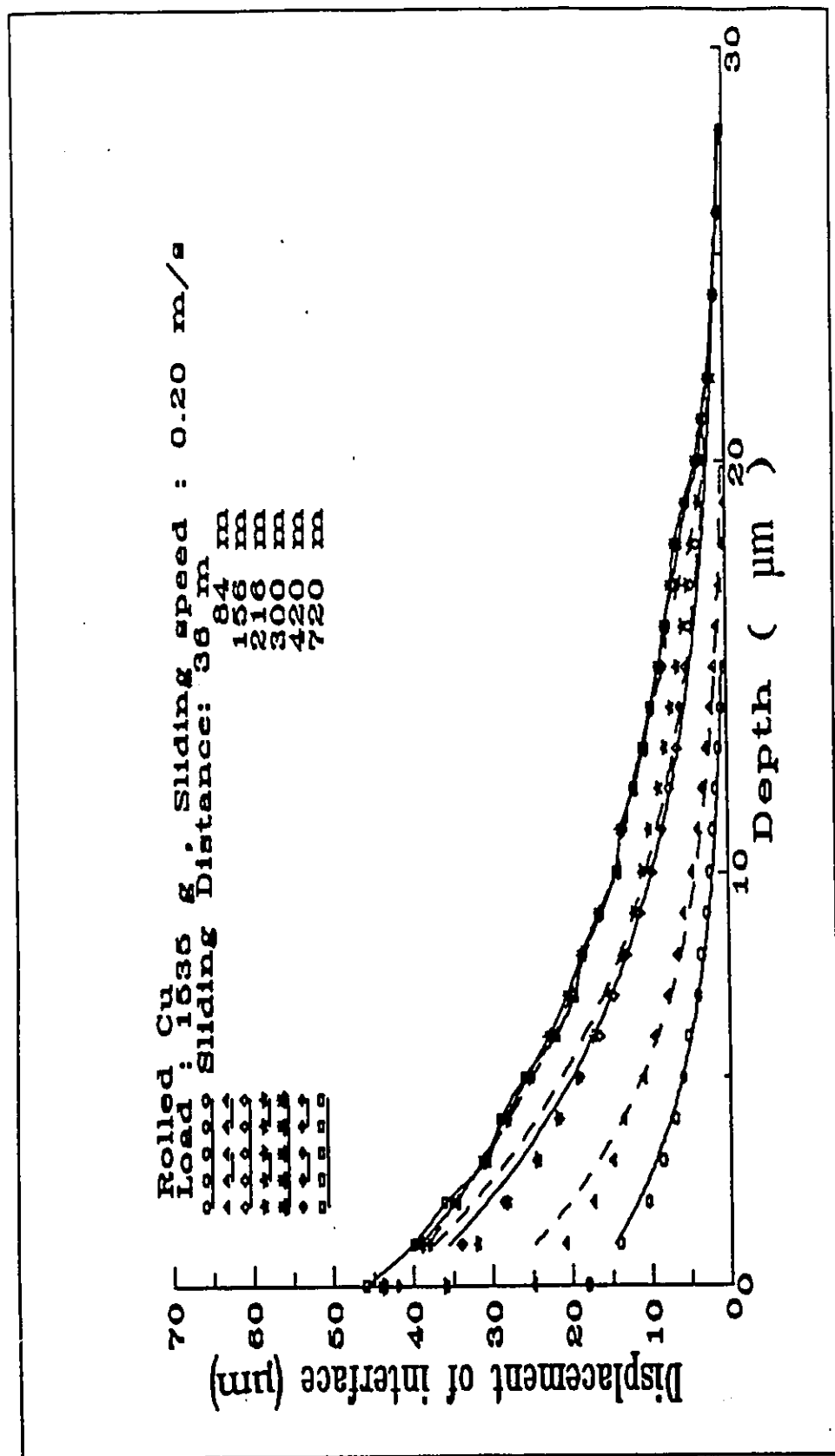
Fig. 4.30: The forward displacements vs sliding distance for rolled Cu.
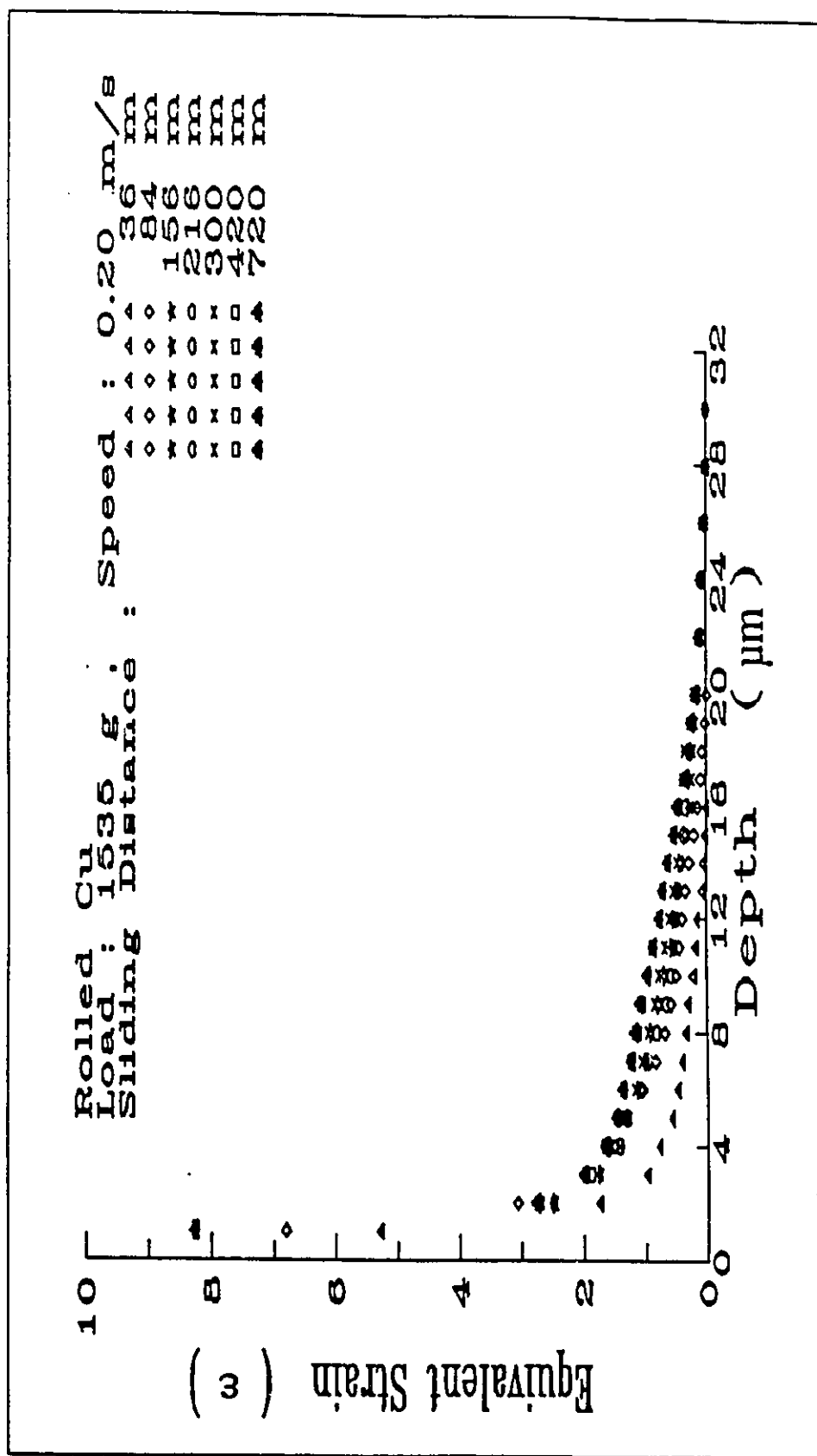
Fig. 4.31: Equivalent strain gradient distributions below the worn surface for rolled Cu.
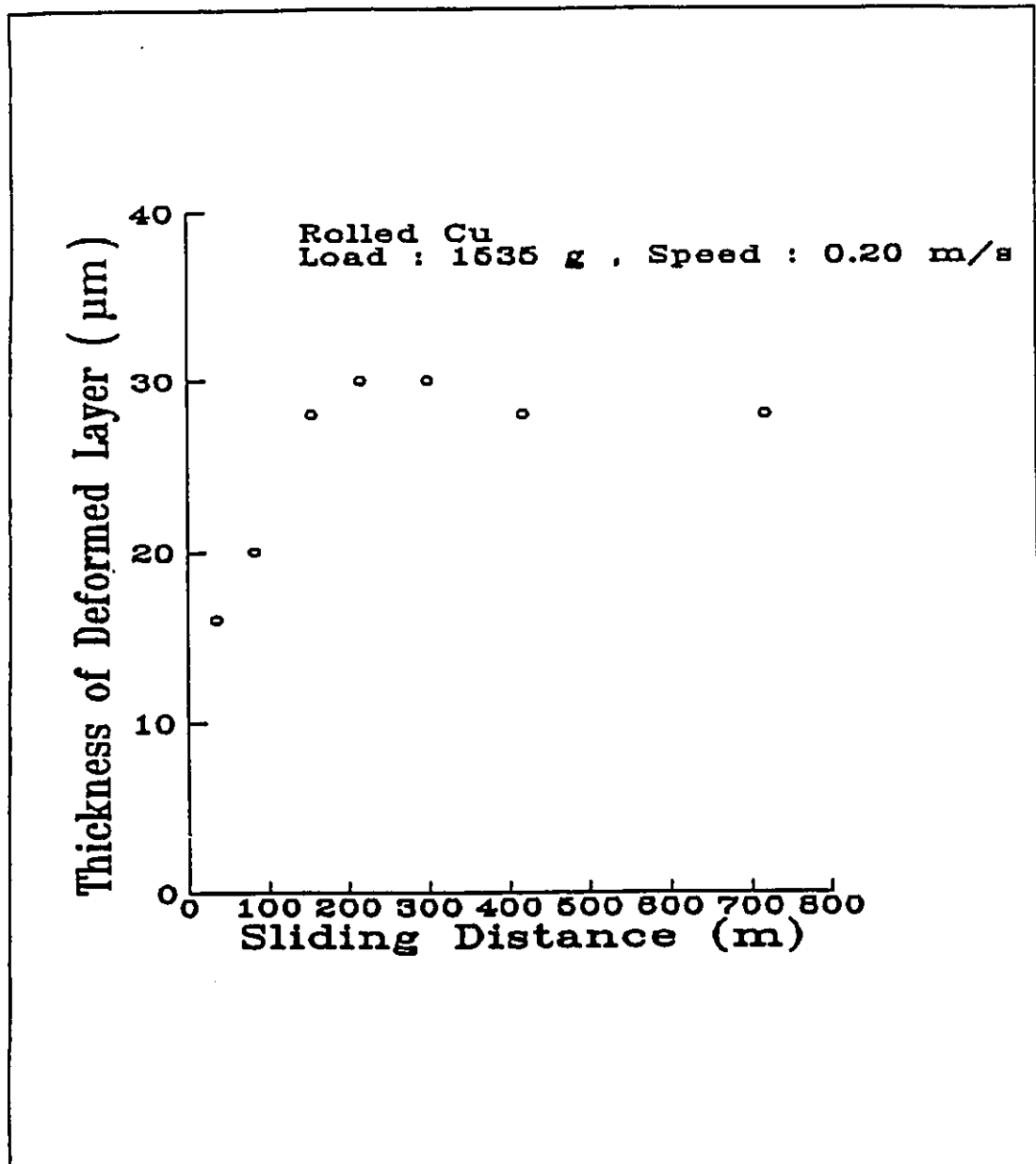
Fig. 4.32: The thickness of deformed layer increases with sliding distance to a

constant value for rolled Cu.
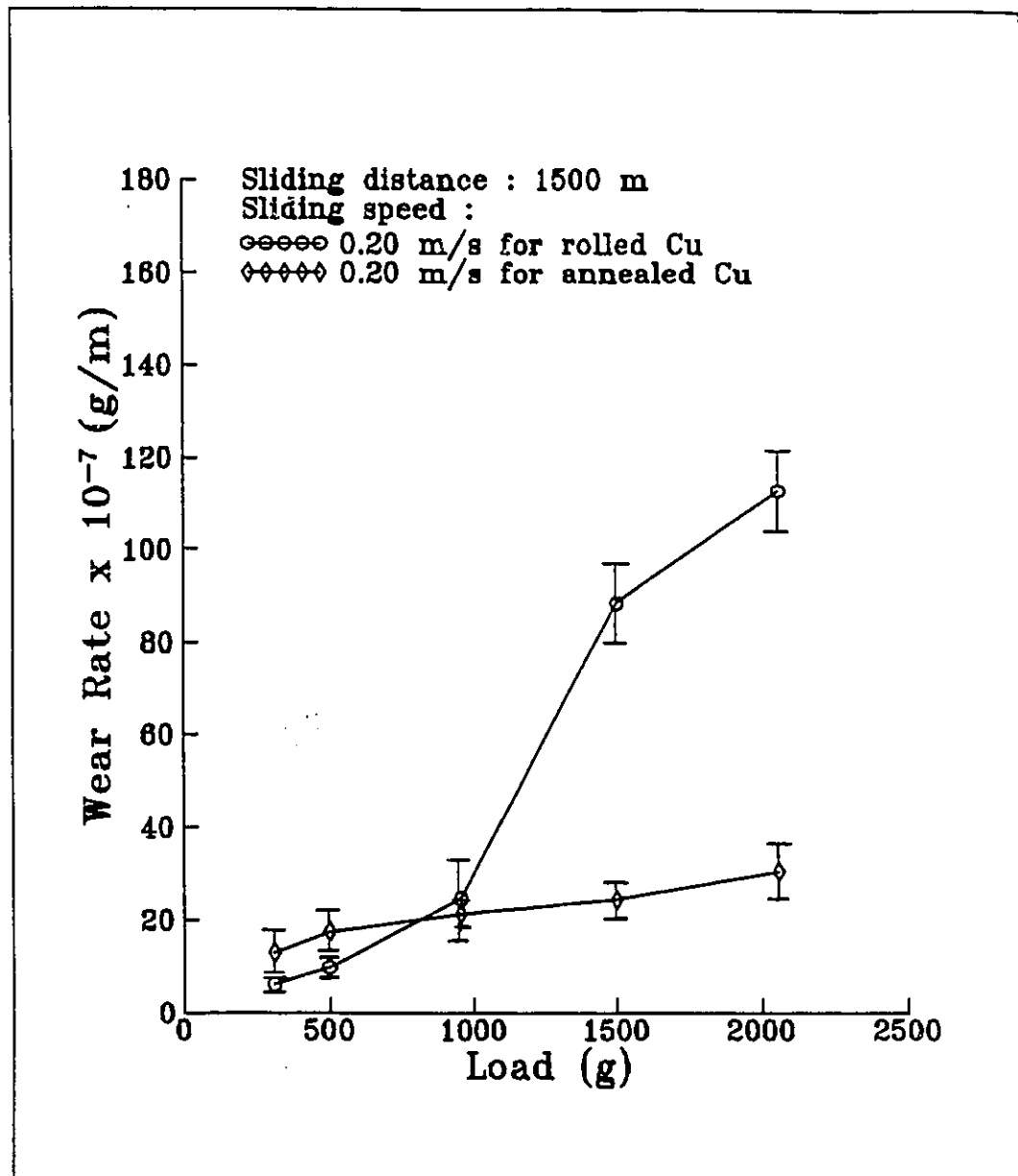
Fig.4.33: Wear rate of rolled Cu and annealed Cu as a of function of load.
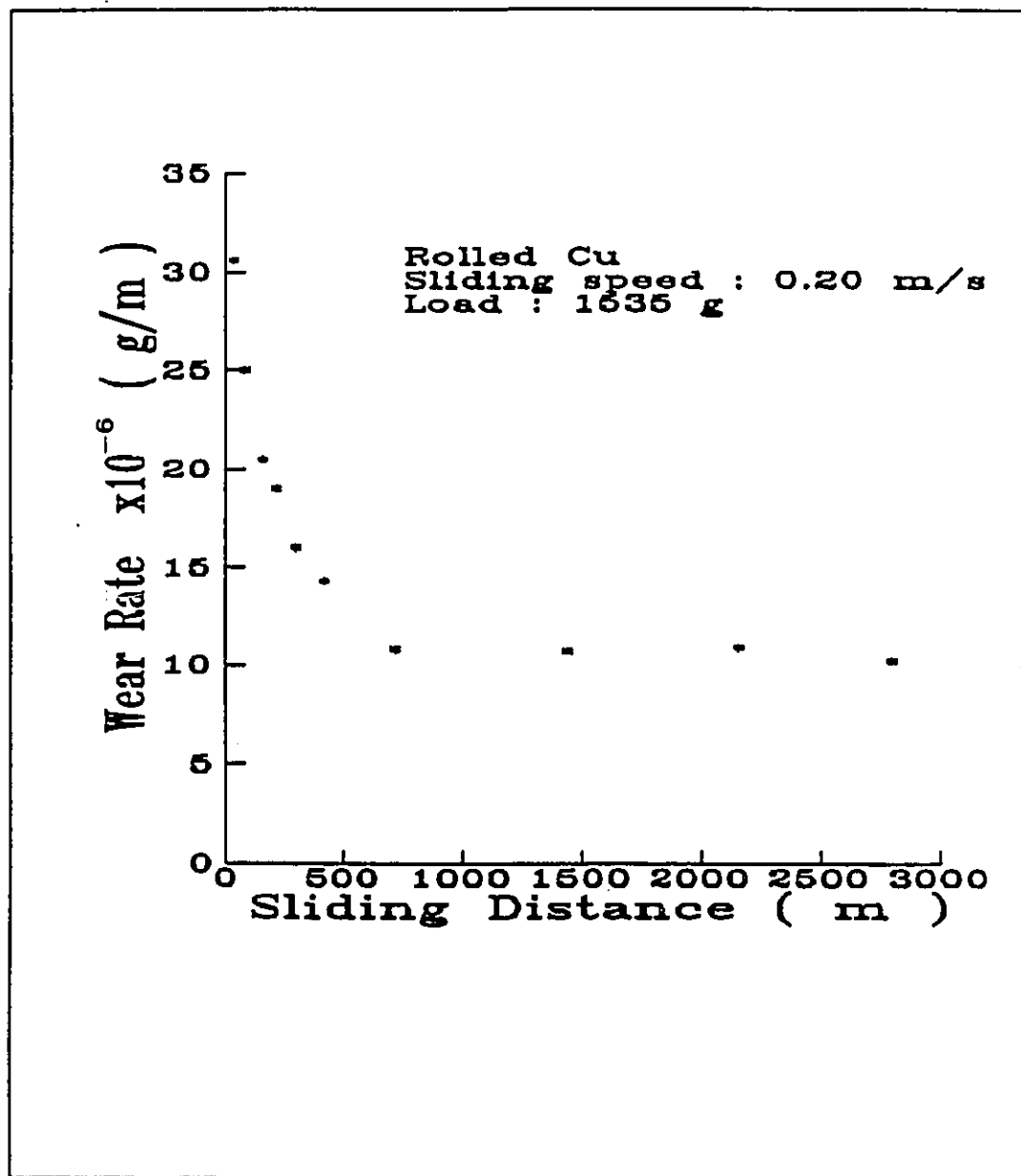
Fig. 4.34: The wear rate decreases with sliding distance for rolled Cu.
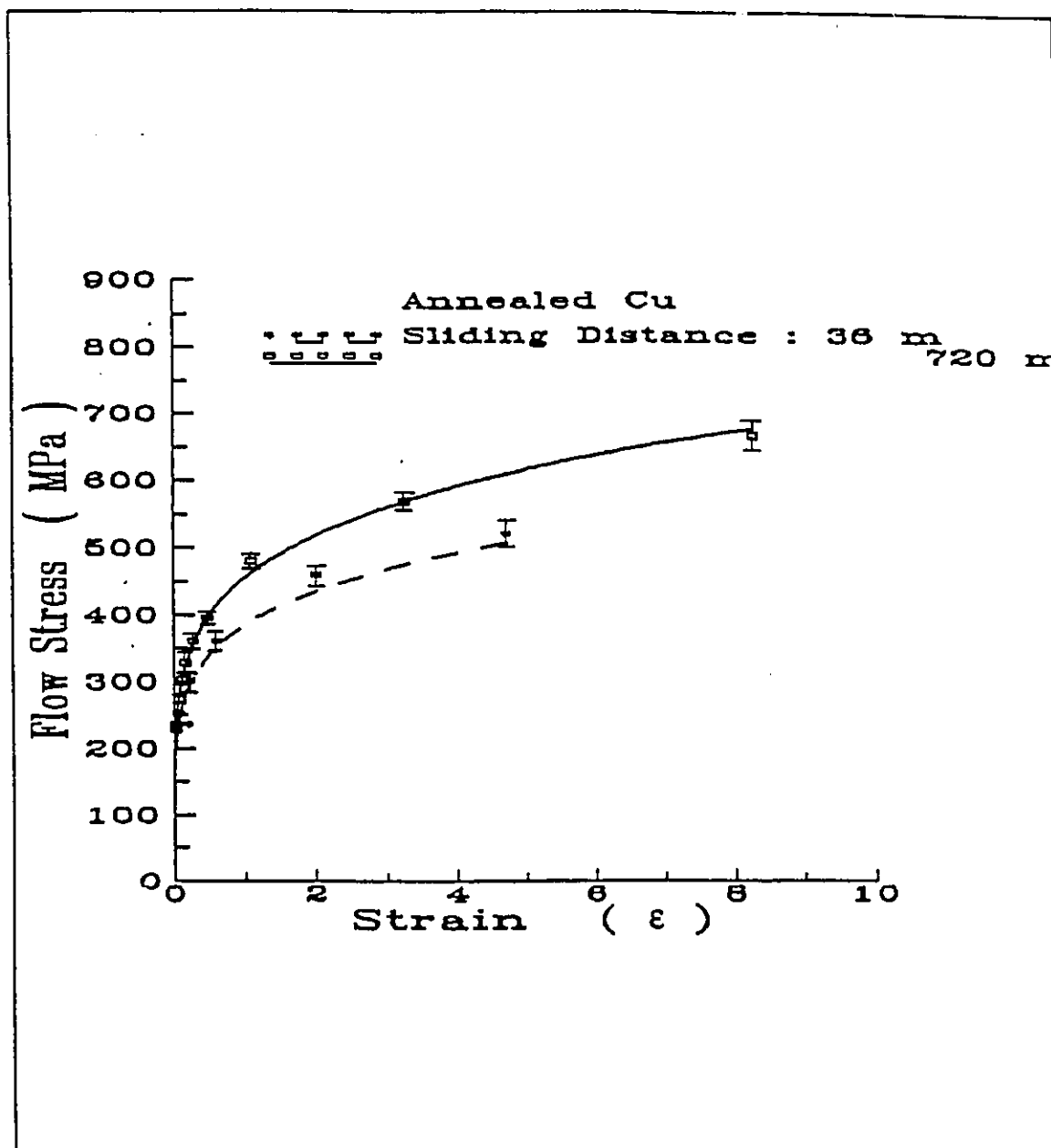
Fig. 5.1: Stress vs strain curves at two different sliding distances for annealed Cu with best fit (dash line and solid line) represented by a power expression, $\sigma = K(\varepsilon)^a$.
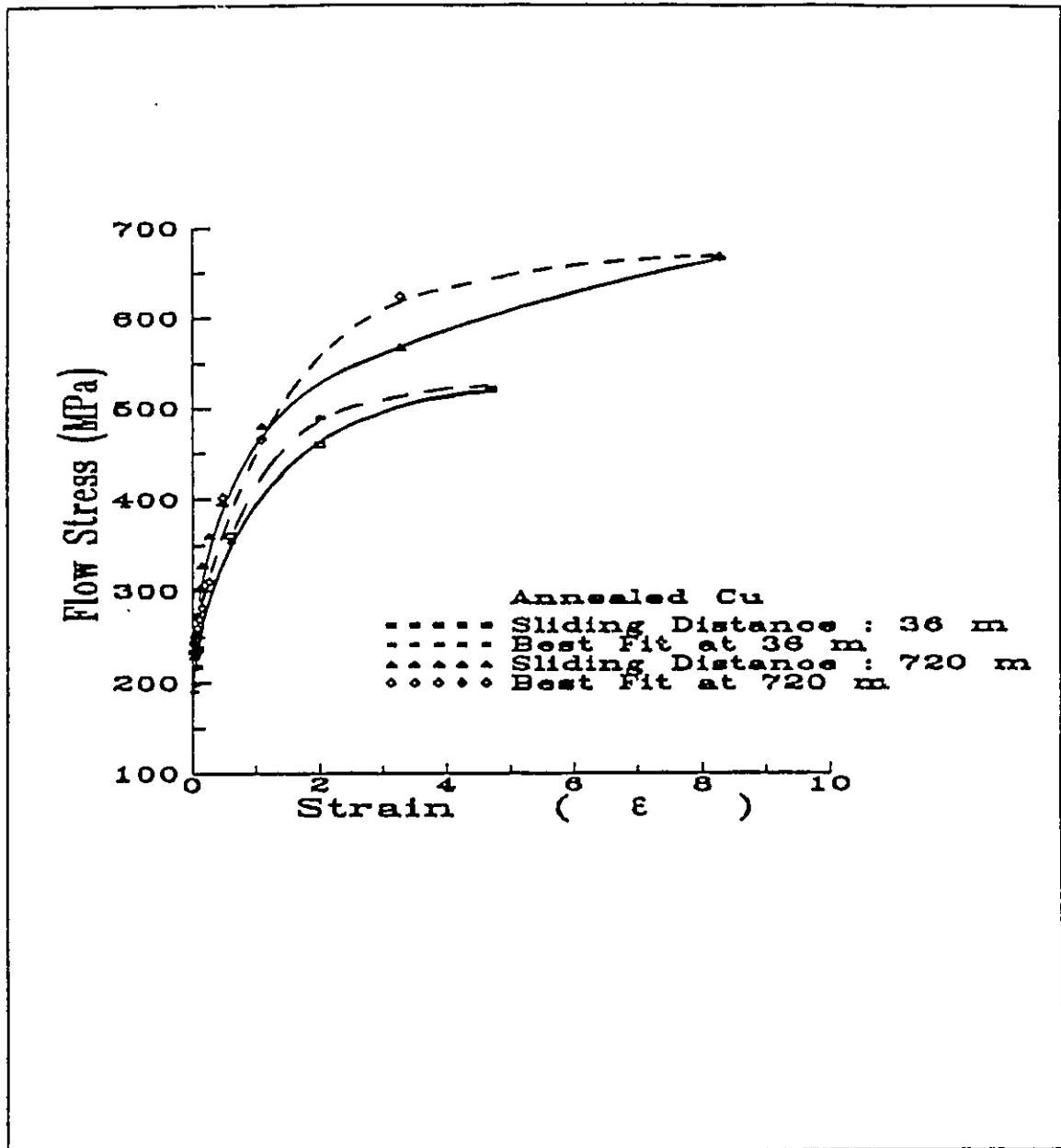
Fig. 5.2: Stress-strain behavior for annealed Cu represented by Voce equation,

$$\sigma = \sigma_s - (\sigma_s - \sigma_o)e^{-\varepsilon/\varepsilon_c}.$$
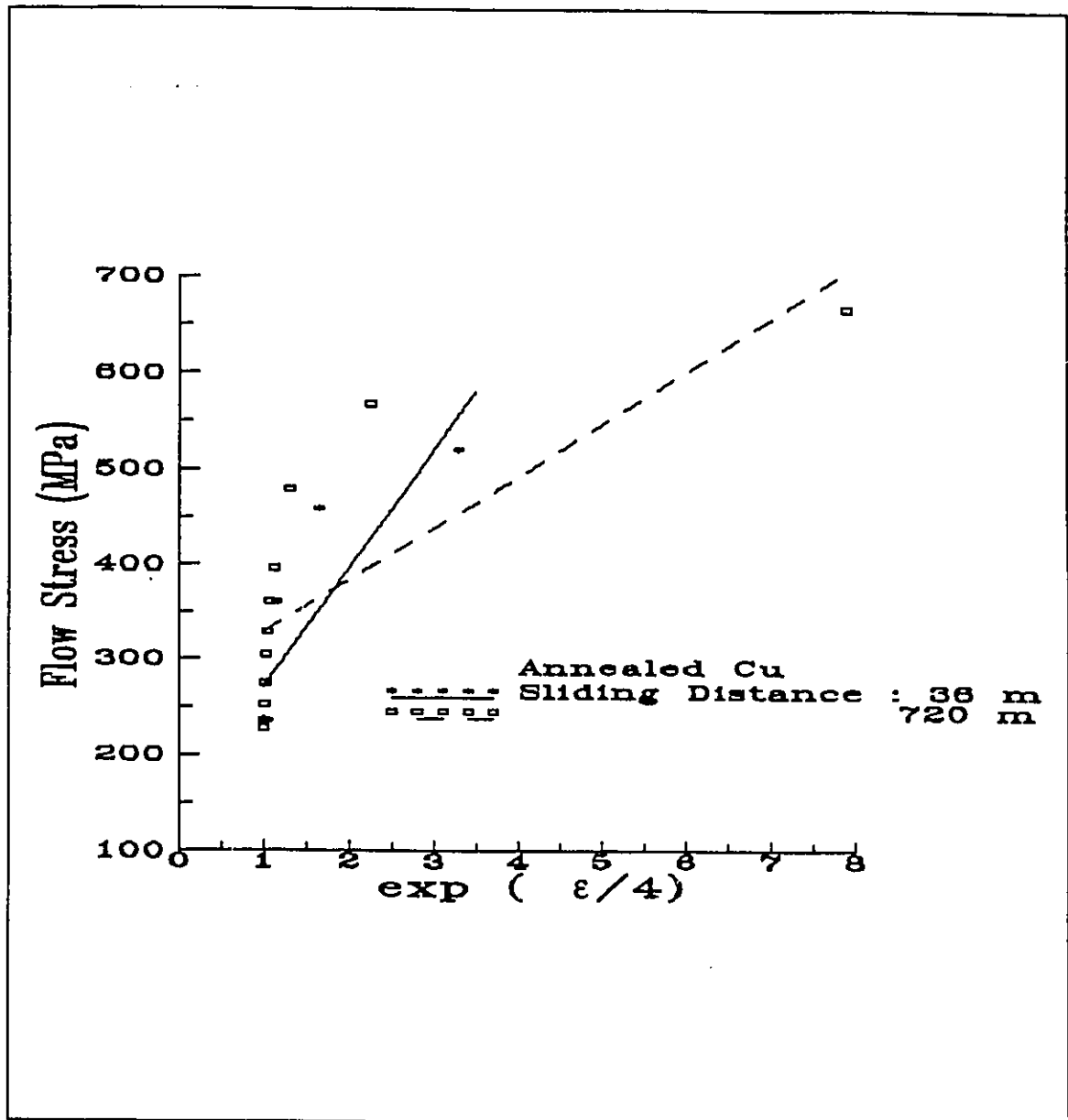
Fig. 5.3: Stress-strain behavior for annealed Cu represented by Embury equation,

$\sigma = f [\exp(\varepsilon/4)]$.
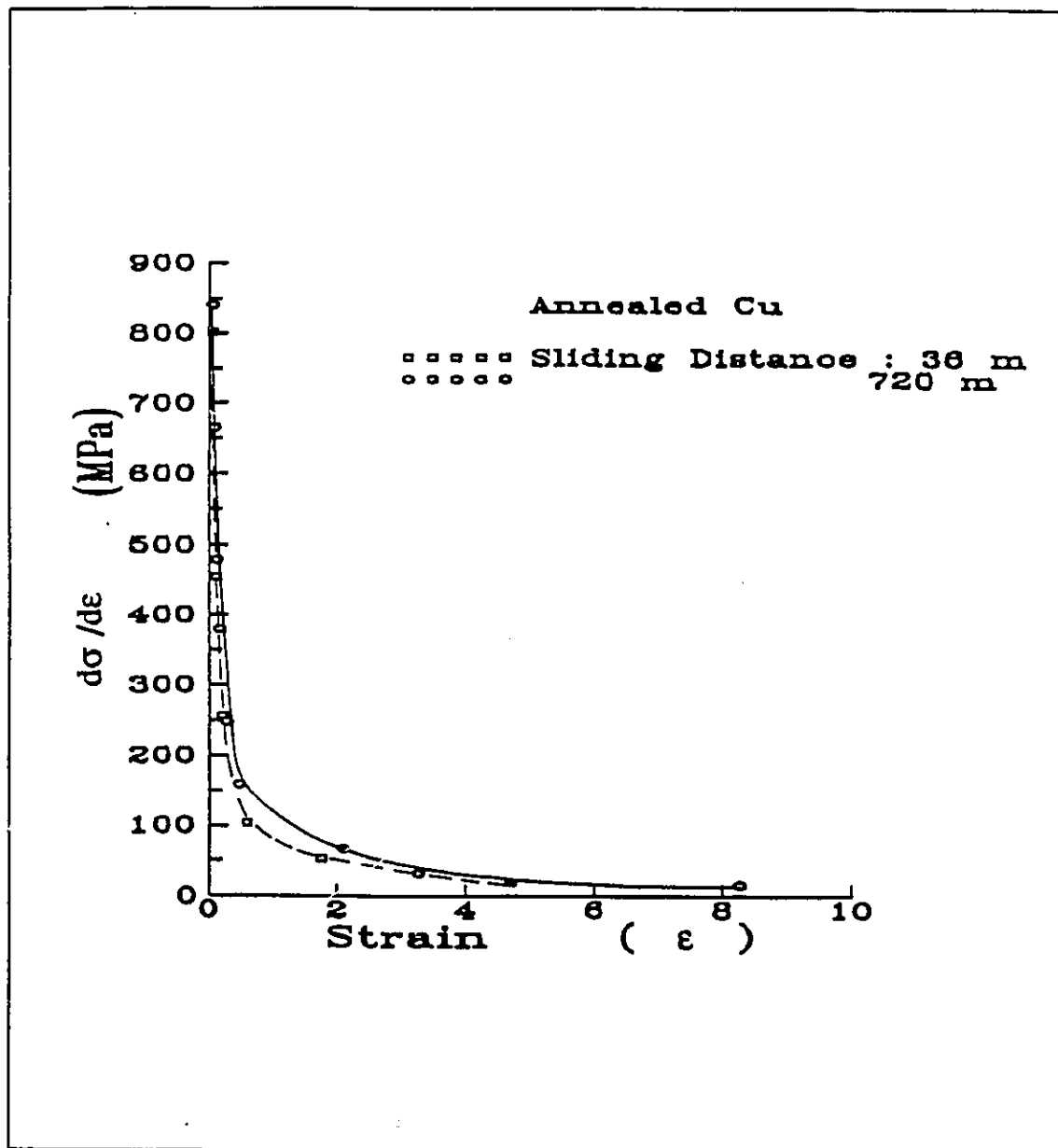
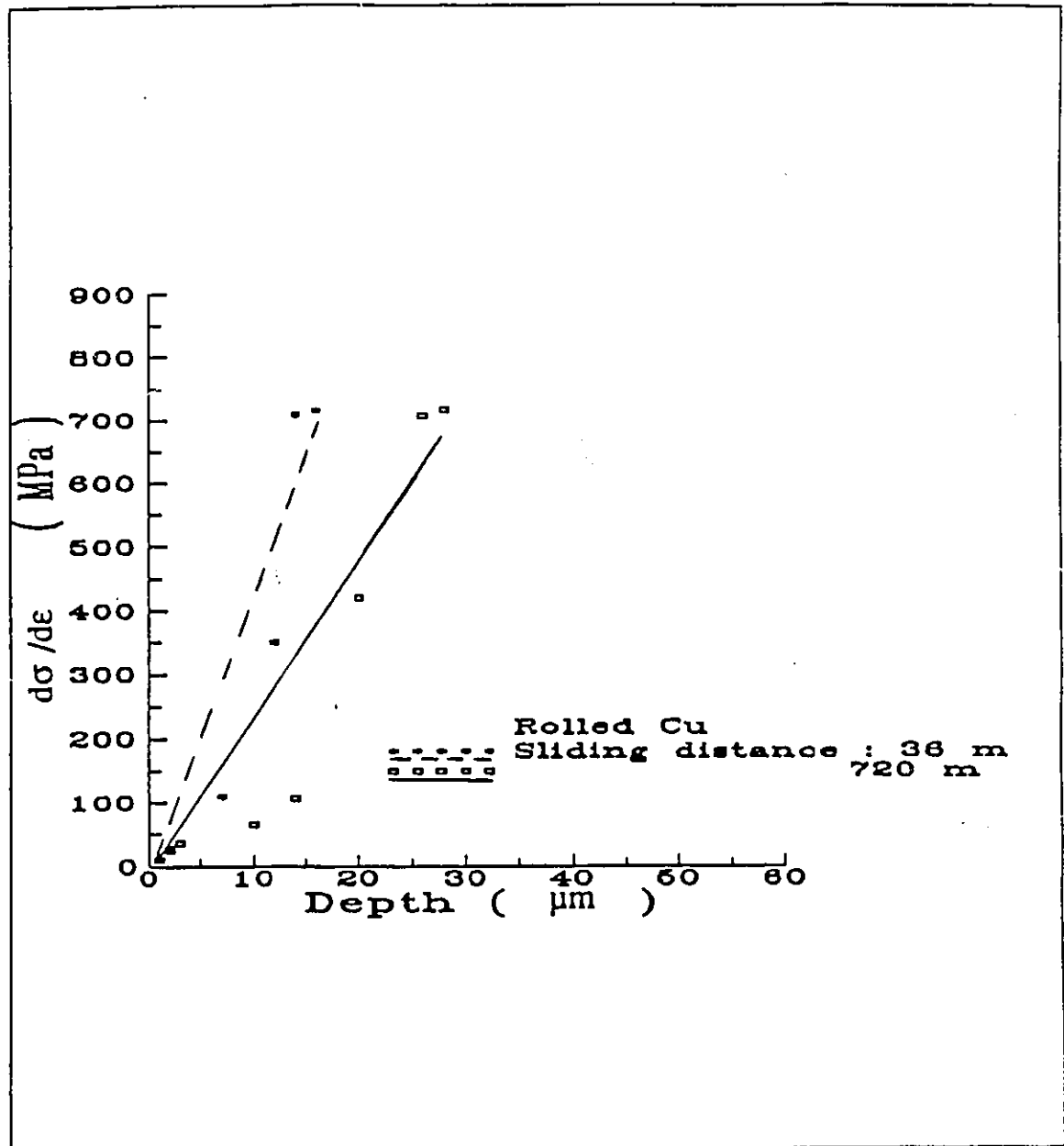Fig. 5.4: Variation in work hardening rate with strain for annealed Cu

138
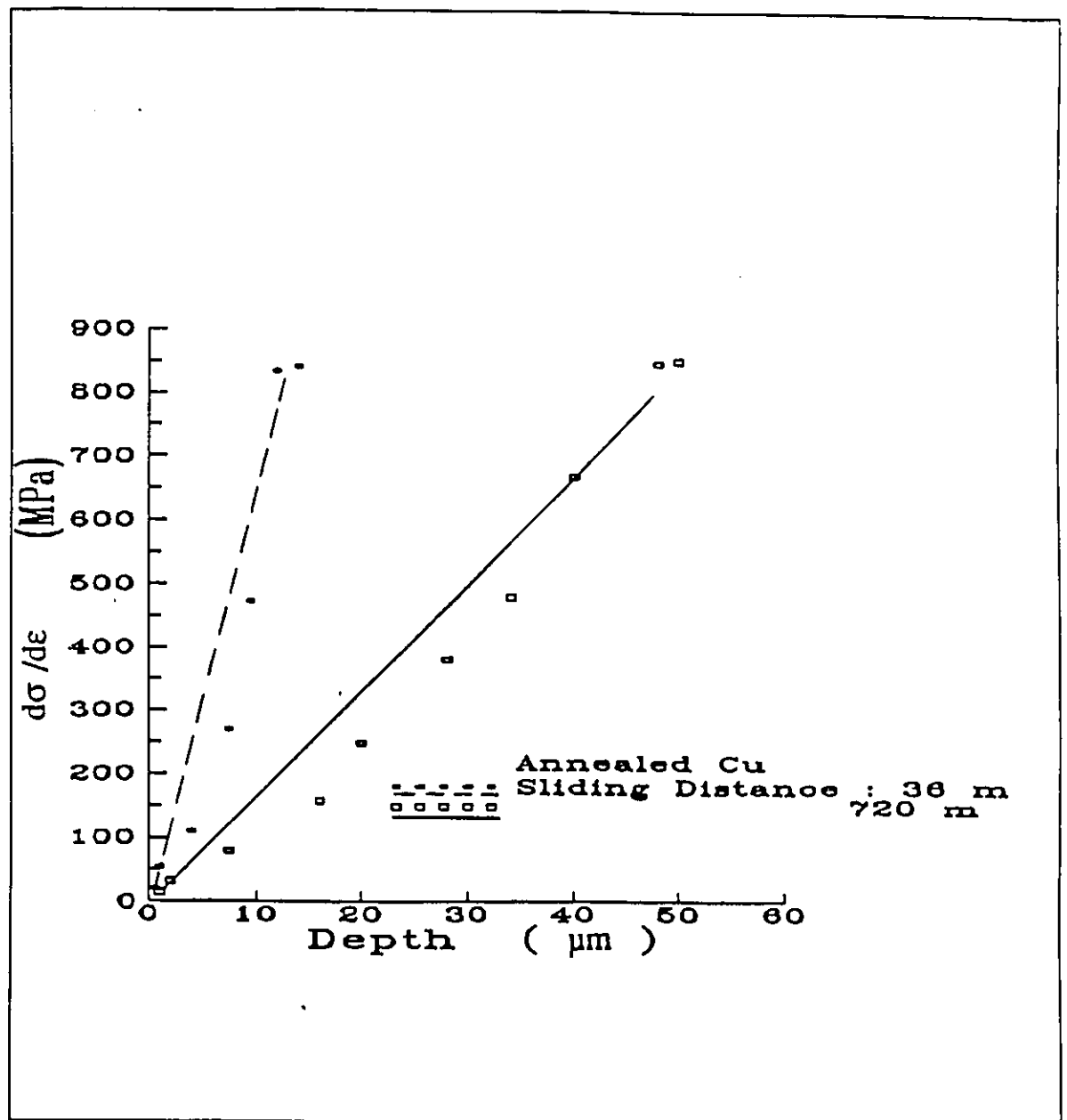
Fig. 5.5: Work hardening rate vs depth below the worn surface at two different sliding

distances for annealed Cu.
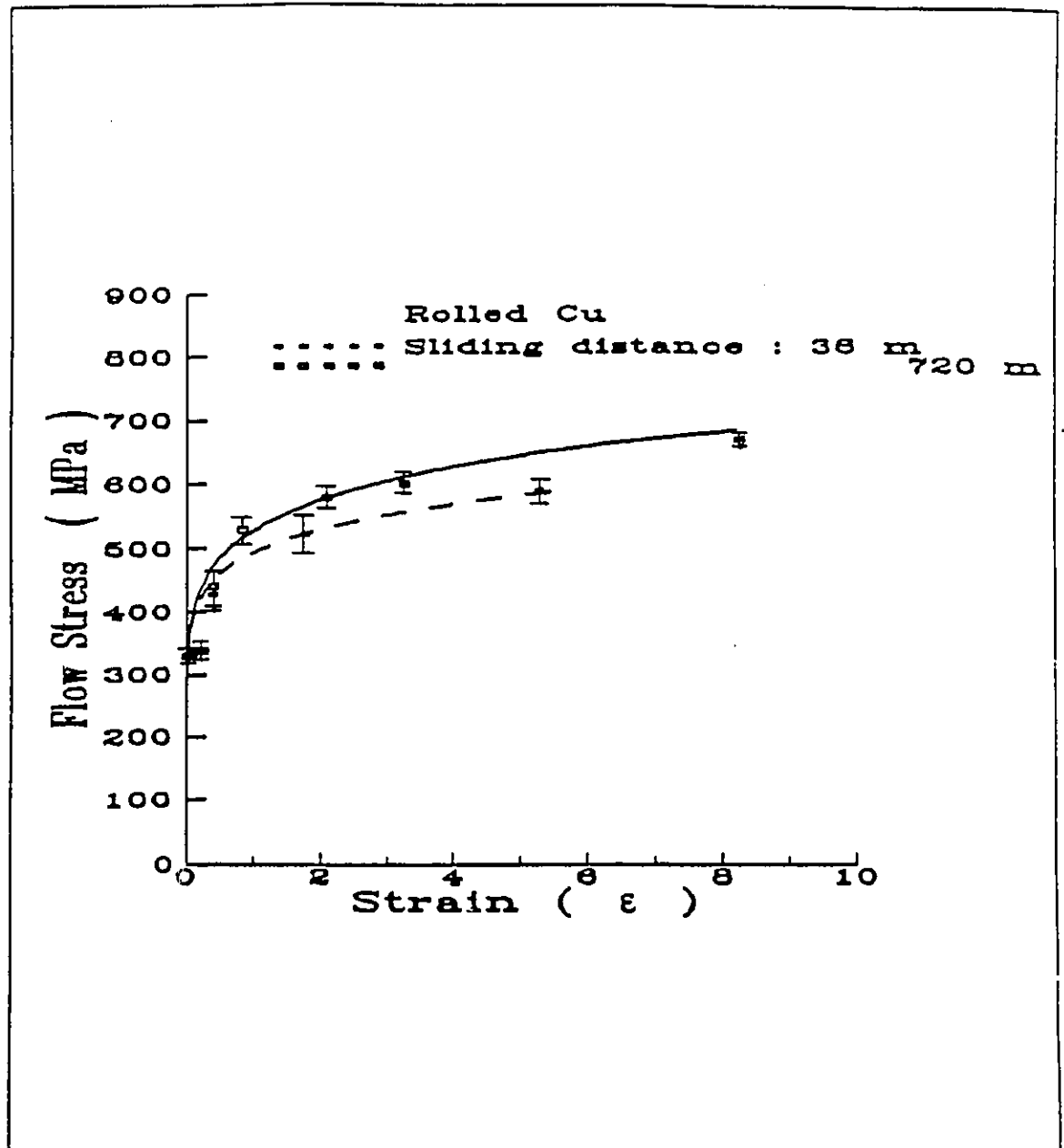
Fig. 5.6: Stress vs strain curves at two different sliding distances for rolled Cu with best fit (dash line and solid line) represented by a power expression, $\sigma = K(\varepsilon)^n$.

140
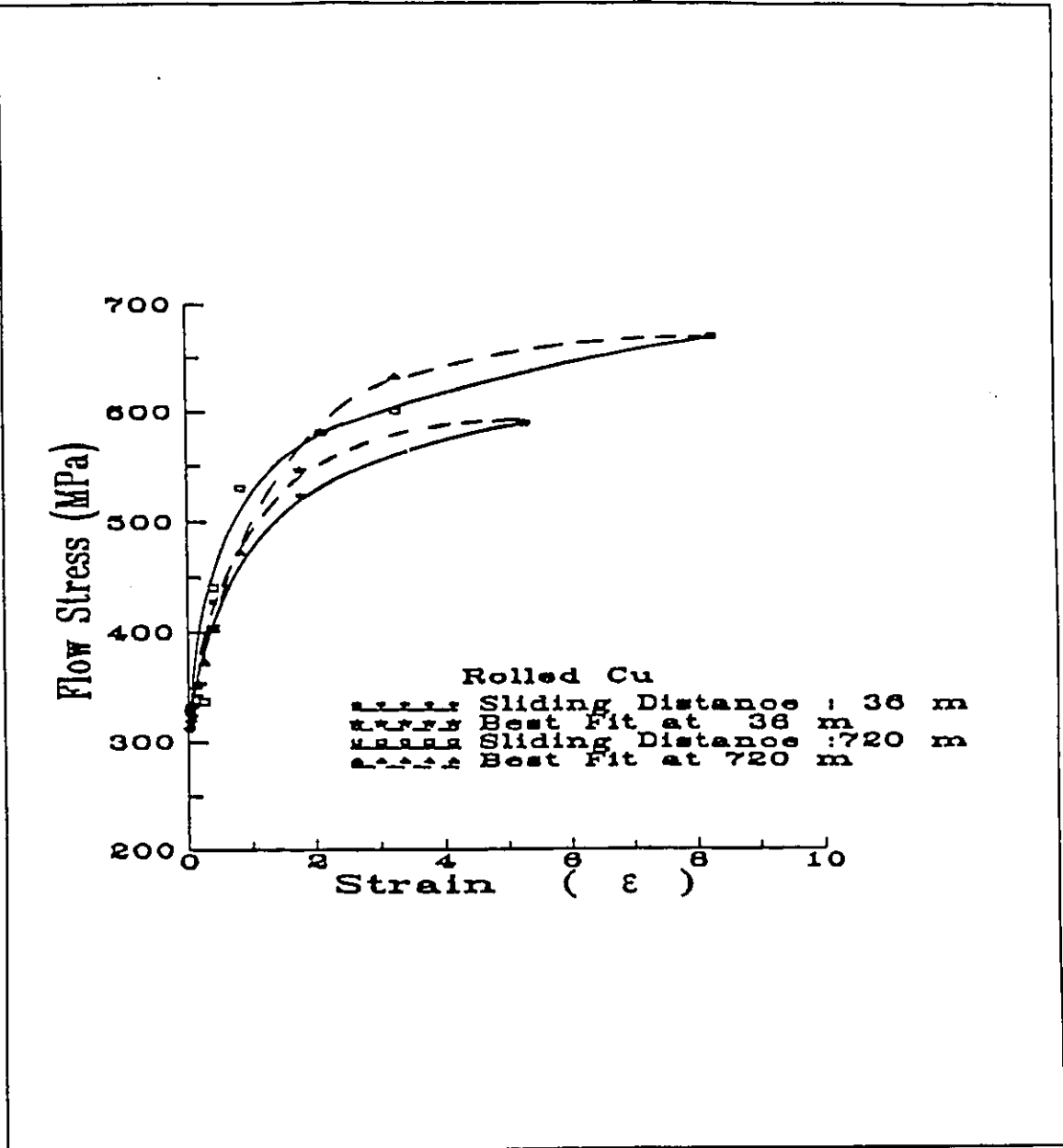
Fig. 5.7: Stress-strain behavior for rolled Cu represented by Voce equation,

$$\sigma = \sigma_s -(\sigma_s -\sigma_o)e^{-\varepsilon/\varepsilon_c}.$$
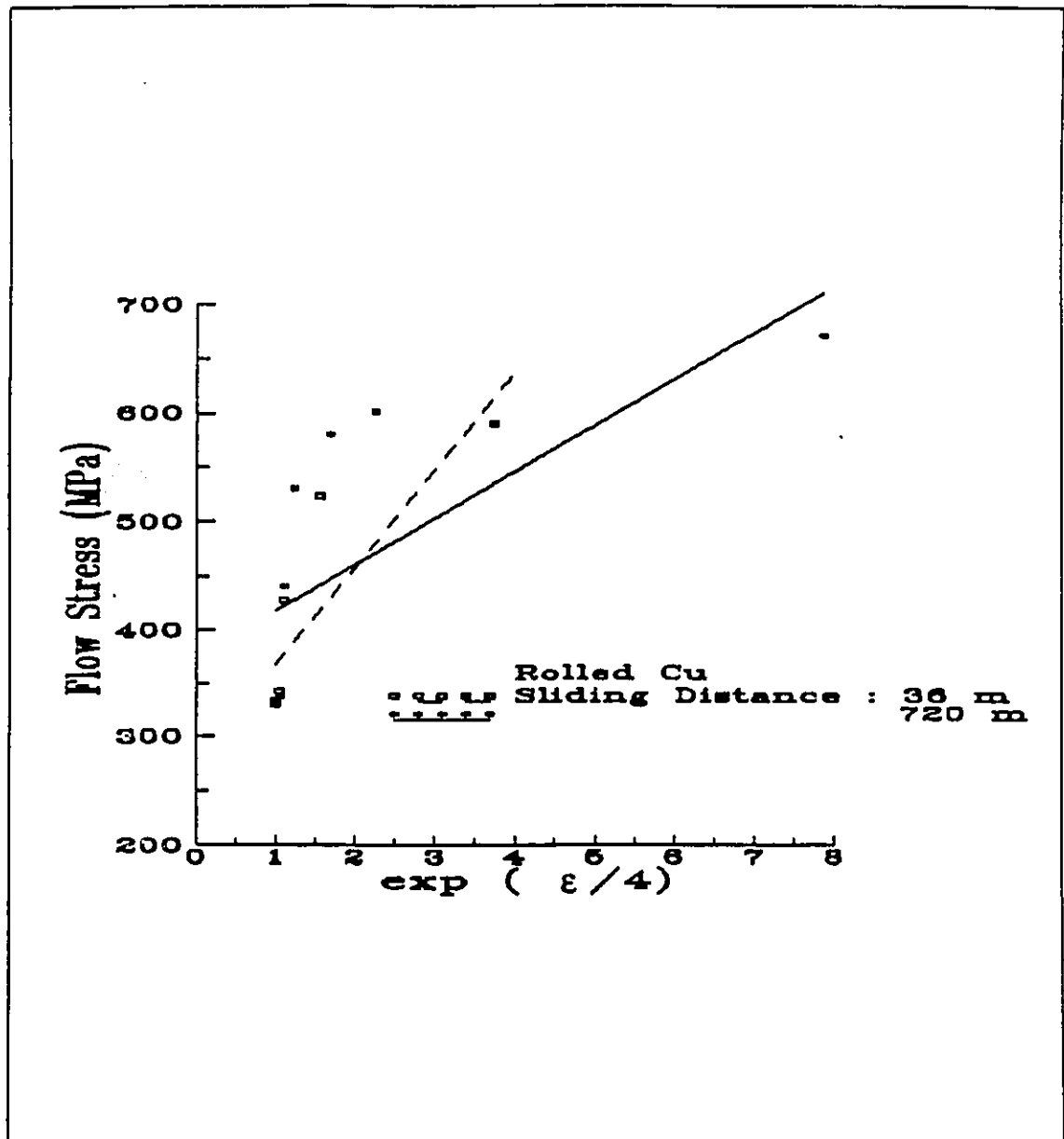
Fig. 5.8: Stress-strain behavior for rolled Cu represented by Embury equation,

$\sigma = f\ [\exp(\varepsilon/4)]$.
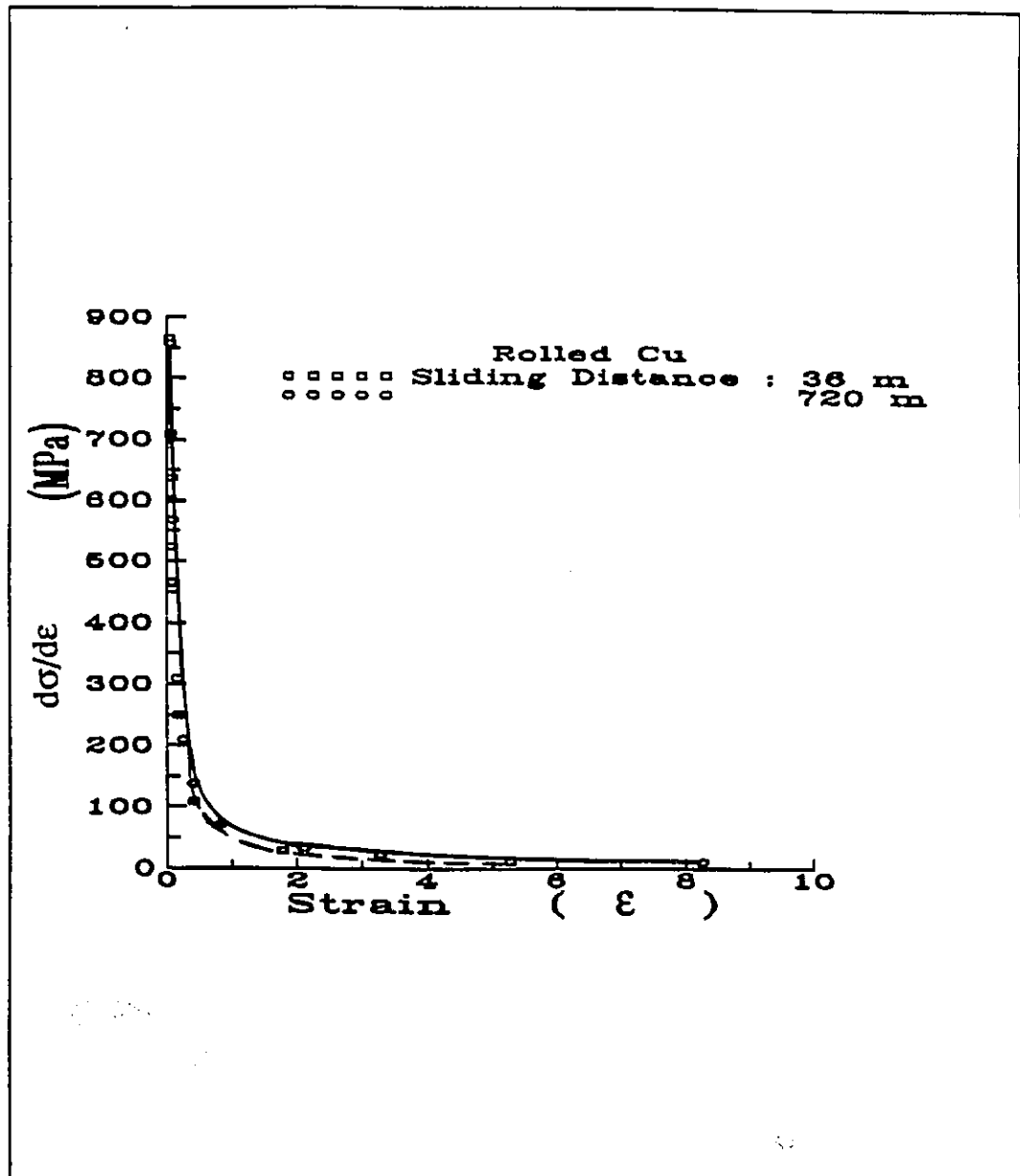
Fig. 5.9: Variation in work hardening rate with strain for rolled Cu

143

Fig. 5.10: Work hardening rate vs depth below the wear surface at two different sliding distances for rolled Cu.
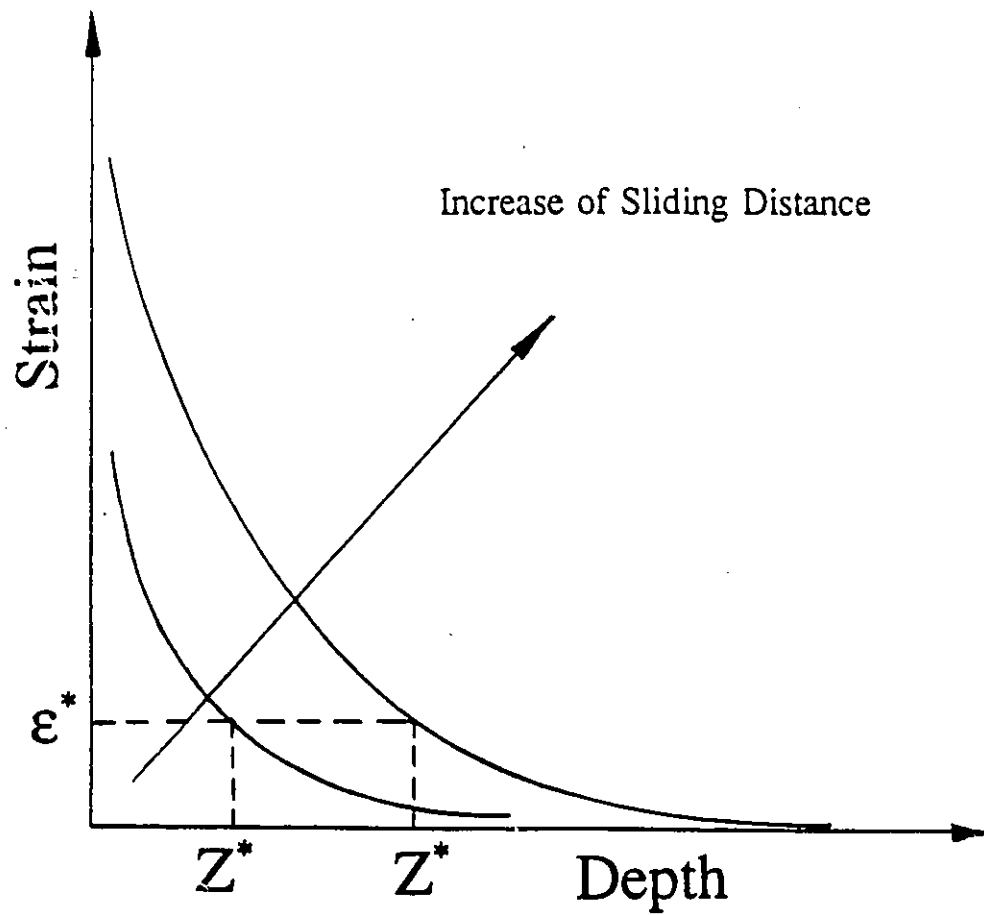
ε^* : Critical Strain Z^* : Critical Depth

Fig. 5.11: Schematic shows that the critical depth for maximum damage moves to deeper area below the worn surface with increase of sliding distance.
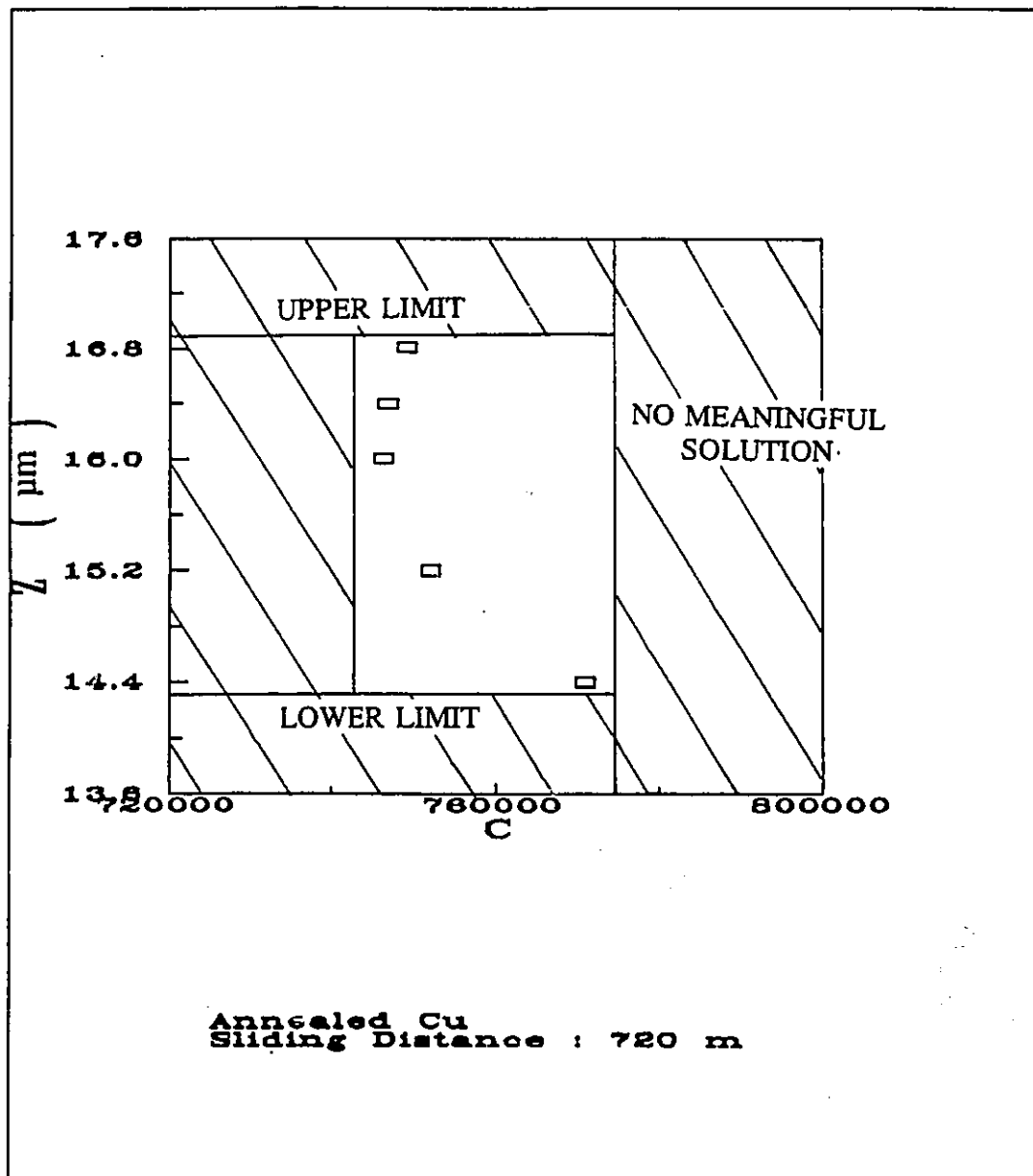
Contact Surface

(a)

Contact Surface
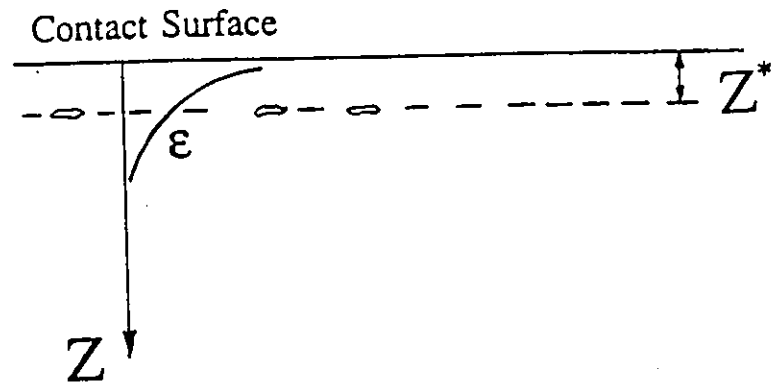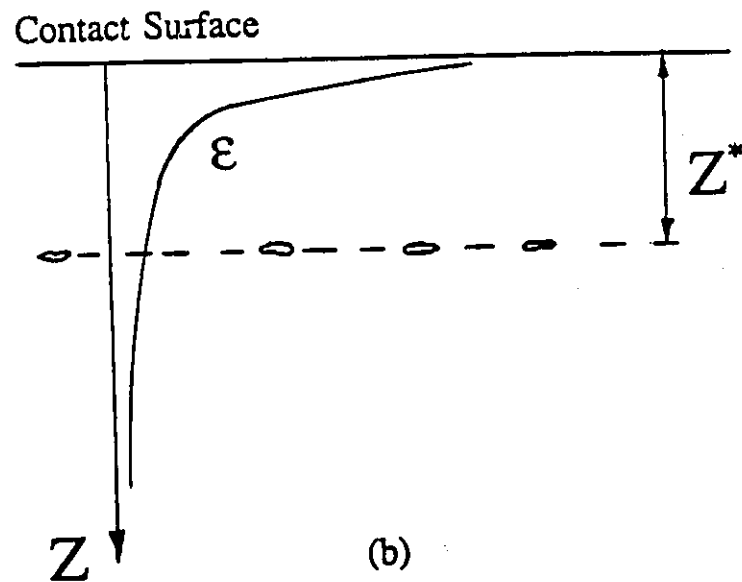
(b)

Fig. 5.12: Schematic shows that the higher wear rate at the beginning (a) is due to the critical depth very close to the worn surface, which results in faster damage propagation to the surface, compared with that when wear rate becomes a constant value (b).
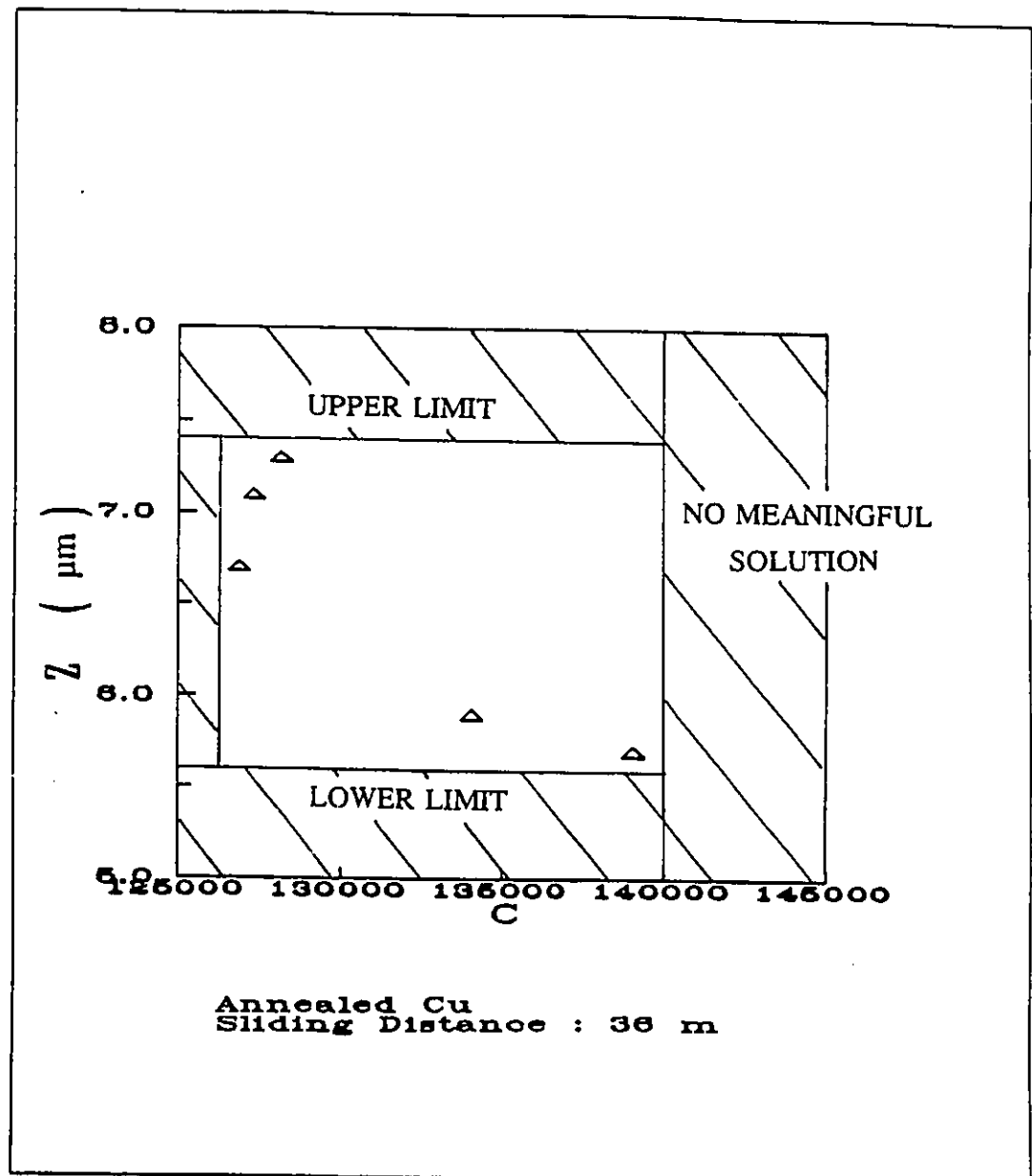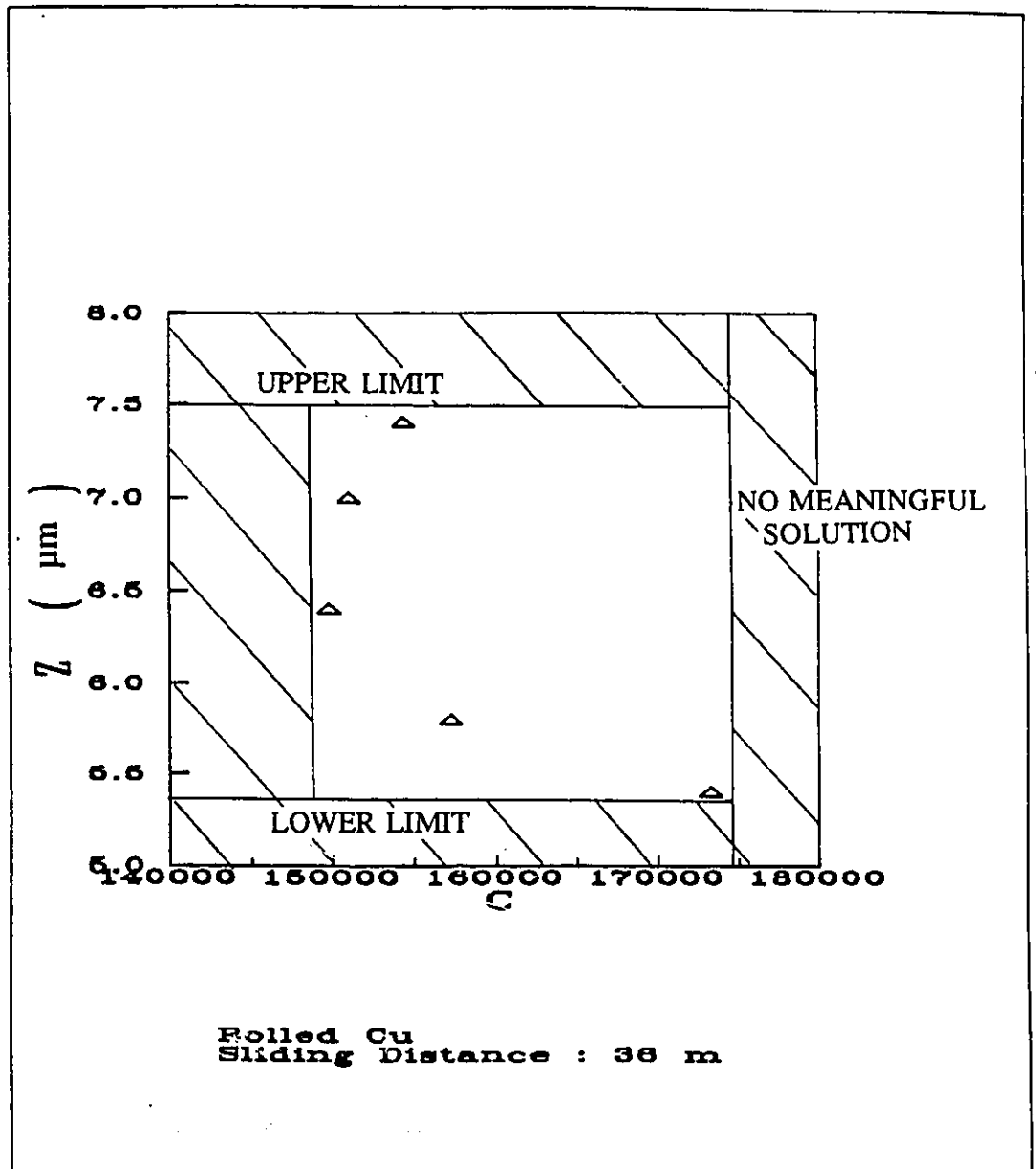
(a)

Fig. 5.13: The correlation between the critical depth, Z^* and A.

(a) and (b) for annealed Cu; (c) and (d) for rolled Cu at two different sliding
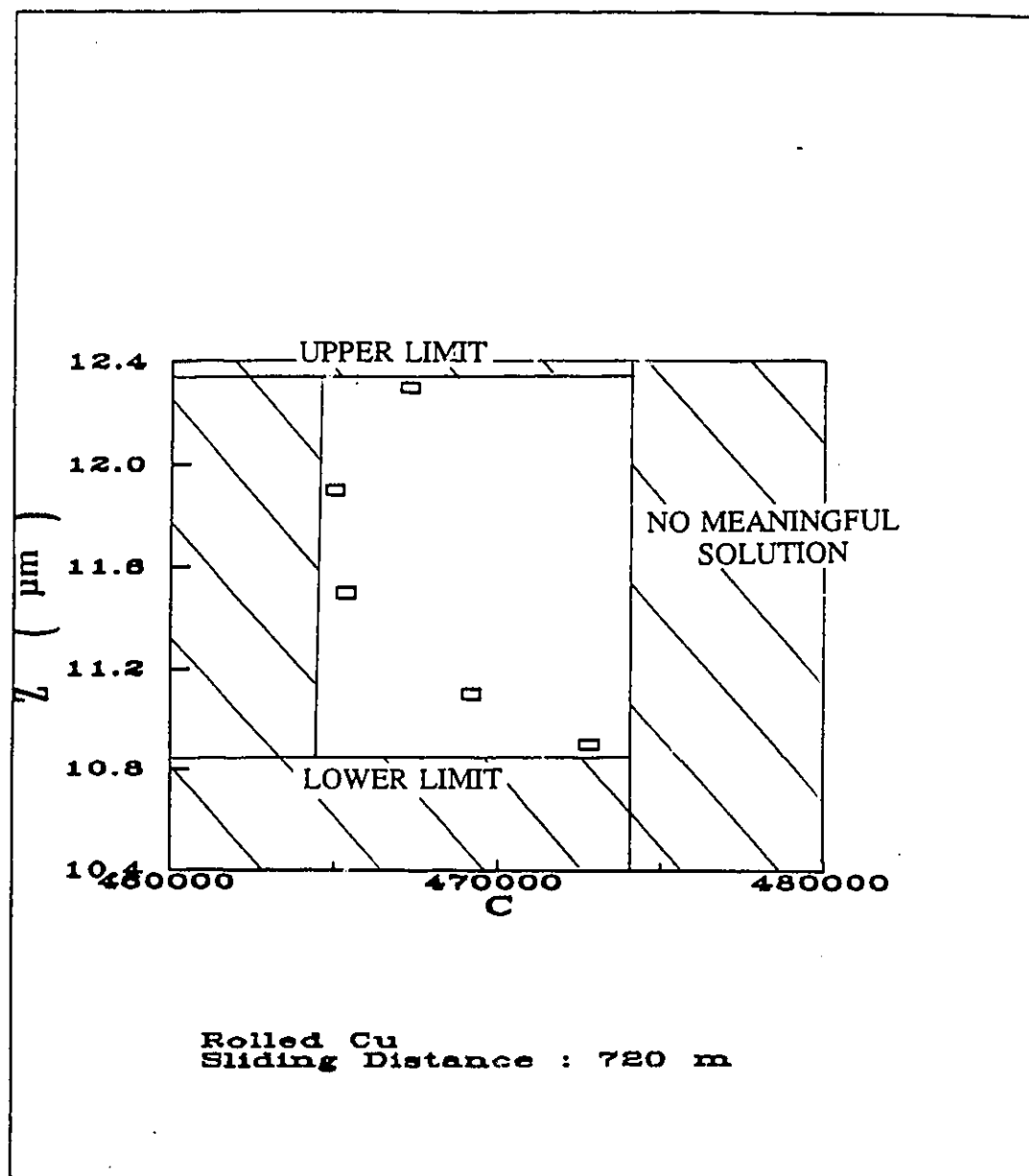
distances, 36 m and 720 m.
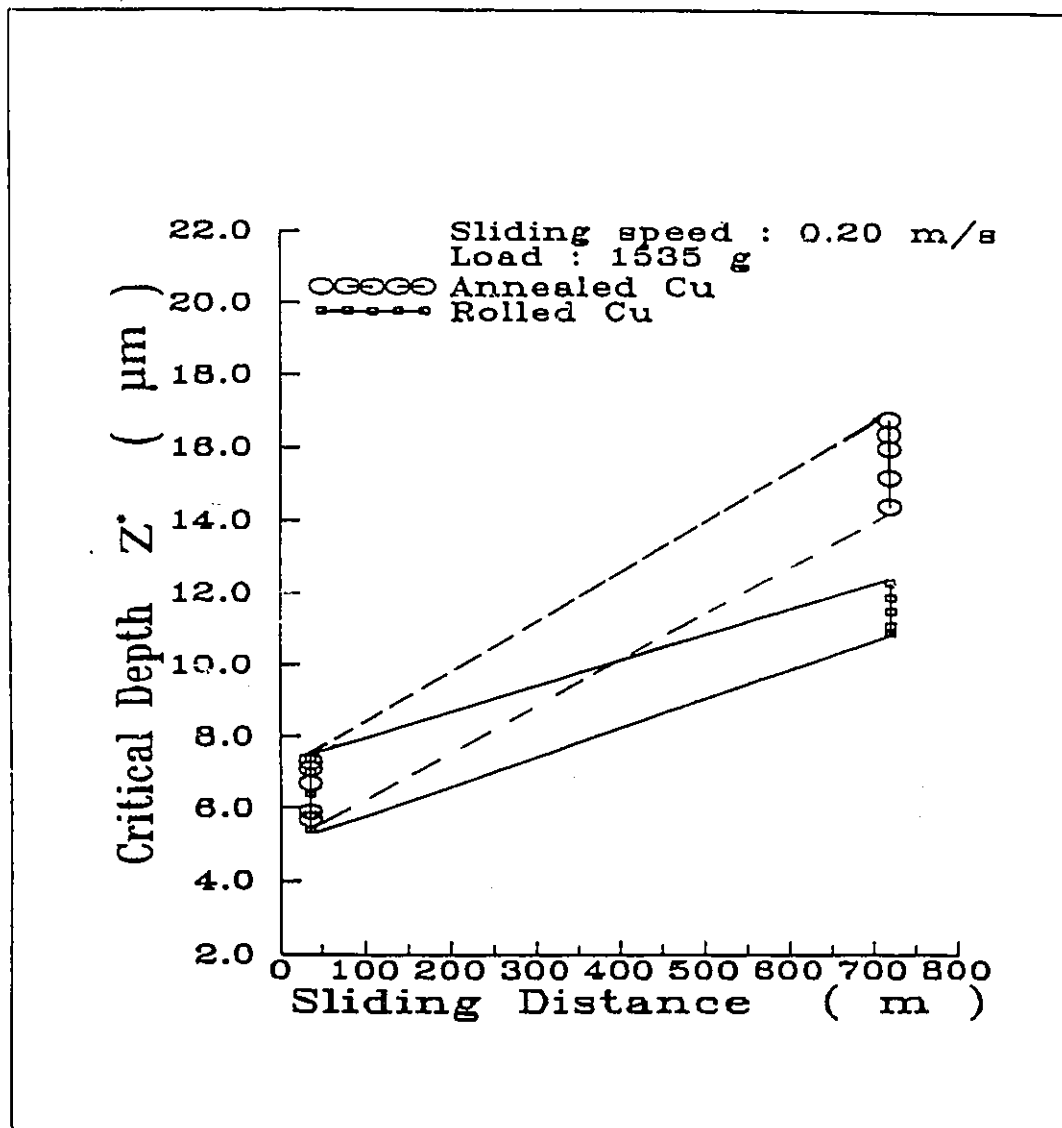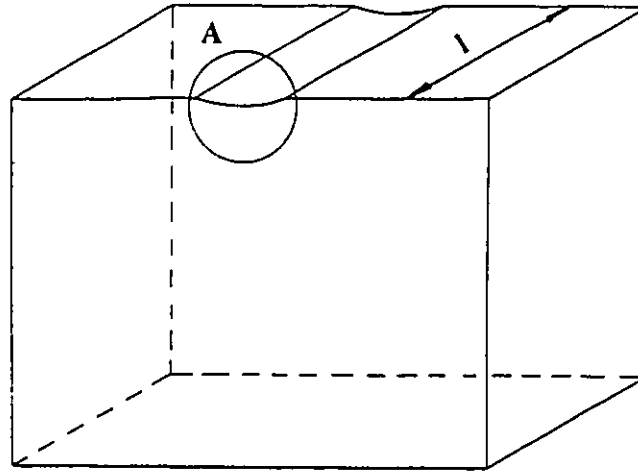
(b)

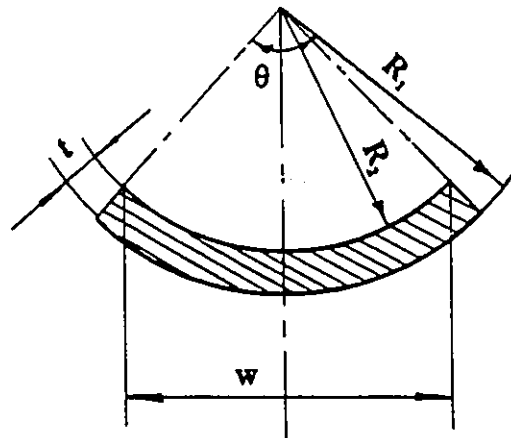Fig. 5.13 (continued) (b)

(c)

Fig.5.13 (continued) (c)

(d)

Fig. 5.13 (continued) (d)

Fig.5.14: The critical depth Z* increases with sliding distance for annealed and rolled Cu.

(a)

(b)

Fig. 5.15: Schematic representation shows the assumption of cross section of deformed

zone represented by the shadow area.

(a) specimen, (b) an enlarged A area in specimen to show the deformed layer.

VITA AUCTORIS

The author was born in Shanghai, P.R. China on March 20, 1964.

EDUCATION

Bachelor of Applied Science in Metallurgical Engineering, Shanghai University of Technology, Shanghai, P.R. China, 1985.

Join the M.A.Sc. Program in Engineering Materials at the University of Windsor, Windsor, Ontario, Canada, in September 1989.

EMPLOYMENT

Engineer, Shanghai People's Machinery Plant, Shanghai, P.R. China, 1985-1989.